THERMAL & STRUCTURAL PERFORMANCE OF A CAST IN PLACE REINFORCED CONCRETE BALCONY THERMAL BREAK

By:

Sarah Nicole Boila

A Thesis

Submitted to the faculty of Graduate Studies of the University of Manitoba
in partial fulfillment of the requirements for the degree of

Master of Science

Department of Civil Engineering
University of Manitoba
Winnipeg, Manitoba, Canada

To Eddie and Benjamin Boila

Acknowledgements

I would like to thank my advisors Dr. Dagmar Svecova and Dr. David Kuhn for their continued support throughout this research project. Their ideas, knowledge, and guidance have been invaluable and I am grateful for the opportunity to learn from their experience. I would like to thank Dr. Svecova for her financial support throughout my graduate degree.

I would also like to thank my co-advisor Dr. John Wells for his support and guidance. His contribution of industry relevant knowledge was considerably impactful on the direction of the research program.

A great thanks is extended to the members of the Red River College with who we worked as a partner to plan and execute the experimental program: Rob Spewak, Kevin Knight, Cory Carson, Cody Buskel, Brandon Campbell and Eric Groot.

I would like to thank Susan Grieef and Steven Wu from Crosier Kilgour & Partners ltd., and Bert Phillips from UNIES ltd. for sharing their technical knowledge and experience.

Many thanks are extended to SIMTReC and NSERC through their College-University Idea to Innovation (CU I2I) Collaborative grant for the funding required to realize this project, as well as Armadillo for their donation of the thermal break material and Building Products for their donation of the concrete.

A great thanks is extended to the staff of the W.R. McQuade Heavy Structures Laboratory, Dr. Chad Klowak, Grant Whiteside, and Brendan Pachal, who helped to develop and carry out the structural experimental testing program.

Abstract

Improving the thermal performance of building envelopes has become a focus in the construction industry, due to a growing awareness of our environmental responsibility and the subsequent introduction of stricter energy codes. Removing or reducing the impact of thermal bridges, which penetrate the building envelope and provide a conduit for heat transfer, is an effective method for improving the energy performance of a building as a whole. Reinforced concrete balconies are one example of thermal bridges, and are the largest source of heat loss through building envelopes after accounting for windows and doors.

Commercially available thermal breaks exist, in which the concrete in the balcony in line with the building's insulation is replaced with a thermally insulating material and the majority of the structural capacity across this joint is provided by reinforcement. Stainless steel reinforcement is typically used for its lower thermal conductivity in comparison to carbon steel. An experimental research program was carried out by the University of Manitoba to investigate the thermal and structural performance of a cast in place balcony thermal break system. This system differs from the existing manufactured units in that the thermal break material and reinforcement are assembled on site and cast in place. This program also focused on the performance of fiber reinforced polymer reinforcement in a thermal break to investigate the impact of its lower thermal conductivity.

This thesis includes the details of the experimental program used to test the thermal and structural performance of the thermal break when reinforced with either carbon steel, stainless steel, or glass fiber reinforced polymer (GFRP). Thermal experimental testing was used in conjunction with three-dimensional finite element modelling to quantify the heat transfer through each variation of the system. Structural experimental testing was carried out to assess the ultimate load carrying capacity and serviceability performance of the thermal breaks.

The experimental test results indicated that the GFRP reinforced thermal break provided the best thermal performance. Although the stainless steel reinforced thermal break gave a similar improvement in increasing interior surface temperatures, the impact of the GFRP reinforced thermal break on reducing heat transfer through the balcony outperformed the remaining two reinforcement types.

The structural experimental results found that all three of the thermal break variations satisfied the ultimate strength requirements as designed. The deflection of the cantilevered balcony was least impacted by the presence of the thermal break when GFRP reinforcement was used, indicating that it is also the preferred reinforcement type for structural requirements.

Further research is recommended to refine the reinforcement layout in order to determine the design which provides an optimal balance between the thermal and structural performance. It is also recommended to investigate and quantify the serviceability performance of the thermal break, and to address the separation at the thermal break-concrete interface.

Table of Contents

Acknowledgements i

Abstract ii

Table of Contents iv

List of Figures viii

List of Tables xiii

List of Symbols xv

1 Introduction 1

1.1 Overview 1

1.2 Background 1

1.3 Research Objectives 3

1.4 Scope of Work 3

2 Literature Review 5

2.1 Structural Cantilevered Balcony Design Using Reinforced Concrete 5

2.2 Thermal Bridging at Balcony Slabs 6

2.3 Materials 8

2.3.1 Thermal Conductivity of Structural Materials 8

2.3.2 Mechanical properties of Structural Materials 10

2.3.3 Thermal Break Materials 10

2.4 State of practice 12

2.4.1 Cost Effectiveness and Thermal Performance of Thermal Break Systems 12
2.4.2 Balcony Thermal Breaks containing GFRP Elements 13
2.4.3 Thermal Performance of Fiber Reinforced Polymer Thermal Breaks 16
2.4.4 Commercially Available Thermal Breaks 17
3 Experimental Program 20
3.1 System Design 20
3.1.1 Design Loads and Assumptions 20
3.1.2 Thermal Break Bending Moment Capacity 22
3.1.3 Thermal Break Shear Force Capacity 24
3.1.4 Reinforced Concrete Slab Capacity 25
3.1.5 Serviceability Requirements 27
3.1.6 Stresses on Thermal Break Material 28
3.1.7 Test Sample Design and Dimensioning 29
3.1.8 Test Sample Strength Calculations 30
3.2 Thermal Test Program 32
3.2.1 Thermal Testing Setup 32
3.2.2 Sample Instrumentation for Thermal Testing 35
3.3 Thermal Modelling 42
3.3.1 Numerical Calculation Method 42
3.3.2 Thermal Modelling Inputs 44

3.3.3 Numerical Mesh 46
3.4 Structural Testing Program 48
3.4.1 Sample Instrumentation for Structural Testing 53
3.5 Specimen Details and Casting 56
4 Experimental Results and Analysis 60
4.1 Experimental Thermal Results 60
4.1.1 Quality and Consistency of Thermal Experimental Results 61
4.1.2 Direction of Heat Flow 63
4.1.3 Experimental Temperature Profiles 65
4.2 Thermal Modelling 70
4.2.1 Thermal Conductivity of GFRP 70
4.2.2 Comparison between Model and Experimental Results 72
4.2.3 Heat Flow across Thermal Breaks 75
4.3 Structural Testing Results 78
4.3.1 Structural Experimental Data 79
4.3.2 Analysis of GFRP Reinforcement in Compression 91
4.3.3 Test Sample Yielding and Failure Loads 95
4.3.4 Structural Failure Modes and Yielding Behaviour 102
4.3.5 Thermal Break Rotation 114
4.3.6 Sample Deflection 117

4.3.7 Summary 121

5 Conclusions & Recommendations 122

5.1 Conclusions 122

5.2 Lessons Learned 124

5.3 Recommendations 125

References 127

Appendix 131

A.1 Full-Scale Balcony Ultimate Strength Design - GFRP Reinforcement 1

A.2 Full-Scale Balcony Ultimate Strength Design - Steel Reinforcement 4

A.3 Full-Scale Balcony Ultimate Strength Design - Stainless Steel Reinforcement 9

A.4 Load Takeoff for Structural Design 13

A.5 Rebar Tensile Testing 15

A.6 Concrete Compressive Strength and Density 18

A.7 Test Specimen Ultimate Strength Calculations – GFRP Reinforcement 20

A.8 Test Specimen Ultimate Strength Calculations – Steel Reinforcement 22

A.9 Test Specimen Ultimate Strength Calculations – Stainless Steel Reinforcement 24

A.10 Calculated Load Deflection Curves for Test Specimens 25

A.11 Thermistor Layout for Thermal Testing 26

List of Figures

Figure 1 Flexural stressed on reinforced concrete balcony cross-section at wall, shown with simplified reinforcement and the equivalent rectangular stress block for concrete compressive stresses 6

Figure 2 Discontinuity in building insulation introduced by balcony slab 7

Figure 3 Stress Strain curve for AFRP, CFRP, and GFRP 10

Figure 4 Thermal Break Location 21

Figure 5 Section 1 and Section 2 as labelled for the design of reinforcement in the cantilevered reinforced concrete balcony slab 26

Figure 6 Test sample dimensions, in mm 29

Figure 7 Thermal test chambers 32

Figure 8 Junction between top of test slabs and 4" rigid insulation wall in thermal test chambers, showing caulking and spray foam 33

Figure 9 Test samples in thermal chamber showing longitudinal side insulation 34

Figure 10 Plywood shelter with rear wall removed showing location of interior temperature sensor 35

Figure 11 Plywood shelter with rear wall installed showing location of exterior temperature sensor 35

Figure 12 Thermistor layout for mock-up sample, dimensions in mm 36

Figure 13 Mock-up thermal test on warm side 37

Figure 14 Longitudinal cross-sectional temperatures, in ˚C, on warm side of mock-up sample, taken from mid-line of the sample 37

Figure 15 Transverse cross-sectional temperatures, in ˚C, on warm side of mock-up sample, distanced 10 mm from the thermal break 38

Figure 16 Longitudinal cross-sectional temperatures, in ˚C, on cold side of mock-up sample, taken from mid-line of the sample 38

Figure 17 Transverse cross-sectional temperatures, in ˚C, on cold side of mock-up sample, distanced 10 mm from the thermal break 39
Figure 18 Thermistor layout and labelling for GFRP reinforced samples 40
Figure 19 Thermistor installation method inside of samples 41
Figure 20 Formwork prior to casting including thermal sensors 42
Figure 21 Boundary condition assignments on three-dimensional model 45
Figure 22 Numerical mesh for GFRP reinforced sample with thermal break a) as derived by the program and b) as selected for analysis 46
Figure 23 Average heat flow calculated for each model with each variation of numerical mesh 48
Figure 24 Structural Test Setup 49
Figure 25 Structural Test Setup - Support B 50
Figure 26 Structural Test Setup - Support A 51
Figure 27 Structural Test Setup - Load Point 52
Figure 28 Strain gauge configuration 54
Figure 29 Structural Test Setup - PI gauge configuration 55
Figure 30 PI gauge mount alignment 56
Figure 31 LVDT instrumentation 56
Figure 32 Formwork prior to casting 57
Figure 33 Force analysis for self-weight load induced by lifting hooks 58
Figure 34 Lifting hook attached to reinforcing bar in formwork 59
Figure 35 Photograph (left) and infrared image (right) of GFRP reinforced slabs tested in thermal chambers, taken from the warm chamber. 61

Figure 36 Temperature point selected for calculation of directional heat flows, located in cross-section C 63
Figure 37 Heat flow labelling for direction of heat flow analysis 64
Figure 38 Experimentally obtained temperature profiles for a GFRP reinforced test sample a) with thermal break and b) without thermal break, all temperatures in ˚C 66
Figure 39 Experimentally obtained temperature profiles for a carbon steel reinforced test sample a) with thermal break and b) without thermal break, all temperatures in ˚C 67
Figure 40 Experimentally obtained temperature profiles for a stainless steel reinforced test sample a) with thermal break and b) without thermal break, all temperatures in ˚C 69
Figure 41 Average temperature difference calculated between experimental and numerical results for a range of GFRP thermal conductivities 71
Figure 42 Maximum temperature difference calculated between experimental and numerical results for a range of GFRP thermal conductivities 71
Figure 43 Strain gauge placement 79
Figure 44 Strain gauge data for a GFRP reinforced sample with a thermal break 80
Figure 45 Strain gauge data for a GFRP reinforced sample without a thermal break 81
Figure 46 Neutral axis height measured from bottom surface of slab over duration of structural testing for sample 6, containing GFRP reinforcement without a thermal break 82
Figure 47 Strain gauge data for a carbon steel reinforced sample with a thermal break 83
Figure 48 Strain gauge data for a carbon steel reinforced sample without a thermal break 84
Figure 49 Strain gauge data for a stainless steel reinforced sample with a thermal break 85
Figure 50 Strain gauge data for a stainless steel reinforced sample without a thermal break 86
Figure 51 LVDT data obtained from samples containing GFRP reinforcement 87

Figure 52 LVDT data obtained from samples containing steel reinforcement 88
Figure 53 LVDT data obtained from samples containing stainless steel reinforcement 89
Figure 54 PI gauge data obtained from sample number 12 containing steel reinforcement with a thermal break 90
Figure 55 PI gauge data obtained from sample number 2 containing GFRP reinforcement with a thermal break 91
Figure 56 Stress and strain distribution for a GFRP reinforced concrete cross-section 92
Figure 57 Stress and strain distribution for a GFRP reinforced thermal break, neglecting the capacity of the thermal break 92
Figure 58 Modulus of elasticity of GFRP reinforcement in thermal break for sample 1, neglecting capacity of thermal break 94
Figure 59 Structural Test Setup 103
Figure 60 Concrete shear cracking in sample 1 immediately adjacent to support A between support A and the load point a) early on in testing but after ultimate design load and b) shortly before ultimate failure. 104
Figure 61 Concrete flexural cracking between support A and B on sample 1 105
Figure 62 Concrete shear cracking immediately prior to failure in Sample 2 105
Figure 63 Concrete shear cracking to the left of Support A prior to ultimate failure in sample 3 106
Figure 64 Concrete shear failure occurring between support A and B in sample 3 106
Figure 65 Concrete shear failure between support A and support B in sample 5 107
Figure 66 Concrete shear failure between support A and the load point in sample 6 107
Figure 67 Image of sample number 10 showing minimal opening of the thermal break prior to steel yielding 108

Figure 68 Image of sample number 10 after yielding of the steel reinforcement 109
Figure 69 Deflection of sample number 10 at the end of testing 110
Figure 70 Sample number 8 after yielding of the steel reinforcement 110
Figure 71 Figure 15 Deflection of sample number 8 at the end of testing 111
Figure 72 Sample 13 prior to yielding of the stainless steel reinforcement 112
Figure 73 Sample 13 after yielding of the stainless steel reinforcement 113
Figure 74 Sample 16 after yielding of the stainless steel reinforcement 113
Figure 75 Thermal break rotation for GFRP reinforced samples 115
Figure 76 Thermal break rotate on for carbon steel reinforced samples 115
Figure 77 Thermal break rotation for stainless steel reinforced samples 116
Figure 78 Deflection of GFRP reinforced samples 119

List of Tables

Table 1 Thermal conductivity of FRP composites 9

Table 2 Thermal conductivity of concrete from ISO 10456:2007 [8] 9

Table 3 Thermal break materials and their properties 11

Table 4 Summary of industry available balcony thermal break products 18

Table 5 Methods for determining deflection provided by manufacturers of thermal breaks 19

Table 6 Rebar reinforcement ratio design 24

Table 7 Calculated maximum deflections for full-scale designs 27

Table 8 Thermal break material stress calculations 28

Table 9 Ultimate strength capacity of test samples 31

Table 10 Theoretical deflection at failure load for test samples 31

Table 11 Material thermal conductivities used in computer modelling 46

Table 12 Number of computational cells in evaluated numerical mesh 47

Table 13 Test sample numbering scheme 60

Table 14 Average temperature difference and standard deviation of individual temperature points calculated between two samples of the same type 62

Table 15 Heat flow values calculated at discrete locations within test samples 64

Table 16 Comparison between experimental and modelled temperature profiles for GFRP reinforced samples 73

Table 17 Comparison between experimental and modelled temperature profiles for carbon steel reinforced samples 74

Table 18 Comparison between experimental and modelled temperature profiles for stainless steel reinforced samples 74

Table 19 Heat flows through samples containing GFRP reinforcement as calculated by Heat3 76
Table 20 Heat flows through samples containing carbon steel reinforcement as calculated by Heat3 76
Table 21 Heat flows through samples containing stainless steel reinforcement as calculated by Heat3D . 77
Table 22 Comparison between heat flows through a conventional balcony system and the thermal break variations 77
Table 23 Micro-strain in GFRP reinforcement at onset of plastic deformation within the thermal break .. 95
Table 24 Ultimate failure loads and moments for GFRP reinforced samples with a thermal break 97
Table 25 Ultimate failure loads and moments for GFRP reinforced samples without a thermal break 97
Table 26 Ratio between experimental failure load and calculated failure load for GFRP reinforced samples 98
Table 27 Yielding loads and moments for steel reinforced samples with a thermal break 98
Table 28 Ratio between experimental failure load and calculated failure load for steel reinforced samples 99
Table 29 Yielding loads and moments for stainless steel reinforced samples with a thermal break..... 100
Table 30 Ratio between experimental failure load and calculated failure load for stainless steel reinforced samples 100
Table 31 Percent reduction in ultimate load capacity for GFRP reinforced samples and yielding load for carbon and stainless steel reinforced samples 101
Table 32 Rotation calculated at equivalent service load 117
Table 33 Deflection at service load for GFRP reinforced samples 118
Table 34 Deflection at service load for steel reinforced samples 119
Table 35 Deflection at service load for stainless steel reinforced samples 120
Table 36 Summary of structural experimental results 121

List of Symbols

A_F	Cross-sectional area of FRP rebar
A_s	Cross-sectional area of carbon steel rebar
A_{ss}	Cross-sectional area of stainless steel rebar
C	Volumetric heat capacity of a material
C_F	Force in FRP compressive reinforcement
d	Distance between points of calculation, distance between compressive and tensile reinforcement
E	Modulus of elasticity
$E_{tension}$	Tensile modulus of elasticity
$E_{compression}$	Compressive modulus of elasticity
f_y	Yield strength
f_u	Ultimate strength
I	Rate of internal heat generation
k	Material thermal conductivity
K	Material thermal conductance as applied in Heat3
H	Net heat flow to a cell as applied in Heat3
l	Length, moment arm during structural testing between thermal break and applied load
M_y	Moment at which reinforcement yielding occurs
M_{ult}	Moment at which ultimate failure occurs
P_{calc}	Calculated experimental failure load
P_y	Experimental yielding load

P_{ult}	Ultimate experimental failure load
Q	Heat flow
Q_x^+	Longitudinal heat flow in positive direction
Q_x^-	Longitudinal heat flow in negative direction
Q_y^+	Vertical heat flow in positive direction
Q_y^-	Vertical heat flow in negative direction
Q_z	Transverse heat flow
R	Boundary surface resistance as applied in Heat3
T	Temperature
T_r	Tensile resistance of a section or member
T_f	Factored tensile force
T_F	Force in FRP tensile reinforcement
V_f	Factored shear force
V_r	Shear resistance of a section or member
Φ_s	Material strength reduction factor for carbon steel
Φ_{ss}	Material strength reduction factor for stainless steel
Φ_f	Material strength reduction factor for FRP materials
λ	Material thermal conductivity
ρ	Material density
$\sigma_{tension}$	Tensile stress
$\sigma_{compression}$	Compressive stress

1 Introduction

1.1 Overview

The following thesis is comprised of six chapters. The first chapter introduces the relevance of this research project relating to the growing environmental constraints of the construction industry, and provides an overview of the research objectives and scope of work. Chapter two reviews literature pertaining to the project topic. Existing practices of constructing balconies are presented, followed by a review of the impacts of thermal bridging in buildings. A summary of relevant construction materials and their properties is presented, and the current state of practice for thermal bridging solutions for balconies is discussed. Chapter 3 presents the experimental testing program used for this project. Included is a detailed explanation of the structural designs, with an overview of the test specimen details and the procedures for specimen construction. The instrumentation, test setup, and testing procedures used for both thermal and structural testing are summarized. The thermal modelling approach is presented. Chapter four presents the experimental results and analysis. The data obtained from thermal testing is presented and verified through numerical modelling in order to draw conclusions regarding the system's thermal performance. Structural testing results are presented, and the ultimate strength and serviceability performance is discussed. Lastly, chapter six presents the conclusions obtained through this experimental program and provides recommendations for future work.

1.2 Background

In our society there exists a growing public awareness regarding the need to reduce our consumption of natural resources and greenhouse gas emissions, both as individuals and as a community. While individuals may take steps in their daily lives to implement small changes that will have positive impacts on their environmental footprint, within industries we sometimes require profound shifts in procedures to overhaul

current practices that have been rendered unfit based on newly introduced environmental constraints. These significant changes must strike a balance between satisfying the new environmental constraints while remaining as, if not more, economical than the tried and tested approaches of the past. Not only this, but they must be presented in a way that the public and industry can be comfortable with and can trust.

One industry that has been addressing the growing constraint of complying with environmental requirements is the building construction industry. This industry generally relies on long standing practices for designing, building, and constructing projects. For the building construction industry to reduce its environmental footprint, it can take several approaches. One approach may be to streamline the construction process, shortening the construction time and reducing the greenhouse gas emissions produced by trucks and equipment during the construction of a project. Alternatively, the industry could focus their efforts on using sustainably sourced materials within their projects. One common and effective approach to developing sustainable buildings, and the one that is addressed in design codes and building rating systems such as Leadership in Energy and Environmental Design (LEED) [1] and the National Energy Code of Canada for Buildings [2] is to improve the insulation of the building envelope and thus lower heating and cooling loads over the life cycle of the building.

Improving the insulation of the building envelope is mainly achieved by selecting thermally insulating materials with higher R-values as construction materials. While wall panels can be fairly easily insulated in this way and the thermal resistance of glass windows is steadily improving, thermal bridging occurring at locations such as the interface of concrete balconies and wall systems continue to compromise the integrity of the building envelope for the entire structure. Thermal bridges provide a thermally conductive path across a building's insulation, connecting the interior and exterior environments and essentially creating a weak spot in the insulation. In a typical balcony design, a reinforced concrete slab is cantilevered through the insulation and beyond the exterior wall. The concrete and reinforcing steel act as thermal conductors,

and with the large surface area of the balcony they create a cooling fin for the building during cold winter months. This results in a temperature reduction in the concrete slab and interior surfaces and creates conditions conducive to condensation. Uncontrolled condensation may deteriorate the structural and architectural components of a building, and negatively affect the indoor air quality by inducing mold growth. The question that then remains, and which this thesis aims to answer, is whether there could be a new method of constructing cantilevered balcony systems that removes, or significantly reduces, the thermal bridging effect without sacrificing structural capacity of the system, by making use of newly available structural materials.

1.3 Research Objectives

The objective of this research program is to design a cast in place balcony thermal break system and to investigate its performance using three reinforcement types: carbon steel, stainless steel, and fiber-reinforced polymer.

First and foremost, the resulting design must provide an effective reduction in thermal conductivity across the balcony-wall joint system while maintaining structural capacity regarding both strength and serviceability requirements. The project aims to experimentally verify both the thermal and structural behaviour of the newly designed systems, and to determine the relative heat loss reduction provided by the new system.

A long term goal of the project is to have the designs adopted into Canadian Design Codes, ensuring wide spread understanding and application of the system.

1.4 Scope of Work

The scope of work for this project may be divided into the following three phases: structural system design, thermal performance testing and modelling, and structural capacity testing.

Structural system design involved utilising available design codes to design the reinforcement ratio required to maintain structural capacity across the newly designed thermal breaks. Design calculations include verifying the shear force and bending moment capacity at critical locations, as well as verifying the serviceability performance of the designs. In order to perform the aforementioned thermal and structural testing, sample sizes of the designed thermal breaks were constructed.

Thermal performance testing and modelling involved designing and implementing a thermal testing program. This included the design and installation of a thermal instrumentation layout, and the design of a thermal testing facility. Thermal experimental testing was performed under steady state conditions over a temperature difference of -31˚C to +21˚C with no thermal cycling. Thermal modelling involved the development and refinement of a numerical model representing the thermal properties of the systems.

Structural capacity testing involved designing and implementing a structural testing program. Included was the design and installation of instrumentation for measuring the strain within reinforcement, deflection of the samples, and rotation of the thermal break. Structural testing was performed under monotonically increasing load. The design of the structural testing setup was also performed.

Lastly, the scope of work of this project involved the application of fundamental engineering principles and numerical modelling to analyse the data obtained from the aforementioned testing programs. Conclusions are drawn regarding the results and recommendations are provided for future work.

The scope of this experimental program regarding materials included one type of thermal break, Armatherm 500™, with one thickness of 25 mm. Three types of reinforcement were included, being carbon steel, stainless steel, and glass fiber reinforced polymer. One concrete strength was included. The thermal testing and analysis was performed under steady state conditions, and the structural testing was performed under monotonically increasing load.

2 Literature Review

The following literature review introduces the reader to the current state of practice within the industry regarding the construction of reinforced concrete balcony slabs. Thermal bridging is defined and its associated negative impacts are presented. Relevant structural materials, including concrete, carbon steel, stainless steel, and glass fiber reinforced polymer (GFRP), are briefly reviewed. A summary of relevant structural insulation materials is also presented. Lastly, the current state of practice for implementing thermal breaks in balconies is presented, providing an overview of relevant research topics as well as a summary of several manufactured thermal breaks.

2.1 Structural Cantilevered Balcony Design Using Reinforced Concrete

Reinforced concrete is a commonly used material in civil engineering for structures, including bridges and buildings. Reinforced concrete structures are designed using the concept of limit state design, in which the section must perform adequately for ultimate strength limit state and serviceability limit state requirements [3]. These requirements include strength at ultimate load, deflection at service load, and crack widths at service load.

In cantilevered balcony design, loads applied to the balcony surface are transferred to the supporting structure through the connecting joint at the wall, resulting in bending moment and shear forces in the slab at this location, as shown in Figure 1. These forces will induce tension in the top portion of the balcony slab and compression in the bottom portion, which are mainly resisted by the reinforcement and concrete, respectively. Reinforced concrete balconies are typically cast monolithically with the wall system of the building, creating a seamless, uniform connection to efficiently transfer loads across the joint.

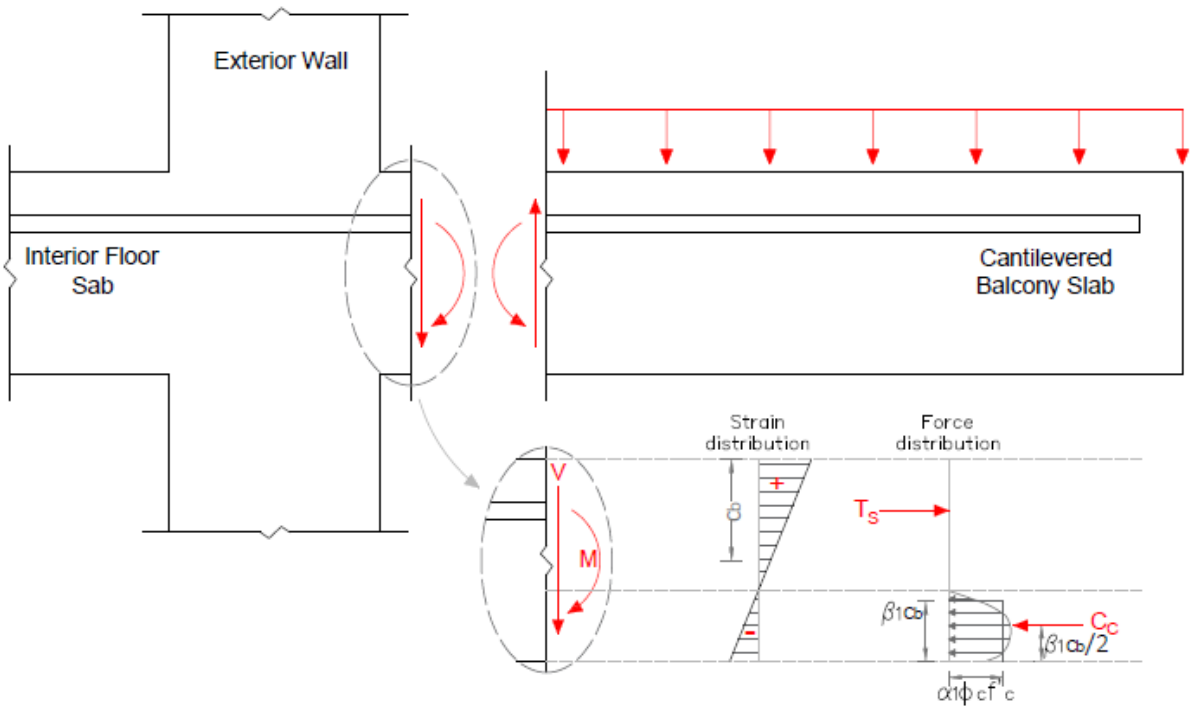

Figure 1 Flexural stressed on reinforced concrete balcony cross-section at wall, shown with simplified reinforcement and the equivalent rectangular stress block for concrete compressive stresses

2.2 Thermal Bridging at Balcony Slabs

In Canada in 2010, space heating of residential buildings accounted for approximately 63% of the residential sector energy use and 10% of the total national energy use [4]. The building industry has been gradually improving insulating methods to reduce this number, implementing more efficient designs such as continuous exterior insulation [5]. Because of the monolithic construction and protrusion of concrete from the interior walls to the exterior of the building with a cantilevered balcony slab, it becomes a challenge to thermally insulate this element of the building envelope. The cantilevered balcony slab introduces a gap in conventional insulation, whether it is applied to the interior or exterior of a building, thus creating a weak spot in the building's enclosure, as shown in Figure 2

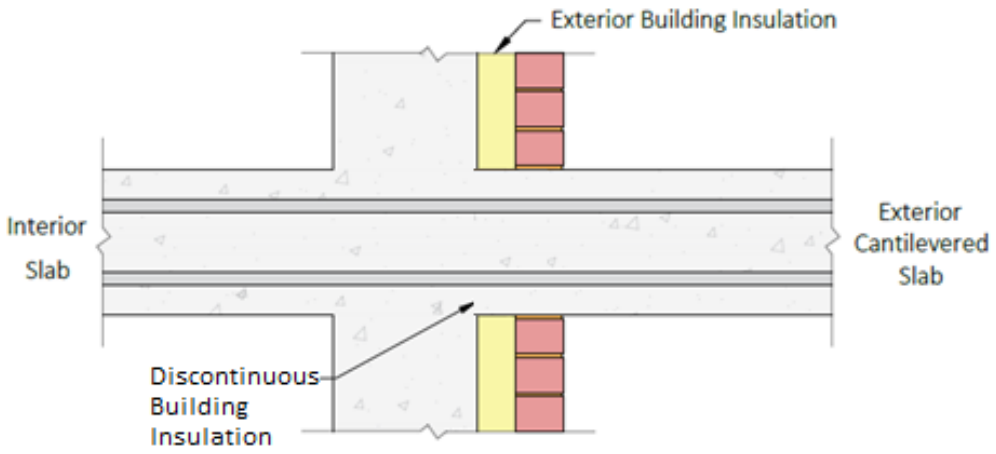

Figure 2 Discontinuity in building insulation introduced by balcony slab

When heat flow bypasses the insulation of a building enclosure, a thermal bridge is formed [5]. Examples of thermal bridges other than continuous balcony slabs include exposed slab edges, windows and doors, and studs or joists within the insulation area. After accounting for windows and doors, balconies are responsible for the second greatest source of thermal bridging and heat loss in multi-story residential buildings. The heat flow through these thermal bridges can cause an otherwise well insulated building to not meet energy code requirements, designer intent, or occupant expectations [5]. Thermal bridges bring upon these detrimental effects through two mechanisms: increasing the heating or cooling demand of a building, and reducing the interior surface temperature at the location of the thermal bridge.

The first mechanism involves heat energy escaping or entering the building's enclosure by travelling along the thermal bridge. Up to 30% of a building's heating energy may be lost through thermal bridges in residential buildings constructed with high-performance windows and highly insulated walls and roofs [6]. This increase in energy loss must be balanced by an increase in mechanical heating or cooling to maintain the desired environment within a building. This leads to higher operational costs for the owner and / or occupants of the building, as well as negative environmental impacts from an increase in greenhouse gas emissions.

The second mechanism involves a decrease in surface temperature at the location of the thermal bridge, occurring during wintertime. When the interior surface temperature falls below the dew point condensation will occur, eventually leading to mould growth. Condensation and mould growth may deteriorate the structural components of the building, and will reduce the interior air quality for its occupants. Exposure to mould and its airborne spores has been shown to increase the risk of respiratory symptoms, respiratory infections, and to aggravate symptoms produced by asthma [7].

2.3 Materials

The following section will present the thermal and structural properties of both structural and insulating materials relevant to the development of a balcony thermal break. Structural materials include carbon steel, stainless steel, and fiber-reinforced polymer reinforcement, as well as concrete. A variety of proprietary thermal break materials and their properties are also discussed.

2.3.1 Thermal Conductivity of Structural Materials

Typical reinforced concrete balconies are constructed using carbon steel, having a thermal conductivity, λ, of 50 W/mK [8]. In order to reduce the effective heat flow across the balcony, this reinforcement is typically replaced with stainless steel in balcony thermal breaks, having a thermal conductivity of 25 W/mK.

Further benefits could be provided by replacing the reinforcement with a fiber reinforced polymer (FRP) product, which provide a significantly lower thermal conductivity. Fiber reinforced polymers are a composite material, consisting of fibers and a matrix that are mechanically bonded together to provide a final material with superior properties than the components alone [9]. The thermal conductivity of an FRP composite is dependent on the fiber type, fiber orientation, fiber volume fraction, and polymer type of the composite [10], therefore it will vary from product to product. As such, the data found in literature

regarding the thermal conductivity of FRP composites used in civil applications, provided in Table 1 is variable and often provided as a range of values.

Table 1 Thermal conductivity of FRP composites

Material	Longitudinal λ (W/mK)	Isotropic λ (W/mK)
High Strength Carbon Fiber, Epoxy Matrix, 60% Volume Fraction [11]	10.38 – 17.30	1.73 – 5.19
Carbon Fiber, Epoxy Matrix [12]	3.8 – 8.0	0.4 – 0.8
S-glass Fiber, Epoxy Matrix, 60% Volume Fraction [11]	3.46	0.35
Aramid Kevlar-49 Fiber, Epoxy Matrix, 60% Volume Fraction [11]	1.73	0.17

Significantly more data is available through literature for the thermal conductivity of carbon fiber reinforced polymers (CFRP) in comparison to glass fiber reinforced polymers (GFRP) and aramid fiber reinforced polymers (AFRP), which is likely due to the fact that it has been used more widely than the other two materials. The thermal conductivity of CFRP is on average higher than the thermal conductivity of GFRP or AFRP. The thermal conductivity of GFRP is less than one tenth the thermal conductivity of carbon steel.

The thermal conductivity of concrete is provided in Table 2 and ranges from 1.15 W/mK to 2.00 W/mK as a function of the concrete's density. It should be noted that the thermal conductivity of concrete is approximately 25 and 12.5 times smaller than that of carbon steel and stainless steel, respectively, and is similar to the thermal conductivity of GFRP.

Table 2 Thermal conductivity of concrete from ISO 10456:2007 [8]

Concrete Type	Density ρ [kg/m^3]	Thermal Conductivity λ [W/mK]
Medium density	1800	1.15
	2000	1.35
	2200	1.65
High density	2400	2.00

2.3.2 Mechanical properties of Structural Materials

Regular mild steel and stainless steel reinforcement are designed for their yield strength, after which the material loses its ability to resist deformation and experiences large plastic deformations under increasing stress [13]. Unlike steel, FRP materials are anisotropic with a high tensile strength and no yielding in the direction of the fibers [14], as shown in Figure 3. FRP rebar, specifically GFRP, has a significantly lower modulus of elasticity than steel. Therefore, serviceability limits often govern in design for GFRP reinforced concrete.

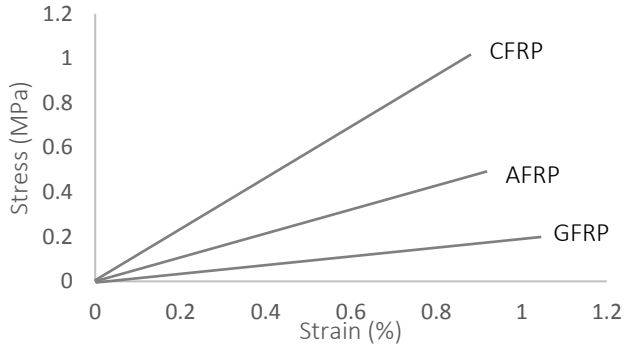

Figure 3 Stress Strain curve for AFRP, CFRP, and GFRP

Unlike carbon and stainless steel, the contribution to compressive capacity of FRP in reinforced concrete is neglected due to its lower compressive strength and complex behaviour in compression caused by fiber micro buckling. Standard test methods are not yet available for testing compressive strength of FRP materials [15]. Values found in literature show a strength reduction of up to 45% for GFRP rebar under compression, and a compressive modulus equal to approximately 80% of the tensile modulus [10].

2.3.3 Thermal Break Materials

Thermal insulation is a material or combination of materials that reduces the rate of heat flow through the assembly in which it is installed [16]. Traditional building insulation is installed within the building envelope and is non-load bearing, serving only to provide insulating capacity to the building. In order to

accommodate new designs and building envelope solutions, such as load bearing thermal breaks, certain materials have been designed or adapted to provide structural capacity as well as thermal resistance. These materials are variations of rigid insulation, with widely varying compositions, and range from simple materials to well-developed proprietary products. The two main properties of interest when selecting a thermal break material are its thermal conductivity (or thermal resistance) and compressive strength. A non-extensive list of these materials is provided in Table 3, listed from lowest thermal conductivity to highest.

Table 3 Thermal break materials and their properties

Product	Composition	Thermal Conductivity [W/mK]	Compressive Strength [MPa]	Fire Protection
Dow Styrofoam Highload 100 [17]	Extruded Polystyrene	0.028	0.69	Combustible
Armatherm 500 [18]	Thermoset Polyurethane	0.0448 - 0.0742	3.86 - 14.82	Flame Resistant
Mightylite [19]	Xonotlite crystal structure composed of lime, silica, and reinforcing fibers	0.085 - 0.136	3.1 - 29	Fire Rated
Redco CPVC [20]	Polyvinyl chloride	0.137	69.6	V-0, 5VB, 5VA rated according to UL 94 [21]
Armatherm Grade FRR [22]	Reinforced Thermoset Resin	0.2	310	Fire Resistant

A desirable thermal break material would have a low thermal conductivity and a high compressive strength. As shown in Table 3, it is often a trade-off between these two properties; a material with a low thermal conductivity will compromise by having a low compressive strength, such as the Dow Styrofoam Highload 100. Conversely, a material with excellent structural capacity will have an undesirably higher thermal

conductivity, such as the Armatherm FRR. Therefore, different materials may be better suited for different applications depending on the requirements of the individual design.

The fire resistance of such materials is also relevant when installed in building enclosures. Several materials offer a range of fire resistance, but for those without adequate fire resistance additional protection would be required within the assembly to ensure the design meets fire code requirements. This is usually achieved by sealing the thermal break along its top and bottom edge with a material that provides the required fire rating.

2.4 State of practice

The following section will present several experimental studies pertaining to balcony thermal break systems, particularly in which the use of GFRP as reinforcement is investigated. A summary of available manufactured thermal break systems and their details will then follow.

2.4.1 Cost Effectiveness and Thermal Performance of Thermal Break Systems

In a study performed by RDH Building Engineering Ltd. in 2013, the cost-effectiveness and thermal performance of several concrete balcony thermal bridging solutions was evaluated [23]. The evaluated systems included [24]:

- Structural slab cut-outs with beam reinforcement, in which the balcony slab connection is constructed as 60% void space with the remaining 40% acting as beam reinforced to accommodate the entire slab load at its ends. The system was modelled with and without exterior insulation within the cut-out space.
- Concentrated rebar, in which the balcony slab reinforcement is placed within 40% of the slab to create a series of small beams, and the remaining 60% of the area is replaced with insulation or left as a void.

- Full and partial balcony slab thermal wraps, in which 2” extruded polystyrene is wrapped in varying extents on the top and bottom surface of the exposed balcony.
- Manufactured concrete slab thermal breaks, provided by manufacturers and offering a range of thermal conductivities. Data for the Schoeck Isokorb [25] was used for modeling.

Three dimensional thermal simulations were performed using the software Heat3 to determine the effective R-values of the thermal break solutions when used with different wall assemblies and floor finishes. Cost evaluations included the construction cost, material cost and installation cost per length of exposed balcony, using data for construction and material costs in Vancouver, BC in 2012. The results determined that the thermal performance and cost effectiveness of the structural slab cut-outs, concentrated reinforcement, and balcony insulation wraps were relatively poor in comparison to manufactured thermal breaks. Therefore, manufactured thermal breaks were suggested as the preferred method for reducing thermal bridging at reinforced concrete balcony slabs. It has also been apparent through existing projects that manufactured thermal breaks have been the method of choice to most commonly remedy thermal bridging at balcony slabs.

2.4.2 Balcony Thermal Breaks containing GFRP Elements

In a study performed by Keller et. al. [26], a new thermal break in which the lower stainless steel compressive bars were replaced by GFRP compression elements was evaluated. The system was designed to transfer a portion of the shear force through the GFRP elements. The GFRP compressive elements were made of E-glass fibers and resin and measured 100 mm in width by 60 mm in depth with a length of 88 mm. They had a three-cell construction, resembling a hollow-core concrete slab. The thermal breaks were constructed using the GFRP compressive elements, stainless steel tensile reinforcement, and stainless steel shear reinforcement passing through a 100 mm thick Styrofoam block.

Full-scale experiments were performed on cantilevered concrete beams containing the thermal breaks. The elements were tested both under predominantly bending moment loading, and under predominantly shear force loading. On the non-cantilevered ends of the beams a support was in place to prevent uplift. In order to simulate different building wall configurations, the non-cantilevered end was supported either immediately behind the thermal break, or 100 mm behind it by a 100 mm wide steel plate. The cantilevered portion of the sample was loaded either 320 mm from the thermal break for shear force loading or 660 mm from the thermal break for bending moment loading.

Displacement of the slab was monitored at the top surface at both concrete-thermal break interfaces, as well as at the cantilevered edge. Two strain gauges were installed on each internal reinforcing bar, and ten strain gauges were installed on each GFRP element. The samples were loaded in four cycles at a displacement rate of 10 mm/min. The four cycles were loaded until 30%, 60%, and 90% of the ultimate load, and lastly until failure.

The experimental results showed that on average 33% higher failure loads occurred when the beams were loaded in shear mode in comparison to moment mode. As well, the beams with a larger depth of 240 mm had on average 30% higher failure loads than those with a depth of 200 mm.

Failure for all test samples occurred through yielding of either the tensile or shear stainless steel reinforcement. Under primarily bending moment loading only the tensile reinforcement yielded. After yielding, concrete crushing occurred at the lower edges of the concrete-GFRP element interface and opening occurred in the upper part of this interface. With the support directly behind the thermal break the concrete crushing occurred on the loaded side, and with the support 100 mm behind the thermal break the concrete crushing occurred on the supported side. The GFRP elements only exhibited cracking after ultimate failure of the slab.

Under primarily shear force loading either both tensile and shear reinforcement yielded, or only shear force reinforcement yielded. Opening occurred at the concrete-GFRP element interface at the upper part of the GFRP element on the loaded side, as well as on the lower part on the supported side. This showed a tilting of the GFRP element under predominantly shear force loading. With the support immediately behind the thermal break, the concrete did not exhibit any signs of failure. With the support moved 100 mm behind the thermal break, concrete crushing occurred on the supported side after yielding of the steel reinforcement. Again, failure cracking in the GFRP elements only occurred after yielding of steel and crushing of concrete.

Shear transfer through the GFRP element was a point of interest in this study, in hopes that in a future model the shear reinforcing bars of the thermal break may also be replaced by the GFRP element. The results showed that under primarily bending moment loading nearly none of the shear force was transferred through the GFRP element. However under predominantly shear force loading, 43% to 63% of the total shear force was transferred through the GFRP element.

In terms of deflection, the total deformation of the beams consisted of a rotation about the support point and a vertical offset within the joint. Under primarily bending moment loading the rotation was dominant, and under primarily shear force loading the vertical offset was dominant. Results showed that at the serviceability limit the vertical offset measured 0.5 mm to 2 mm, providing an acceptable range. The rotation about the thermal break however showed the potential to introduce larger deflections with larger cantilevered span lengths, which may be calculated considering strains in the tensile steel reinforcement and GFRP element combined with the deformation of the concrete slab itself.

The durability of the system was also investigated by exposing the GFRP elements to alkaline solutions at varying temperatures over 18 months, and found that the elements exhibited good long-term performance.

In terms of thermal conductivity, replacing the lower stainless steel bars with GFRP elements improved the linear thermal conductivity of the system to 0.1-0.2 W/m·K. The overall performance of the system was improved by 26% when compared to a system constructed using only stainless steel reinforcement. Overall, the newly developed thermal break system using GFRP elements provided satisfactory structural performance while significantly improving the thermal performance of the system. Therefore, thermal breaks implementing GFRP as reinforcement in place of stainless steel pose a viable option for improving the performance of thermal breaks and therefore the performance of building envelopes as a whole.

2.4.3 Thermal Performance of Fiber Reinforced Polymer Thermal Breaks

In a study performed by Goulouti et. al. [27], the thermal performance of a fiber-reinforced polymer thermal break balcony connection was evaluated. The study evaluated the impact of this improved thermal break on the energy balance of a typical residential building located in Switzerland. A case study was performed, and the thermal losses through the balcony connections as well as the building's total transmission losses and heating needs were estimated and compared.

Building energy simulations were performed using LESOSAI, a software used for thermal balance calculation and life cycle analysis of buildings. The case study was performed for three different thermal break thermal transmittance values, equal to 0.3, 0.15 and 0.1 W/mK, corresponding to the SIA limit and target values and the optimized thermal break, respectively. Each thermal break was modelled with three different building envelopes of varying performance.

The results show that the reduction in heating needs from implementing a thermal break with lower thermal transmittance was most apparent for the highest efficiency building envelope, and less apparent for the lower efficiency building envelope. For the lowest efficiency building envelope, a nearly 13% reduction in heating needs was seen when improving the thermal bridge transmittance from 0.3 to 0.1 W/m·K Comparatively, a nearly 27% reduction was found when the same thermal bridge transmittance

decrease was modelled for the most efficient building envelope. Overall, the total losses through thermal bridges in comparison to the building's total transmission losses decreased by a factor of approximately three when the linear thermal transmittance of the thermal break was decreased from 0.3 to 0.1 W/m·K. The results from this study show the benefits of including an FRP reinforced thermal break in a building envelope on the building's total energy needs.

2.4.4 Commercially Available Thermal Breaks

Commercially available balcony slab thermal breaks are typically developed and supplied by companies involved in providing construction components for building statics and building science solutions. Many companies involved have originated in Europe and have expanded to provide international services, including in North America. Although the commercially available balcony thermal breaks provide excellent thermal and structural properties, they have yet to become a commonplace design element in the North American construction industry. This is mainly due to the large initial installation cost associated with the manufactured thermal breaks.

Most balcony thermal break products follow a similar configuration to one another. The main body is typically composed of an insulating material that may provide some, but minimal, structural capacity. The thickness of this insulating body may range from 60 to 120 mm. Structural integrity between the balcony slab and interior structure is provided by reinforcement traversing the insulation body. Tension and shear reinforcement is typically provided by stainless steel reinforcement, providing a lower thermal conductivity than carbon steel. Compression resistance is typically provided by special compression modules made of high strength concrete or stainless steel compression studs, reducing rebar congestion and simplifying installation. Several products are available with an additional fire protection board on the top and bottom surface of the insulation material to achieve fire code requirements. A summary of several industry available balcony thermal break products and their components is presented below in Table 4.

Table 4 Summary of industry available balcony thermal break products

Company	Product	Insulating Body	Tension Reinforcement	Shear Reinforcement	Compression Reinforcement
Schöck, Germany [28]	Isokorb	Graphite-enhanced Expanded Polystyrene 80 mm min.	High Strength Stainless Steel	High Strength Stainless Steel	Steel Fiber Reinforced UHPC[1]
Ancon, UK [29]	Isotec	Rockwool® Mineral Wool 80 mm	1.4301 Stainless Steel	1.4301 Stainless Steel	12mm diameter High Resistance 1.4301 Stainless Steel Bars with Hot-forged Heads
	Isolan	Polystyrene with High-density Polyethylene Rail Top Edge 60 mm	Grade B500B to BS4449 Carbon Steel	Grade 1.4362 Stainless Steel	Grade B500B to BS4449 Carbon Steel
Halfen, Germany [30]	HIT	Polystyrene	Carbon Steel connected with High Grade Stainless Steel tube	High Grade Stainless Steel	High Grade Stainless Steel Pressure Pads
H-Bau, Germany [31]	Isopro	NEOPOR Expanded Polystyrene 80 mm	B500B Steel and B500NR Stainless Steel	B500B Steel and B500NR Stainless Steel	HS Concrete Pressure Element or Steel Pressure-bearing Plane
	Isomaxx	NEOPOR Expanded Polystyrene 120 mm	B500B Steel and B500NR Stainless Steel	B500B Steel and B500NR Stainless Steel	HS Concrete Pressure Element or Steel Pressure-bearing Plane

From a structural design perspective, designing for strength within a thermal break is fairly straight forward. Alternatively, serviceability requirements such as deflection and rotation become more complex to account for due to the complexity of the thermal break system. The methods to account for additional deflection caused by the thermal break are provided in product brochures and literature for several manufactured thermal breaks, and are summarized below in Table 5. Some companies require design data and will advise

[1] UHPC Ultra High Performance Concrete

upon calculated deflections without providing the explicit methods. A common theme is that the balcony will be installed with a precamber to account for the additional deflection caused by the thermal break.

Table 5 Methods for determining deflection provided by manufacturers of thermal breaks

Product	Method
Schöck Isokorb [28]	Calculate deflection caused by connection as $w = (\tan \alpha)\ (l)\ (M_n / M_r)\ (1.4 / 100)$ l = cantilever length M_n = nominal unfactored moment resistance M_r = ultimate factored moment resistance α = obtained from selection table Deflection values used to estimate the required camber.
Ancon Isotec [29]	Calculate deflection for concrete slab and multiply by 1.2. Apply necessary pre-camber to account for deflection.
Ancon Isolan [29]	Ancon will advise on calculated deflections upon receipt of relevant design data.
Halfen HIT [30]	Not mentioned.
H-Bau Isopro [31]	Calculate deflection caused by connection as $w(mm) = (\tan \alpha)\ (m_{Ed} / m_{Rd})\ l\ (10)$ l = cantilever length m_{Ed} = bending moment for determining excess height resulting from Isopro element, governing load combination determined by designer m_{Rd} = design moment of Isopro from provided design tables $\tan \alpha$ = deformation factor obtained from selection table Deflection values used to estimate the required camber.

3 Experimental Program

The following section outlines the processes and procedures followed in this experimental program. The approach to designing the system is first provided. The experimental testing details are given for first thermal testing, including the approach for thermal modeling, followed by structural testing. The methods of preparing the test samples and their details are lastly included.

3.1 System Design

Since guidelines and standards do not address methods for designing balcony thermal breaks, a novel approach had to be taken towards design. The thermal breaks were designed first and foremost based on structural requirements, while keeping in mind the co-existing requirement of reducing thermal conductivity across the break. Designs for a typical residential balcony slab with a thermal break for each reinforcement type were developed in order to facilitate scaling and testing of the system.

The carbon steel and stainless steel reinforced concrete slabs are designed according to the CSA A23.3-04 standard within the Concrete Design Handbook, Third Edition [32]. The GFRP reinforced concrete slab is designed according to the CSA S806-12 standard [33] with references to the Design Manual for Reinforcing Concrete Structures with Fibre Reinforced Polymers provided by ISIS Canada [34]. The strength capacity of the thermal break joint is estimated using approaches from several design codes, as explained in the following sections. Ultimate strength design and deflection calculations for the full-scale balcony slab containing each of the three reinforcement types may be found in Appendices A.1, A.2, and A.3.

3.1.1 Design Loads and Assumptions

Design loads were based on the requirements of the 2010 National Building Code of Canada (NBCC) [35]. A full summary of the load calculations is provided in Appendix A.4. The typical residential balcony for which

design loads were determined was assigned a cantilevered length of 1.83 m (6 feet), and a corresponding depth of 190 mm. Design loads were calculated for a one meter wide design section.

The thermal break connection was designed to resist shear from the external balcony only. This assumption is justified for a building with exterior insulation in which the thermal break is installed in-plane with the external insulation and exterior to the supporting column, as shown in Figure 4.

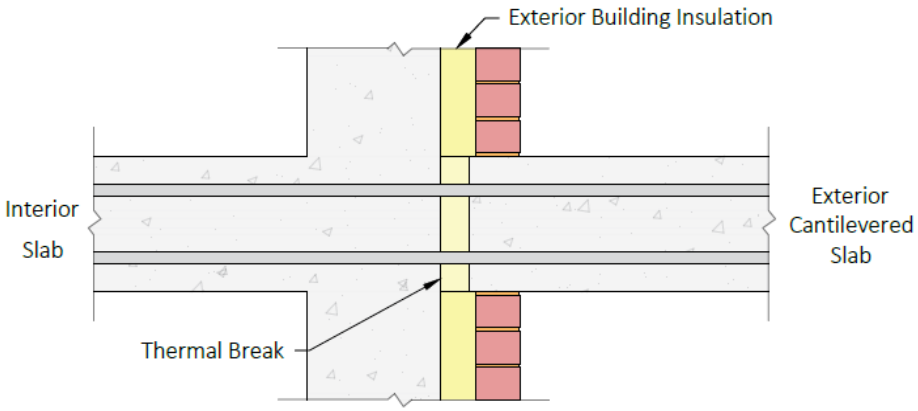

Figure 4 Thermal Break Location

The bending moment acting on the thermal break was taken as that caused by the loads acting on the cantilevered balcony slab. For simplicity, loads acting on the internal floor slab were neglected. In the design of a full building complex, it would be required to ensure that the reinforcement required in the internal slab due to the negative moment at the support is not larger than that required in the thermal break due to the cantilevered balcony loads.

The following loads were included in design: self-weight of the concrete slab, self-weight of a balcony guardrail, live load due to use and occupancy, live load acting on the guardrail, and snow load. Loads not considered in design include wind and earthquake loads.

Dead loads included in design are the self-weight of the concrete slab and the self-weight of the balcony guardrail. The self-weight of the concrete slab is calculated as the dimensional volume of the cantilevered

slab multiplied by a reinforced concrete density of 25 kN/m^3 [36], acting as a uniformly distributed load on the member. The self-weight of the balcony guardrail is representative of a steel framed railing containing glass panels with a height of 1.070 m as required by the NBCC [35]. The self-weight is approximated based on the weight of double ¾" glass panels, weighing 0.478 kN/m^2 per panel [37], to account for the combined weight of a single glass panel with steel framing. This load is treated as a concentrated load acting at the cantilevered edge of the balcony.

The live load due to use and occupancy acting on the balcony surface is obtained for the case of an exterior balcony from Table 4.1.5.3 of the National Building Code of Canada (NBCC) [35], which provides the specified uniformly distributed live loads on an area of floor or roof. The live load acting on the guardrail is obtained according to section 4.1.5.14 of the NBCC, considering the most critical load scenario between a vertical load acting on the guardrail, and a horizontal load acting outwards at the minimum required height of the guard (1.070 m).

Snow load is calculated according to the NBCC [35]. The balcony is assumed to be situated in Winnipeg, Canada for snow and rain load data selection.

Load factors are obtained from Table 4.1.3.2.A of the NBCC [35]. Load case 2, with a dead load factor of 1.25, live load factor of 1.5, and companion load factor of 0.5 produces the critical load case for design.

3.1.2 Thermal Break Bending Moment Capacity

For the initial design, the strength of the insulating thermal break material was assumed to be negligible and the forces transferred across the thermal break were assumed to be resisted solely by the reinforcement at this cross-section. The intent in this is to provide a conservative approach to design such as would be taken by engineers when designing a new system. Therefore, the moment capacity of the section with the thermal break is calculated based on first principles of equilibrium in a cross-section as a

force couple acting through the reinforcement, inducing tension in the upper reinforcement and compression in the lower reinforcement. The moment arm, d, between the tensile and compressive forces is taken as the distance from centroid to centroid of the reinforcement layers. Calculating the moment capacity at the cross-section of the thermal break using methods from the concrete design handbook is not possible since these methods include empirical equations dependant on the strength and properties of concrete.

The strengths of carbon steel and stainless steel under both tension and compression are taken to be their respective yield strengths. As discussed in Section 2.3.2, the contribution of FRP to compression capacity is typically neglected in design, however literature provides approximate values for the compressive properties of FRP as a function of its tensile properties. For the design of the thermal break moment capacity, the compressive strength of GFRP rebar is assumed to be 60% of its ultimate tensile strength and the compressive modulus is taken as 80% of its tensile modulus.

The design of longitudinal tensile and compressive reinforcement for steel and stainless steel reinforced sections are approached in the same manner. The reinforcement area in a one meter wide design section required to resist the factored bending moment is first determined. A reinforcement spacing is then selected to provide at least the minimum required reinforcement. Based on guidance from industry contacts provided by Crosier Kilgour & Partners Ltd., 16 mm diameter reinforcement was selected for both steel and stainless steel reinforced sections. The reinforcement design is provided for all rebar types in Table 6. A concrete cover of 40 mm was chosen for exterior exposure conditions and was used for all three reinforcement types.

Table 6 Rebar reinforcement ratio design

Reinforcement Type	Bar Size	Bar Diameter [mm]	Spacing [mm]
Carbon Steel	10M	16	167
Stainless Steel	10M	16	250
GFRP	25M	25	250

The design of GFRP reinforced members requires a different approach, since serviceability requirements typically govern in design due to the low modulus of elasticity of GFRP. Therefore, the spacing of GFRP reinforcement at the location of the thermal break was selected based on deflection requirements, as provided in Section 3.1.5. Once selected, the moment resistance of the thermal break was calculated to ensure its adequacy.

3.1.3 Thermal Break Shear Force Capacity

Available technologies for reducing thermal bridging in a reinforced concrete balcony slab typically use inclined shear bars to provide shear capacity. This increases the amount of reinforcement traversing the thermal break, which in turn increases the overall thermal conductivity of the system. In order to optimize thermal insulation capacity, shear bars were eliminated from the designs in this project. Instead, the connection was designed to provide shear capacity through shear friction of the longitudinal reinforcement.

The shear capacity of steel and stainless steel rebar, V_r, is estimated using section 13.4.4 of the Canadian Standard CSA S16-09 for the design of steel structures [38], which provides the shear resistance of a steel pin in Equation 1 as

$$V_r = 0.66\,\phi_s\,A_s\,f_y \tag{1}$$

where ϕ_s is the material strength reduction factor for steel and is taken as 1 for experimental testing, A_S is the cross-sectional area of the steel, and f_y is the yield strength of the steel.

There are currently no theoretical models to predict the transverse shear strength of FRP dowels [39]. Based on literature and available data of similar FRP products [40] [41], the shear strength of GFRP rebar was estimated at 10% of its ultimate tensile strength. For strength calculations, the shear capacity of GFRP was taken as 10% of the already reduced compressive strength, which was 60% of the ultimate tensile strength. Therefore, the shear strength was taken as 6% of the rebar's ultimate tensile strength in these designs.

The designs were checked to ensure that the rebar would not fail under combined shear and tensile loading. The interaction equation in Equation 2 was used to determine the capacity of a dowel subjected to shear and tensile forces [42] [43]:

$$(\frac{V_f}{V_r})^2 + (\frac{T_f}{T_r})^2 \leq 1.0 \quad (2)$$

where V_f and T_f are the factored shear and tensile forces, respectively, and V_r and T_r are the shear and tensile capacity of the material, respectively. Given that this relationship is based on the maximum normal stress and maximum shear stress theories of a material [42], it can be applied in the design of steel, stainless steel, and GFRP rebar subjected to combined tensile and shear loading.

3.1.4 Reinforced Concrete Slab Capacity

The design of the full scale cantilevered reinforced concrete slab involved the design of two reinforcement cross-section, as labelled in Figure 5. Section 1 adjacent to the thermal break was checked to ensure that the reinforcement selected across the thermal break was adequate to resist the factored bending moment and factored shear force within the concrete section.

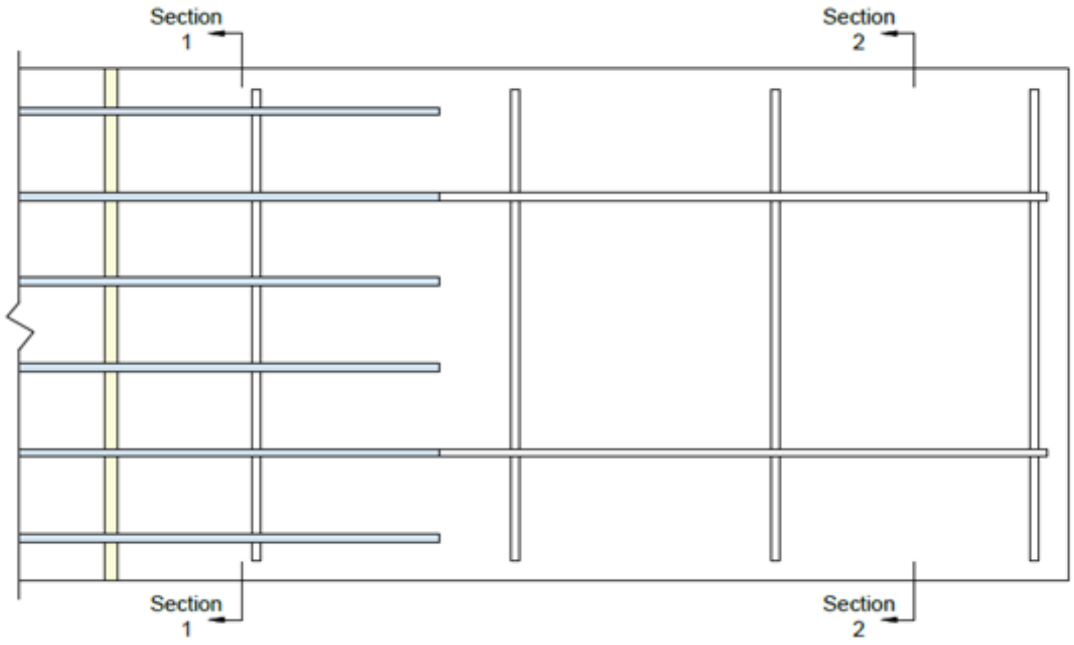

Figure 5 Section 1 and Section 2 as labelled for the design of reinforcement in the cantilevered reinforced concrete balcony slab

For the GFRP reinforced balcony, the entire balcony was designed as Section 1 due to deflection constraints, meaning that the reinforcement traversing the thermal break is continuous to the cantilevered edge of the balcony.

For the steel and stainless steel reinforced balconies, an additional concrete cross-section was designed for the cantilevered edge of the balcony. This cross-section is referred to as Section 2 and was designed to contain the minimum required reinforcement area. The moment capacity of Section 2 was then calculated. Section 1 reinforcement was extended from the thermal break to the location within the slab that is subjected to the moment capacity of Section 2, plus the required embedment length. The purpose of reducing the reinforcement density at Section 2 is to reduce the amount of reinforcing materials and therefore reduce the initial cost of constructing the balcony.

3.1.5 Serviceability Requirements

Serviceability requirements in reinforced concrete design typically include limitations on the deflection of a structural member and on crack widths within the concrete. The crack widths were not checked in these designs, as they would dictate a significantly higher and unrealistic reinforcement density compared to all other design checks, and are typically neglected in industry applications for this reason [44]. Therefore the deflection under service load was the only serviceability requirement checked in these designs.

In order to accommodate the difference in stiffness introduced by the thermal break, deflections were calculated using moment area theorems. It is noted that the moment area theorems do not consider the lack of bond between thermal break and concrete, which would reduce stiffness of the member and allow for opening between the thermal break and concrete. The experimental deflections are therefore anticipated to be larger than calculated deflections. The obtained deflections are summarized below in Table 7.

Table 7 Calculated maximum deflections for full-scale designs

Reinforcement Type	Deflection introduced by thermal break [mm]	Deflection introduced by length of slab [mm]	Total maximum deflection [mm]
Carbon Steel	1.29	7.29	8.58
Stainless Steel	1.93	9.23	11.17
GFRP	2.62	10.81	13.44

The permissible deflection for a typical balcony floor slab is provided by CSA to be the clear span length of the floor slab divided by 360 [33]. This produces a maximum allowable deflection of 5.1 mm for the design balcony, which is exceeded by all designs as shown above. It should be recalled that most existing manufactured balcony thermal breaks are installed with a precamber to account for their large deflection. Therefore the calculated deflections using moment area theorems will be accommodated by precamber.

As mentioned previously, serviceability requirements were also used to determine a reinforcement spacing for the GFRP reinforced slab. This was done by calculating the deflection for a GFRP reinforced slab with different reinforcement spacing and selecting the design that provided a reasonable deflection, determined to be not more than 25% larger than the deflection obtained for stainless steel, while minimizing the total reinforcement ratio. The design was then checked for strength requirements, as described in section 3.1 previously.

3.1.6 Stresses on Thermal Break Material

As an additional check, maximum stresses on the thermal break material were calculated for service and ultimate conditions. This was done by assuming the strength capacity of the thermal break to be equal to zero, therefore assuming that forces on the cross-section are transferred solely by the reinforcement. Based on this, the stress in the reinforcement was calculated in order to calculate the corresponding strain. Based on the strain in the reinforcement, the rotation of the cross-section was calculated. From this the rotation of the cross-section and maximum strain in the thermal break material were calculated, along with corresponding stress in the thermal break. The obtained stress values and their percentage of the material's ultimate stress are provided below in Table 8.

Table 8 Thermal break material stress calculations

	At Service Load		At Ultimate Load	
Reinforcement	Stress [MPa]	% Ultimate	Stress [MPa]	% Ultimate
Carbon Steel	0.9	6.2	1.2	7.8
Stainless Steel	1.4	9.3	1.7	11.8
GFRP	2.7	18.3	8.6	58.1

As these calculations neglect the stiffness of the thermal break material, they should provide an over-estimation of the stress on the thermal break. Given this, and the low stress values obtained in calculations, the stresses on the thermal break are deemed acceptable for the designs.

3.1.7 Test Sample Design and Dimensioning

In order to facilitate structural and thermal testing, sample sizes of the balcony designs were constructed. Due to the nature of thermal testing and the error which it would incorporate into the results, scaling of the system was not possible. Therefore, the dimensions of the design were kept to scale and a sample size was extracted.

The full 190 mm depth of the slab was maintained. A sample width of 500 mm provided a symmetric reinforcement distribution for each reinforcement spacing obtained in design. The thermal break was placed at mid-length of the samples. The sample length was then dictated by the longest of the required reinforcement embedment lengths, equal to 740 mm, meaning that the reinforcement must extend at minimum this length into the concrete to develop full capacity at the thermal break. A sample length of 1600 mm was selected, providing an embedment length of 747.5 mm to either side. The resulting sample dimensions are provided below in Figure 6.

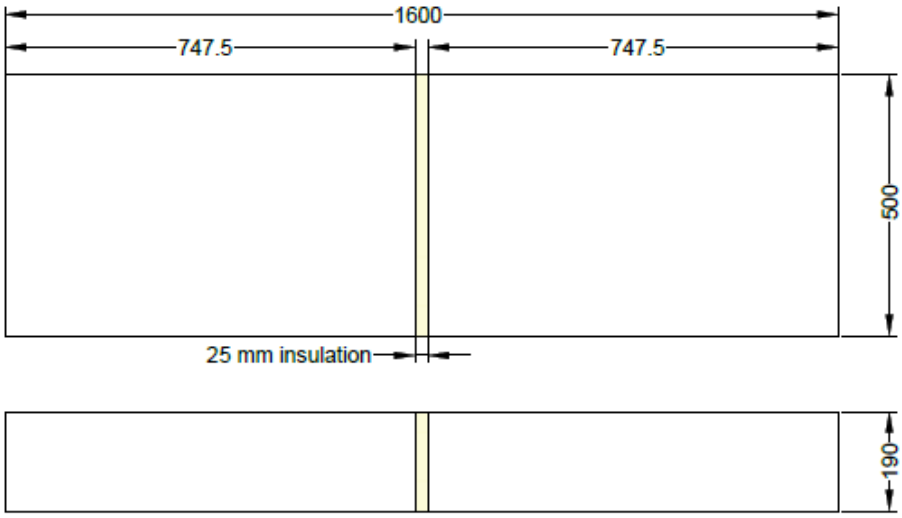

Figure 6 Test sample dimensions, in mm

Samples tested without a thermal break were assigned the same reinforcement as samples designed with the thermal break. These samples were simply constructed excluding the thermal break, and the same

location at the mid-length of the sample was considered as the connection during testing. Maintaining the same reinforcement and only including or removing the thermal break allows the experiment to isolate the effects of including the thermal break material.

3.1.8 Test Sample Strength Calculations

Material strength testing was performed on steel and stainless steel reinforcement samples, as well as on concrete cylinders cast during casting of the test samples, in order to determine the actual strengths of the materials. The data from rebar tensile testing and concrete cylinder testing is included in Appendix A.5 and A.6, respectively. Material strength testing was not performed on the GFRP reinforcing bars since the required sample length could not be accommodated by the available testing facilities, and the strength of the GFRP was taken as that provided by the manufacturer.

Tensile testing of the steel and stainless steel reinforcement was performed according to ASTM A370 Standard Test Methods and Definitions for Mechanical Testing of Steel Products [45]. For regular steel, the 2% offset method was used to obtain the yield stress and strain from the obtained test results. Due to the roundhouse shape of the stress strain curve and the difficulty in isolating the initial slope, the 0.5% extension method was used to determine the yield stress and strain for stainless steel reinforcement. The yield strength for carbon and stainless steel specimens were found to be 462 MPa and 554 MPa respectively.

Compressive concrete cylinder testing was performed according to ASTM C39 Standard Test Method for Compressive Strength of Cylindrical Concrete Specimens [46]. At the time of structural testing, the concrete compressive strengths were 39 MPa and 44 MPa for samples with and without a thermal break, respectively. The concrete density was also evaluated as 2331 kg/m^3 and 2403 kg/m^3 for samples with and without a thermal break, respectively, which correlate to thermal conductivities of 1.88 W/mK and 2 W/mK.

Strength calculations were re-done for the sample sizes and are included in Appendix A.7, A.8, and A.9. A summary of the ultimate strength capacity of the sample types is provided in Table 9 below. For samples without the thermal break, the capacity at the supposed joint location is equal to that shown in the column labelled "Slab Adjacent to Thermal Break". The carbon steel and stainless steel samples, both with and without the thermal break, are anticipated to fail by yielding of the steel at the location of the thermal break. The GFRP reinforced samples are anticipated to fail by shearing of the concrete.

Table 9 Ultimate strength capacity of test samples

	Thermal Break	Slab Adjacent to Thermal Break	
Reinforcement	M_r [kN-m]	M_r [kN-m]	V_r [kN]
Carbon Steel	26.1	37.1	88.7
Stainless Steel	20.8	30.0	81.6
GFRP	51	65.5	48.8

Deflections were calculated for each sample type, based on moment area theorems. A summary of the load-deflection curves for each sample type is provided in Appendix A.10. The calculated deflections up until failure load (yielding for steel and stainless steel, concrete shear failure for GFRP) are provided below in Table 10, along with the calculated failure load. Since the calculated deflections do not take into account the lack of bond between thermal break and concrete, it is anticipated that experimental deflections will exceed those calculated.

Table 10 Theoretical deflection at failure load for test samples

	With Thermal Break		Without Thermal Break	
Reinforcement	Failure Load [kN]	Deflection at Failure [mm]	Failure Load [kN]	Deflection at Failure [mm]
Carbon Steel	29.6	2.38	41.6	2.53
Stainless Steel	25.6	3.06	36.2	3.24
GFRP	43.3	7.71	43.3	5.88

3.2 Thermal Test Program

3.2.1 Thermal Testing Setup

Thermal testing was carried out using facilities located at Red River College in Winnipeg, Canada. A dual-sided thermal chamber was used to simulate the conditions of a balcony in service, being exposed to warm interior temperatures on one side and cold exterior temperatures on the other. This therefore simulated the highest heat transfer scenario, which would occur in cold winter months. The interior design temperature was selected as 21˚C, and the exterior design temperature for Winnipeg of -31˚C was used.

The test samples were installed within the thermal chambers and a wall of 100 mm wide rigid extruded polystyrene insulation, with an R-value of 20, was installed around the samples to separate the two thermal environments. The thermal break was aligned with the cold chamber, as shown in Figure 7, to simulate the alignment of the thermal break when installed in an externally insulated building. The far edges of the samples are supported by screw pins placed at each corner (two supports per slab) with a 50 mm by 50 mm section of Armatherm measuring 25 mm in depth placed between the surface of the screw pin and the sample to eliminate thermal effects from the supports.

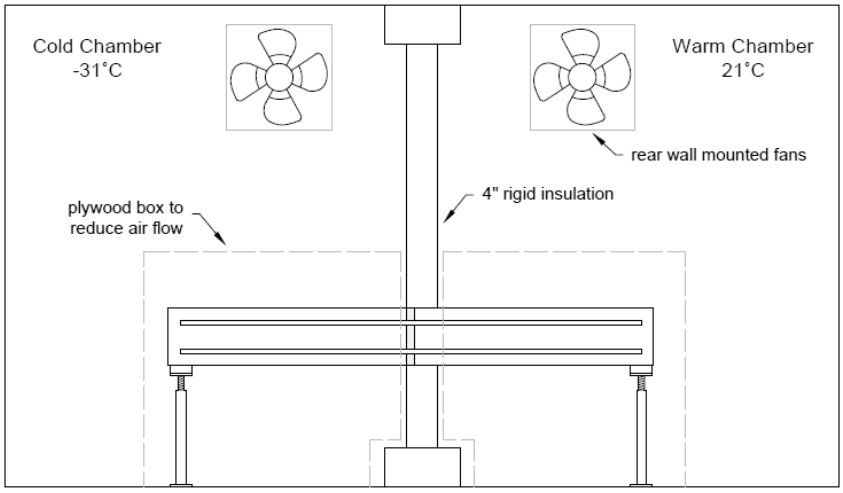

Figure 7 Thermal test chambers

Figure 8 shows the junction between the top of the two test samples and the 4” rigid insulation wall in the thermal chambers, as well as the 4” rigid insulation placed between the two samples. A 25 mm gap was left between the sample and insulation wall, which was filled with a polyurethane spray foam sealant to provide insulation directly against the samples, as shown in Figure 8. Caulking sealant was applied at all edges between the spray foam, samples, and insulation wall to ensure airtightness between the two thermal environments. A smoke wand was used to identify any remaining locations of air flow so that they may be sealed with the caulking. The rigid insulation between the two samples was placed directly against the samples with caulking applied along all edges to ensure a proper seal.

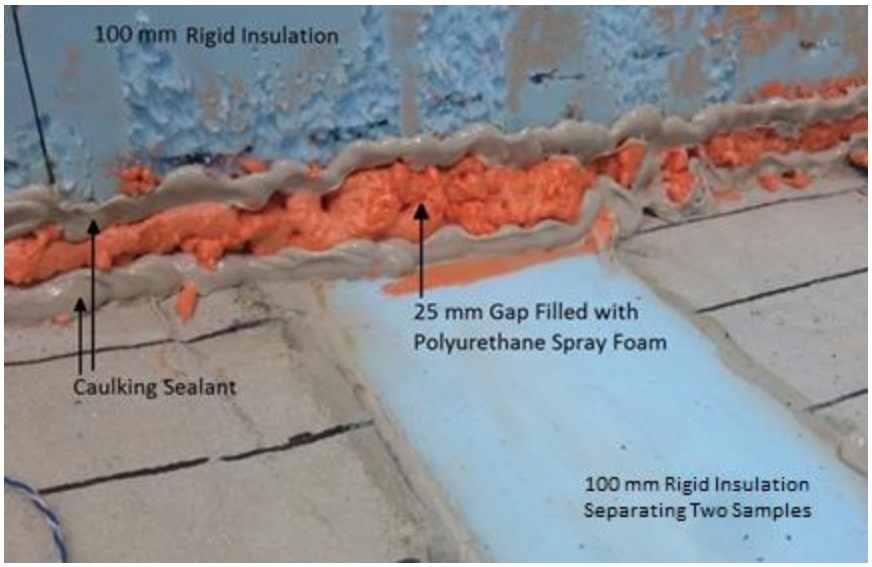

Figure 8 Junction between top of test slabs and 4" rigid insulation wall in thermal test chambers, showing caulking and spray foam

In order to simulate the primarily longitudinal heat flow which would occur in an installed balcony with a width significantly larger than its cantilevered length, the sides of the 0.5 m wide test samples were insulated, as shown in Figure 9. Sections of 100 mm thick rigid insulation were adhered using construction adhesive to the sides of the test samples, and caulking was applied between the edges of this insulation and the concrete to eliminate any possibility of airflow between the insulation and the sample. Two samples

were tested at once within the chamber, side by side, with one section of 100 mm wide rigid insulation installed between them, as shown in Figure 9.

Figure 9 Test samples in thermal chamber showing longitudinal side insulation

The temperature within each environmental chamber was regulated by a fan positioned on the rear wall, as shown in Figure 7, blowing air of the required temperature into the chamber. Because of this there was a pronounced effect of uneven airflow within each chamber and along the surfaces of the unsheltered samples, resulting in uneven convective conditions. To eliminate this convection and provide consistent exposure conditions along all surfaces, a shelter built from plywood was installed around the samples within each environmental chamber. This allowed the temperature of air in contact with the samples to reach the design temperatures while eliminating the air flow. In order to monitor the temperature inside relative to outside of the shelter, one 10k ohm thermistor with a tolerance of ±0.2˚C was installed both inside and outside of the shelter as shown in Figure 10 and Figure 11.

Figure 10 Plywood shelter with rear wall removed showing location of interior temperature sensor

Figure 11 Plywood shelter with rear wall installed showing location of exterior temperature sensor

3.2.2 Sample Instrumentation for Thermal Testing

In order to record the temperature profiles of the samples, 10K ohm thermistors with a tolerance of ±0.2˚C were installed on their surface and embedded within the concrete. The thermistors were purchased from Digi-Key and soldered onto wire at the University of Manitoba.

Prior to casting of the 18 samples, one steel reinforced mock-up sample was cast and instrumented with an excess amount of thermistors. This was used to determine an efficient thermistor layout for the remaining 18 samples that would provide a satisfactory temperature profile while minimizing the number of sensors required. The thermistor layout for the mock-up sample is provided in Figure 12.

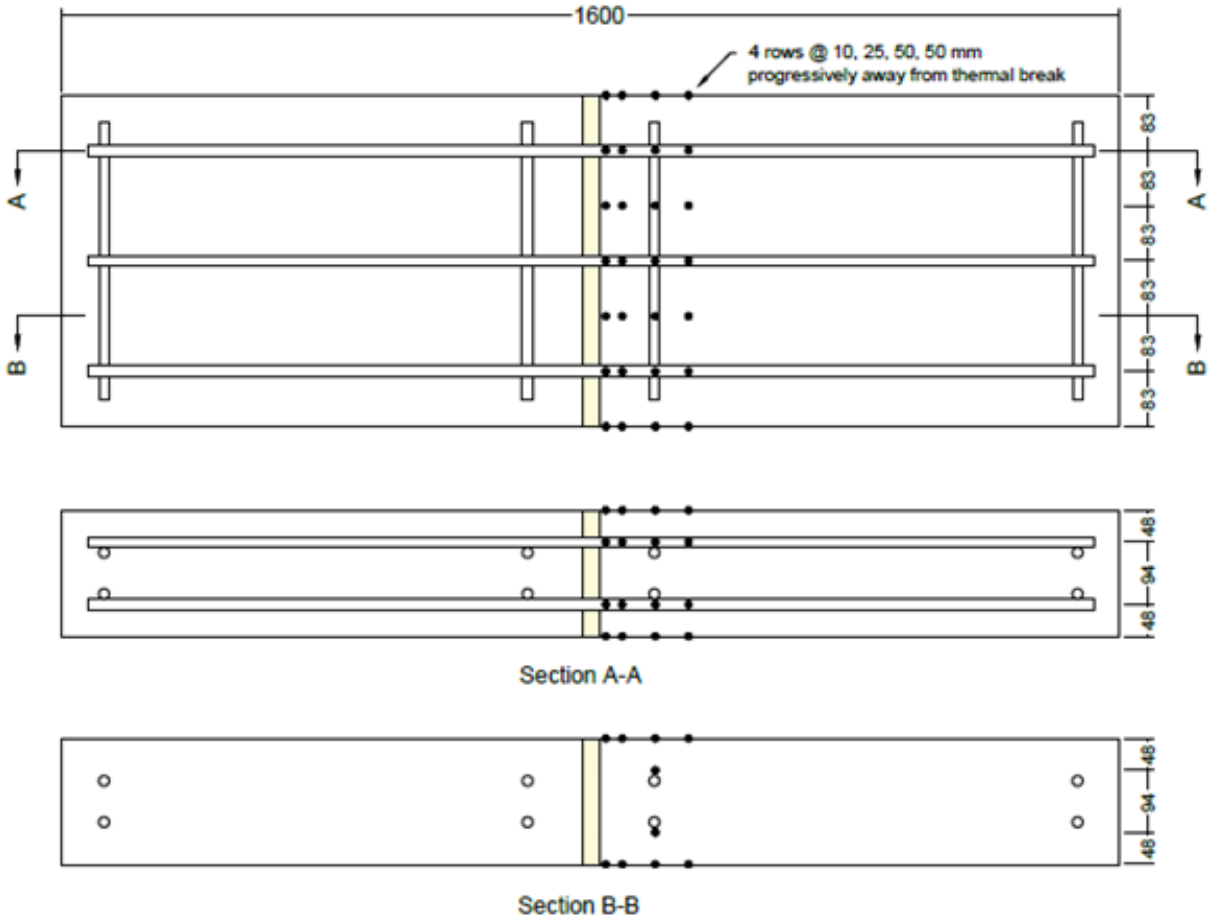

Figure 12 Thermistor layout for mock-up sample, dimensions in mm

In order to reduce material costs, only one side of the sample was equipped with sensors. For testing, the mock-up was first oriented and tested with the instrumented side extending into the warm chamber. The sample was then reoriented and tested with the instrumented side extending into the cold chamber. The mock-up sample was installed with the same 100 mm rigid insulation adhered to the exposed longitudinal

sides as was used for the final 18 samples. The data acquisition units were located inside of the chamber, as shown in Figure 13.

Figure 13 Mock-up thermal test on warm side

Figure 14 displays the longitudinal distribution of temperatures along the mid-line of the slab on the warm side. Temperature increased as distance from the thermal break increased, indicating longitudinal heat flow through the slab. Of interest is the modest increase in temperature from the top surface to the bottom surface of the slab. This is concluded to be due to the buoyancy of warm air, as warmer air is unable to rise away from the bottom surface of the slab and is therefore entrapped.

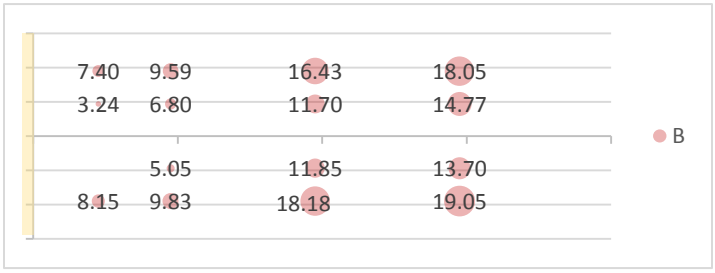

Figure 14 Longitudinal cross-sectional temperatures, in ˚C, on warm side of mock-up sample, taken from mid-line of the sample

Figure 15 displays the temperature distribution of the transverse cross-section of the slab located 10 mm from the thermal break, and it is from these results that the uneven convection introduced by the blower fan was identified. In Figure 15 an increase in temperature from the left-hand side of the slab to the right-

hand side is present. This is concluded to be due to air wash from the blower fan acting from the left-hand side of the slab.

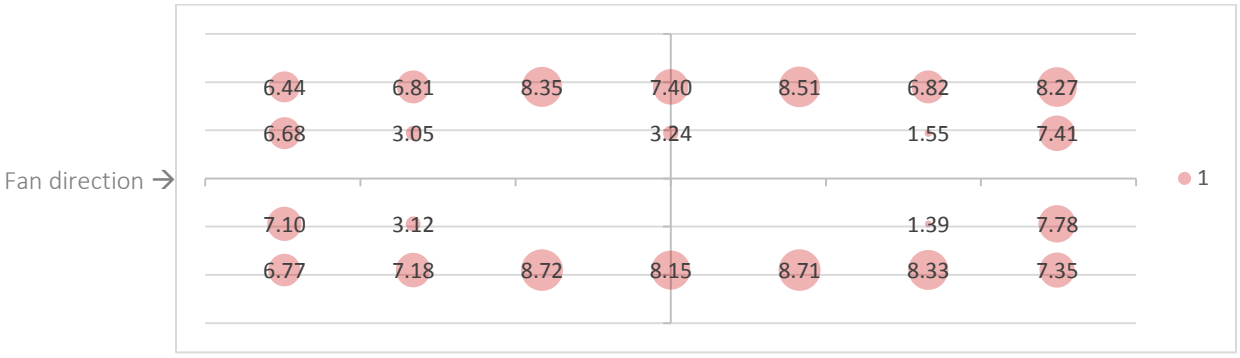

Figure 15 Transverse cross-sectional temperatures, in ˚C, on warm side of mock-up sample, distanced 10 mm from the thermal break

Figure 16 displays the distribution of temperatures along the mid-line of the slab on the cold side. Similar to the results from the first test, there is a decrease in temperature as distance away from the thermal break increases, again showing the longitudinal heat flow. The modest increase in temperature from the top surface to the bottom surface of the slab is again present.

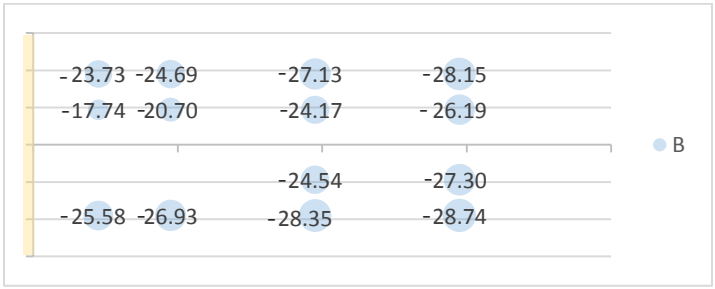

Figure 16 Longitudinal cross-sectional temperatures, in ˚C, on cold side of mock-up sample, taken from mid-line of the sample

Figure 17 displays the temperature distribution of the transverse cross-section of the slab located 10mm from the insulation joint on the cold side. Contrary to what was observed on the warm side of the slab, the temperatures are relatively symmetric about the vertical centerline, indicating that the convective film coefficient was relatively consistent along the slab's surface in comparison to the behaviour seen in the first test.

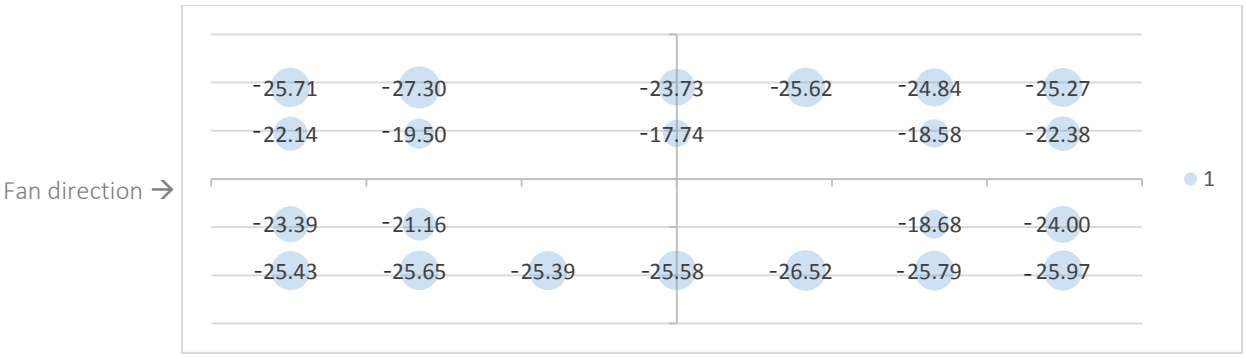

Figure 17 Transverse cross-sectional temperatures, in ˚C, on cold side of mock-up sample, distanced 10 mm from the thermal break

The results from the mock-up thermal tests indicated that uneven airflow surrounding the samples needed to be reduced, resulting in the construction and use of the plywood shelter shown in Figure 10 and Figure 11. For the final thermistor layout it was decided to only instrument the top half of each sample and to assume vertical symmetry in the temperature profile when comparing experimental results to those obtained through modeling. This eliminated the need to include different convective exposure conditions on the top and bottom of the samples in the computer models.

Figure 18 shows the final thermistor layout for GFRP reinforced samples, and the remaining drawings for all sample types may be found in Appendix A.11. Both the warm and cold sides were instrumented, eliminating the need to test each sample twice.

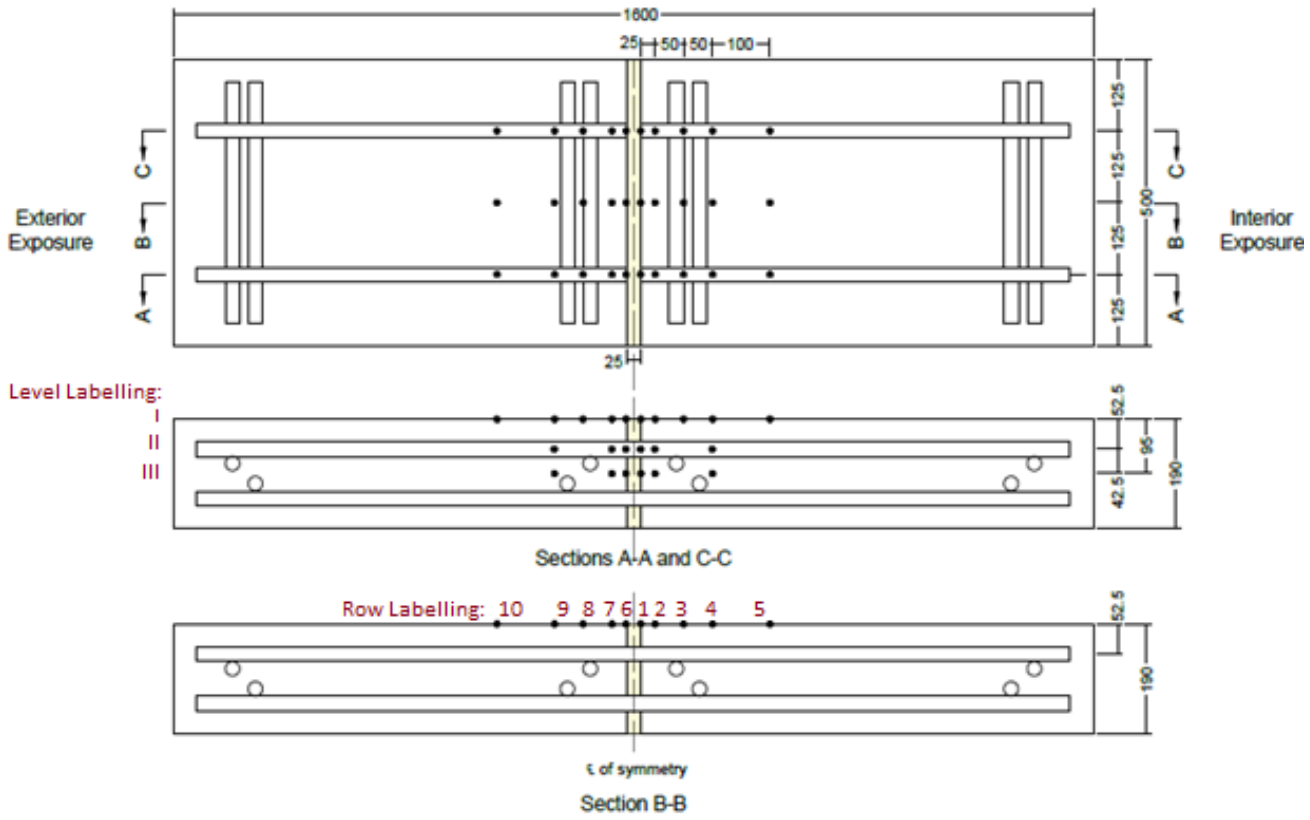

Figure 18 Thermistor layout and labelling for GFRP reinforced samples

The surface mounted thermistors were adhered to the surface of the concrete. Those located at the level of the reinforcement were tied to the reinforcing bars using cable ties. The thermistors suspended between the two reinforcing bars and touching the thermal break material were adhered to the thermal break. The remaining thermistors at this level were suspended between the two reinforcing bars using cable ties, as shown in Figure 19. For samples without the thermal break, all thermistors suspended between the two bars are suspended with cable ties.

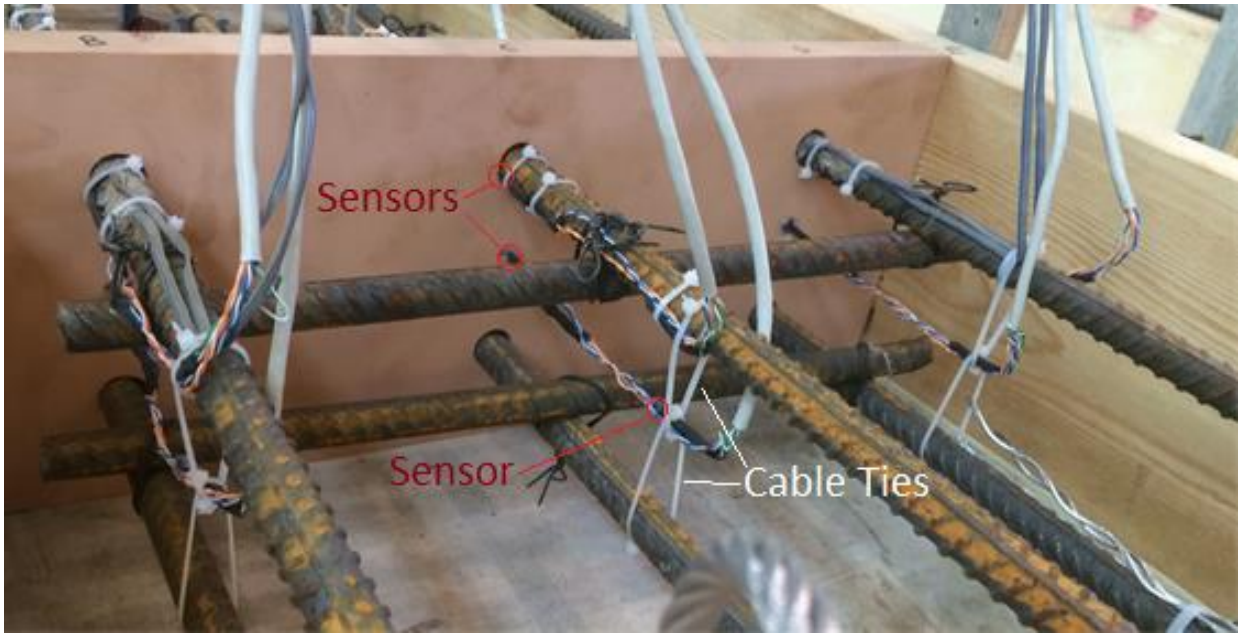

Figure 19 Thermistor installation method inside of samples

During casting of the concrete, the thermistor cables were lifted up and away from the samples by a temporary bridge constructed onto the formwork, as shown in Figure 20. This allowed the cables to exit the concrete as close to the sensors as possible. Extra care was taken during casting to avoid damaging the internal thermistors, and the concrete was not vibrated within the instrumented area but instead just outside of it, close enough to ensure adequate concrete compaction within all areas of the samples without damaging the thermistors.

Figure 20 Formwork prior to casting including thermal sensors

3.3 Thermal Modelling

Steady state thermal modelling was performed using Heat3 8.02, a three-dimensional finite element heat transfer program developed by BLOCON (2017). The models were built according to ISO 10211 (2007) [47], the international standard for modelling thermal bridges in building construction. Each reinforcement type was modelled with and without a thermal break, to allow for a comparison between the temperature profiles obtained through experimental testing with those found in modelling. The purpose of thermal modelling was to simulate the conditions occurring within the experimental testing chambers in order to validate the results and further quantify the physical properties of the different thermal breaks.

3.3.1 Numerical Calculation Method

The calculation method performed in Heat3 is governed by the following partial differentiation equation for temperature T(x,y,z,t) in Equation 3 [48]:

$$\frac{\delta}{\delta x}\left(\lambda\frac{\delta T}{\delta x}\right)+\frac{\delta}{\delta y}\left(\lambda\frac{\delta T}{\delta y}\right)+\frac{\delta}{\delta z}\left(\lambda\frac{\delta T}{\delta z}\right)+I(x,y,z,t)=C\frac{\delta T}{\delta t} \quad (3)$$

in which I, (W/m^3), is the rate of internal heat generation, λ, (W/mK), is the material thermal conductivity, and C, (J/m^3K), is the volumetric heat capacity. To derive a solution, this partial differentiation equation is discretized to produce a computational mesh of approximated values. In the present case it is assumed that there is no internal heat generation, therefore I = 0.

For a given computational cell with dimensions Δx_i, Δy_j, and Δz_k there are six adjacent cells. The directional heat flow in watts from one cell (I,j,k) to another (I,j,k+1) in each of the six directions is obtained by multiplying the thermal conductance by the temperature difference between the two cells as follows in Equation 4:

$$Q_{i,j,k+1/2} = K_{i,j,k+\frac{1}{2}}(T_{i,j,k} - T_{i,j,k+1}) \tag{4}$$

where $K_{i,j,k+1/2}$ is the material thermal conductance between the two cells. This is calculated as shown in the Equation 5 for heat flow in the z-direction through the area $\Delta x_i \bullet \Delta y_j$:

$$K_{i,j,k+1/2} = \frac{\Delta x_i \, \Delta y_j}{\frac{\Delta z_k}{2\,\lambda_{i,j,k}} + \frac{\Delta z_k}{2\,\lambda_{i,j,k+1}} + R_{i,j,k+1/2}} \tag{5}$$

where $R_{i,j,k+1/2}$ is the thermal resistance at the interface between the cells. This equation applies for all internal cell surfaces. For the conductance at a boundary condition the equation is modified to Equation 6, shown for heat flow in the x-direction through the area $\Delta y_j \bullet \Delta z_k$:

$$K_{i,j,k+1/2} = \frac{\Delta y_j \Delta z_k}{\frac{\Delta x_i}{2\,\lambda_{i,j,k}} + R_{i,j,k+1/2}} \tag{6}$$

where $R_{i,j,k+1/2}$ is now defined as the boundary surface resistance.

An energy balanced is developed for each computational cell and the net heat flow to cell (i,j,k) from the six adjacent cells is calculated as $H_{i,j,k}$ (W). This net heat flow results in either an increase or decrease in temperature for the cell. The temperature at the new computational time step is calculated as follows in Equation 7:

$$T_{i,j,k,new} = T_{i,j,k} + \frac{\Delta t}{C_{i,j,k}\,\Delta x_i\,\Delta y_j\,\Delta z_k} H_{i,j,k} \tag{7}$$

3.3.2 Thermal Modelling Inputs

Several simplifications were made between the experimental test samples and the models. Due to their minimal effect on longitudinal heat transfer, transverse reinforcing bars were not included in the models. As well, since the program is limited to drawing straight line segments, the circular reinforcing bars were each drawn as a square cross-section with an area equal to that of the original circular cross-section. According to ISO 10211, the surrounding insulating wall was extended a length of 1m above and below the modelled sample.

The interior boundary condition was specified as 21˚C and the exterior boundary condition as -31 ˚C, as per the Winnipeg design temperature. Both boundary conditions were assigned a surface resistance of 0.1 m^2K/W to simulate the low airflow occurring within the plywood shelters of the experimental setup. The boundary conditions were assigned to surfaces as shown in Figure 21. All surfaces in the y-z plane, as well as the uppermost and lowermost rigid insulation wall surfaces in the x-y plane, were assigned the adiabatic boundary condition. Two separate boundary conditions with the same exposure conditions for both the interior and exterior exposure were designated, with boundary conditions two and four assigned as interior and boundary conditions three and five assigned as exterior. The program calculates heat flow through each individual boundary condition, and this assignment allowed for the separation between heat flow

calculated through the balcony surfaces (boundary conditions two and three) and the heat flow calculated through the insulating wall (boundary conditions four and five).

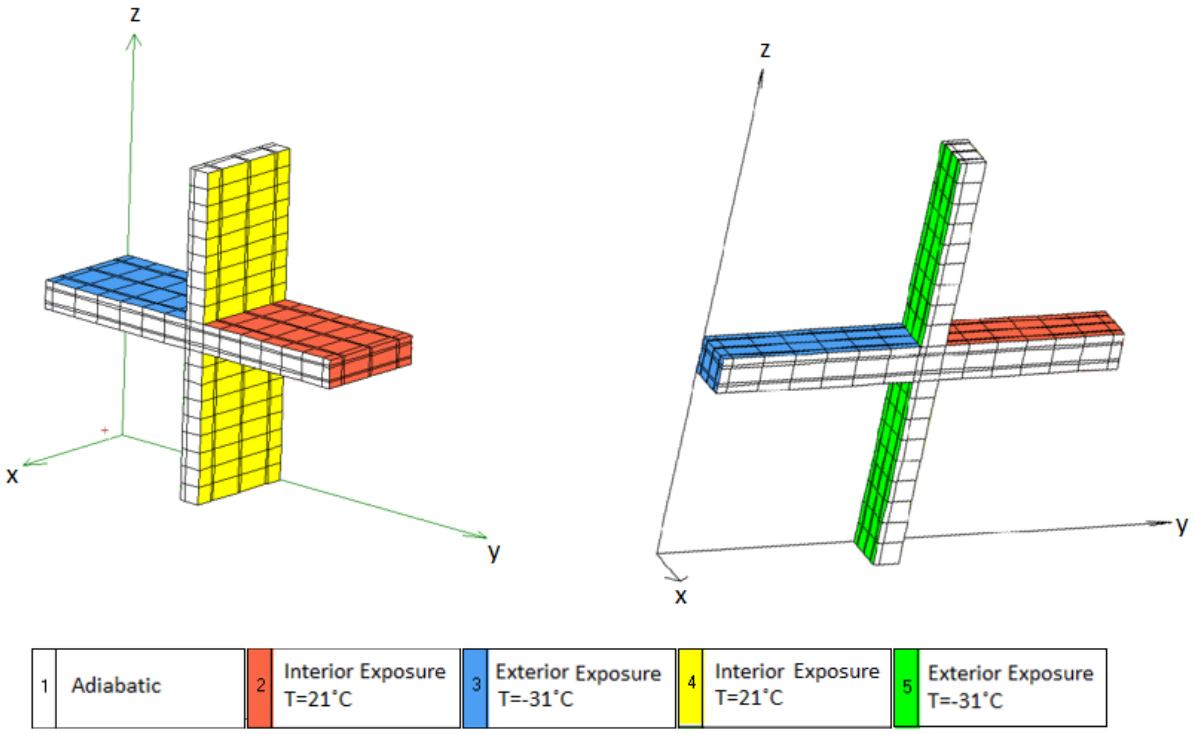

Figure 21 Boundary condition assignments on three-dimensional model

Material thermal conductivities were assigned according to the values found in literature listed in

Table 11. Since the value of thermal conductivity for FRP materials found in literature varies, due to the varying properties of each individual FRP product, a sensitivity analysis was performed by varying the thermal conductivity of GFRP in the model until the sum of differences in temperature between the experimental results and thermal model was minimized and will be included in the experimental results and analysis.

Table 11 Material thermal conductivities used in computer modelling

Material	Thermal Conductivity, λ [W/mK]
Carbon Steel Rebar [8]	50
Stainless Steel Rebar [8]	25
GFRP Rebar	1.5
Armatherm 500 [18]	0.0742
Concrete [8]	2

3.3.3 Numerical Mesh

After inputting physical geometry and material properties, Heat3 produces a numerical mesh, shown in Figure 22.a for the GFRP reinforced sample with a thermal break. A sensitivity analysis was then performed in order to identify an adequately refined numerical mesh. Since the analysis of the temperature profiles from thermal modelling would require interpolation to obtain temperature data at the exact locations of the thermal sensors within the test samples, it was necessary to provide a refined numerical mesh to ensure that error introduced by manual interpolation would be minimized.

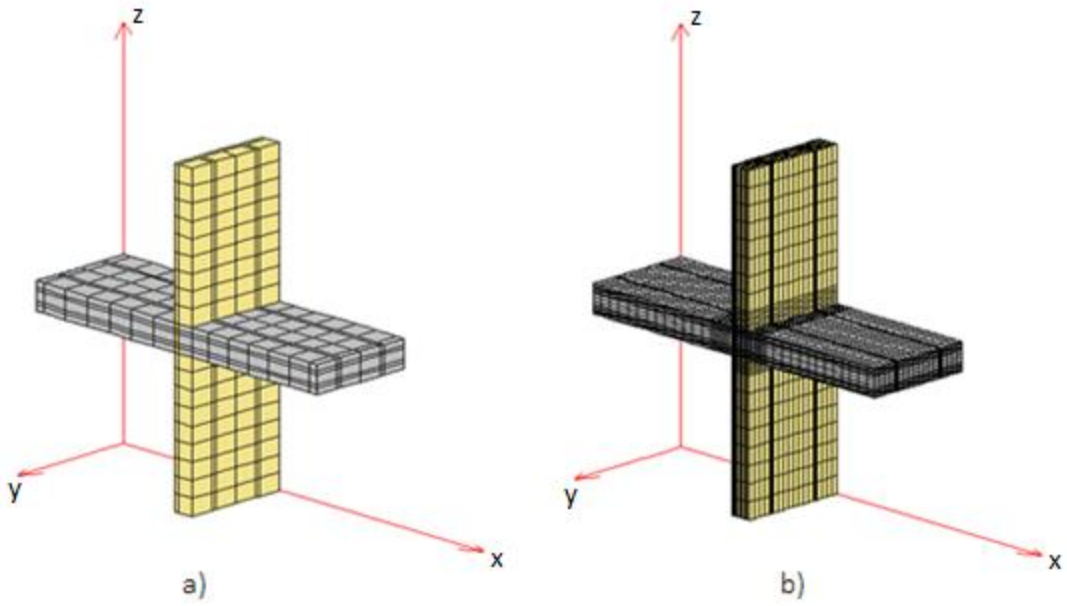

Figure 22 Numerical mesh for GFRP reinforced sample with thermal break a) as derived by the program and b) as selected for analysis

In order to evaluate the sensitivity of the models to the refinement of the numerical mesh, the effect of four numerical mesh densities on the calculated heat flow for each model was observed. Numerical mesh 1 was the coarse numerical mesh as derived by Heat3. For each subsequent numerical mesh, the number of computational cells along each axis was doubled, and therefore the total number of computational cells was increased by a factor of eight. The number of computational cells in each evaluated numerical mesh is provided in Table 12.

Table 12 Number of computational cells in evaluated numerical mesh

Numerical mesh	Number of Computational Cells
1	696
2	5,568
3	44,544
4	365,352

Figure 23 provides the average calculated heat flow through each model when evaluated with each numerical mesh. From this figure it is apparent that the calculated heat flow is generally insensitive to the selected numerical mesh. Between numerical mesh 1 and 2, the calculated heat flow increases by 1.9% on average. Between numerical mesh 2 and 3, the calculated heat flow increased by 1.0% on average. Comparing the heat flow calculated by numerical mesh 3 and 4, the increase is further reduced to 0.2% on average. This indicates that the effect of the selected numerical mesh on the calculated heat flow is decreasing as the fineness of the numerical mesh is increased. Given that the results are changing by 1.0% between numerical mesh 2 and 3, and essentially unchanged between numerical mesh 3 and 4, increasing by only 0.2%, it can be conservatively concluded that the heat flow results are grid independent to within 1.0% at the grid density of numerical mesh 3, and this mesh was selected for performing the analyses.

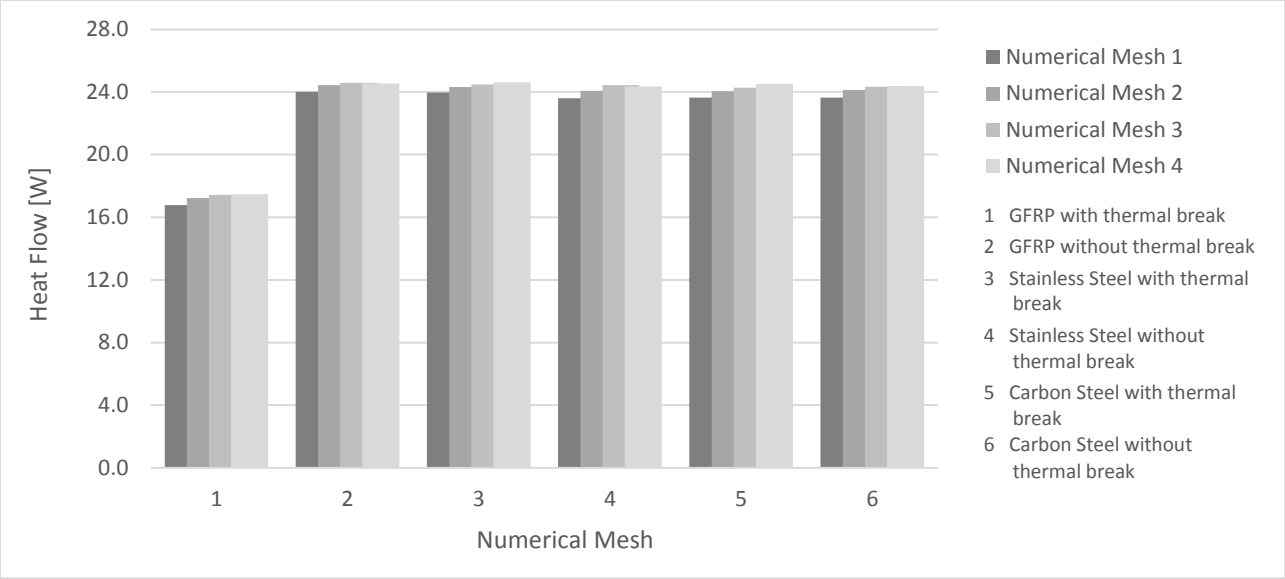

Figure 23 Average heat flow calculated for each model with each variation of numerical mesh

3.4 Structural Testing Program

Structural testing was carried out at the McQuade Structures Laboratory at the University of Manitoba. The samples were destructively tested as cantilevered slabs to simulate the loading of a balcony in service. The configuration of the test setup is shown below in Figure 24. The specimens were supported by two roller supports placed on concrete blocks, labelled as support A and support B.

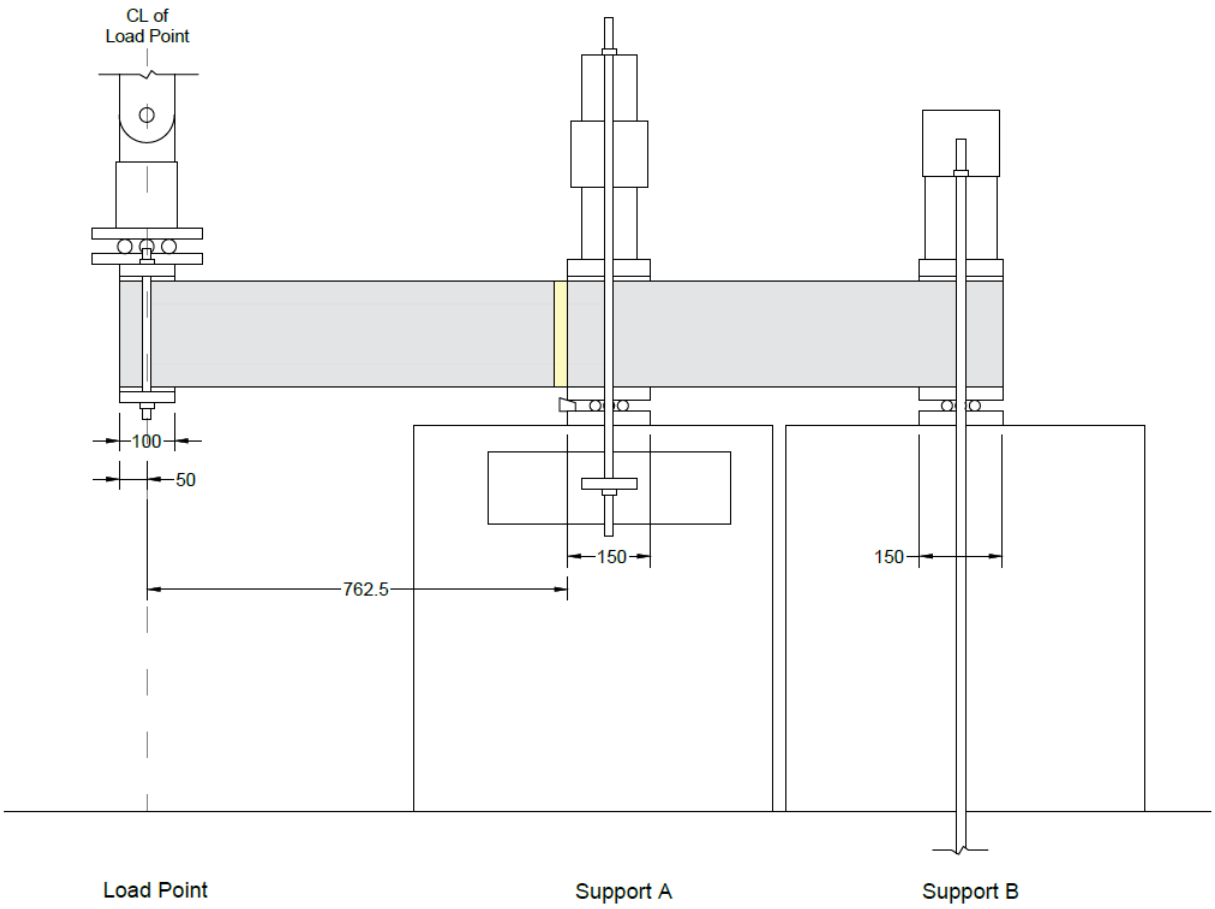

Figure 24 Structural Test Setup

Support B is located at the furthest end from the load point and has a width of 150 mm, as shown in Figure 24. The sample rests on a roller support containing two rollers, which allow horizontal movement with minimal rotation. The purpose of support B is to ensure negative moment development at support A and prevent the samples from overturning during testing, therefore a downwards force is applied to the top surface of the samples, also over a width of 150 mm. This force is applied using two hydraulic jacks, as shown in Figure 25. The hydraulic jacks apply force to a spreader bar, which is in contact with the sample through a steel plate resting on compressible rubber. The compressible rubber, measuring 10 mm in thickness, was placed between the sample and the steel plate to eliminate unevenness on the concrete surface. A steel bar passes through each hydraulic jack and is held in place on top by a bolt, and is then

anchored into the strong floor of the lab, allowing the jacks to push upwards on the bolts and therefore downwards on the spreader bar. The required load was determined by taking the largest anticipated force developed at this support during testing, based on sample strengths, and applying a safety factor of two. This resulted in a load of 100 kN.

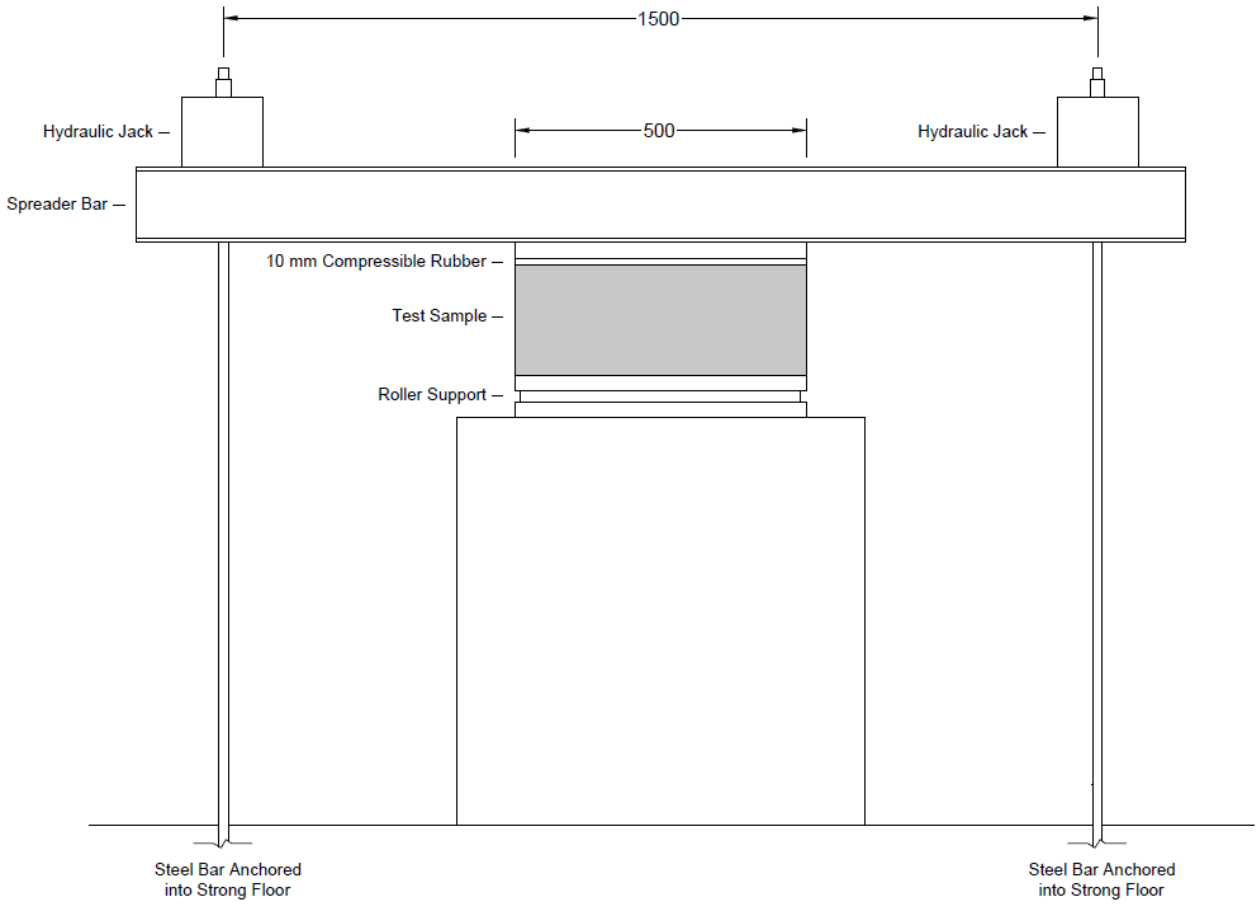

Figure 25 Structural Test Setup - Support B

Support A is located immediately behind the thermal break and has a width of 150 mm, as shown in Figure 24. The sample rests on a roller support containing two rollers and is braced with two additional wooden blocks to prevent rotation towards the load point. The purpose of support A is to simulate the wall system of a building, providing rigidity and preventing rotation. Therefore a downwards force was applied to the top surface of the samples at this support, also through a width of 150 mm. This force was applied by a

hydraulic jack placed between two spreader bars, as shown in Figure 26. The upper spreader bar was anchored downwards at its outer edges into steel supports attached to the lowermost supporting concrete block. The lower spreader bar was in contact with the samples through a steel plate placed on top of a plaster form. The plaster form was used in place of compressible rubber due to the increased unevenness in this area caused by the difficulty in finishing of the concrete around the thermal break and internal thermal sensor wires. The applied load was calculated based on typical wall loads, and a final load of 100 kN was selected, which is equal to the hold down load applied at support B.

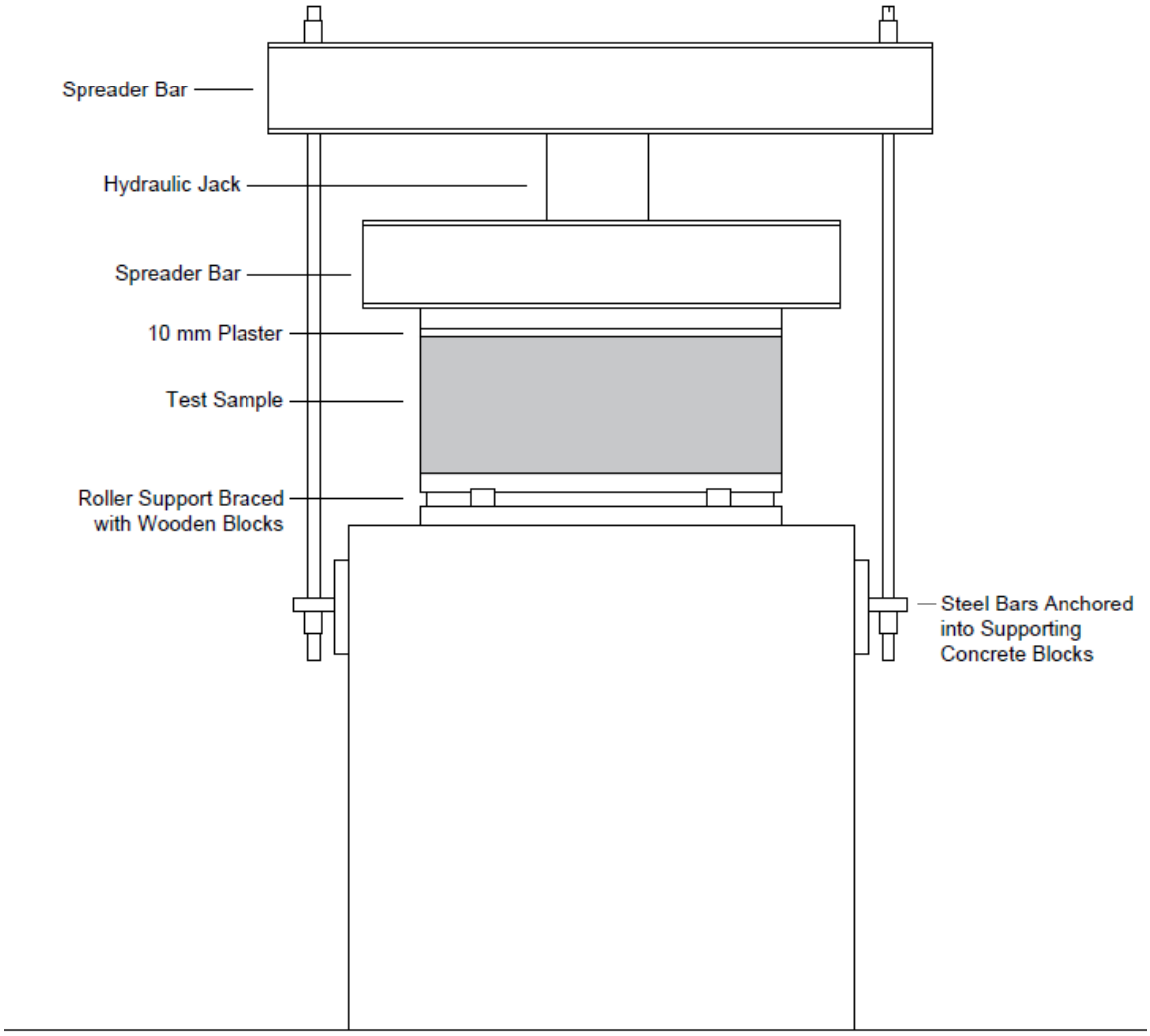

Figure 26 Structural Test Setup - Support A

The samples were loaded at the furthest cantilevered edge from the thermal break, as shown in Figure 24. The centre line of the load was located 50 mm from the edge of the sample, therefore providing a moment arm of 762.5 mm from the point of loading to the thermal break. The load was transferred to the samples through a 100 mm wide plate, placed directly midline to the load point and therefore flush with the edge of the samples. The samples were sandwiched between two steel plates, each with a 10 mm compressible rubber section between them and the sample, which were held in place by steel bars and bolts, as shown in Figure 27. The load from the actuator was transferred first through a rotating pin, which allowed for rotation at the load point as the sample deflected. The load was then transferred through a spreader bar which rested on two sets of rollers, which allowed for extension of the sample as it deflected. The combination of the pin allowing rotation and rollers allowing extension allowed the samples to deflect under the applied load without restricting their movement.

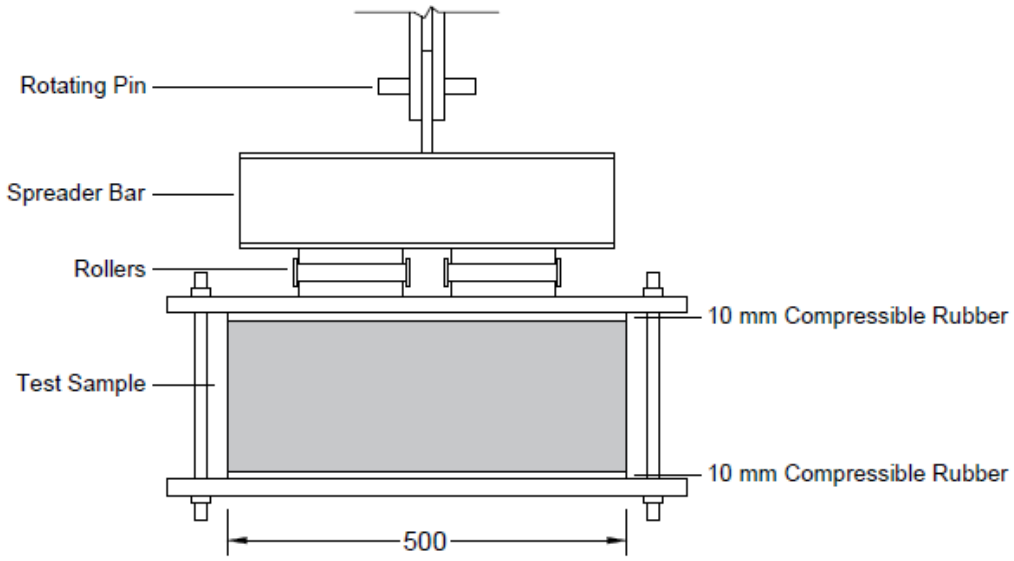

Figure 27 Structural Test Setup - Load Point

3.4.1 Sample Instrumentation for Structural Testing

In order to observe their behaviour during testing, the samples were instrumented with a combination of 350 ohm strain gauges, 200 mm PI gauges, and an LVDT displacement sensor.

Strain gauges were attached to the reinforcing bars within the samples, at the locations shown in Figure 28. For the GFRP reinforced samples there were two strain gauges placed on each of the four reinforcing bars. The first strain gauge, labelled as 1 in Figure 28, was placed halfway across the depth of the thermal break. This was calculated to be the location of highest stress within the rebar during testing. The second strain gauge was placed 25 mm outside of the thermal break, towards the end where the load was applied. The two strain gauges were therefore placed 37.5 mm apart from one another. This allowed for a comparison between the rebar stresses within the thermal break and those immediately outside of it. The two rebars within the top layer were instrumented with strain gauges on their upper surface, and the two rebars within the lower layer on their lower surface. This allowed the strain gauges to capture the highest stress across the cross-section of each rebar. The compression reinforcement was instrumented for the GFRP reinforced samples in order to observe their behaviour, since the behaviour of GFRP in compression is relatively unknown. The steel and stainless steel reinforced samples were instrumented the same way as the GFRP reinforced samples, with the exception that only the tension reinforcement were instrumented. The results from the strain gauges on the tension reinforcement for these samples will be used to determine the yield point during testing.

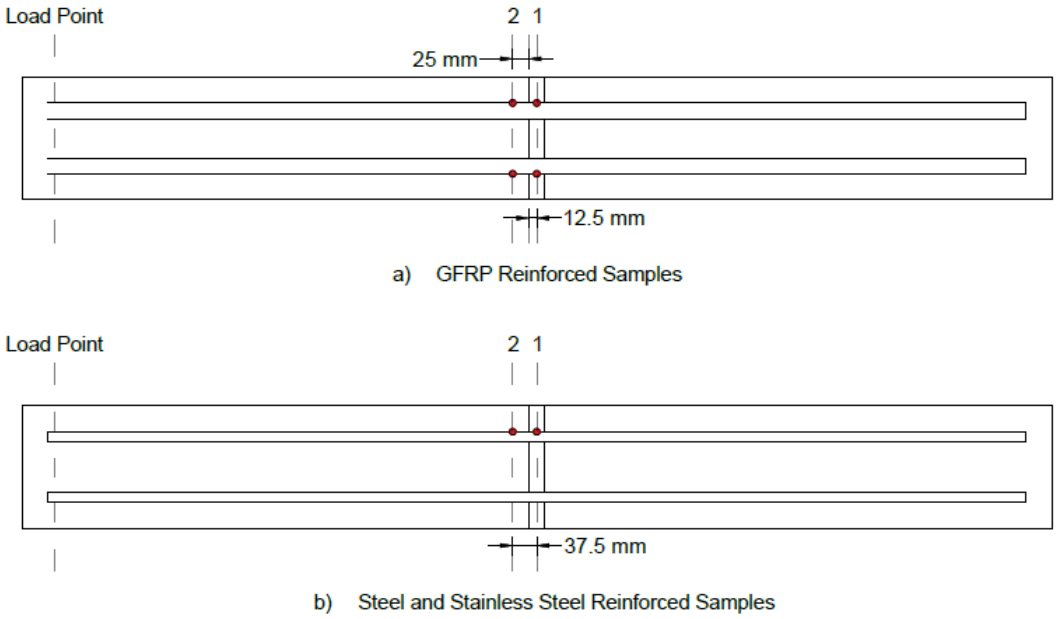

Figure 28 Strain gauge configuration

To install a strain gauge, the surface of the rebar was first sanded to provide a smooth surface and cleaned with rubbing alcohol to remove debris. The gauges were adhered using an industrial adhesive. They were then covered with Teflon tape, followed by epoxy with a sand coating to protect the gauges within the concrete while providing bond.

Four 200 mm PI gauges were installed on each sample to measure the rotation and opening of the thermal break during testing. The configuration of the PI gauges is provided below in Figure 29. To provide a reference, the two exposed longitudinal sides of the samples will be referred to as the East and West edges of the sample. The East edge of the sample was instrumented with two horizontal PI gauges crossing the thermal break. One PI gauge was installed at the uppermost level of the concrete, and the second was installed at the lowermost level, as shown in Figure 29. The west edge was also instrumented with two horizontal PI gauges, placed at the upper and lowermost edges of the sample, however they were placed immediately behind the thermal break as opposed to across it. PI gauges 1 and 2 on the East edge were intended to capture the extension and compression of the sample on the upper and lower most edges

respectively in order to quantify the rotation over the thermal break. Because the PI gauges extended a length of 200 mm, extending 25 mm over the thermal break and 175 mm over concrete, the two additional PI gauges were installed on the West edge. These PI gauges were intended to capture movement due to cracking of the concrete in this location. The intent was to show that there was minimal cracking and therefore minimal movement occurring over PI gauges 3 and 4, therefore the movement occurring over PI gauges 1 and 2 could be used to quantify rotation over the thermal break.

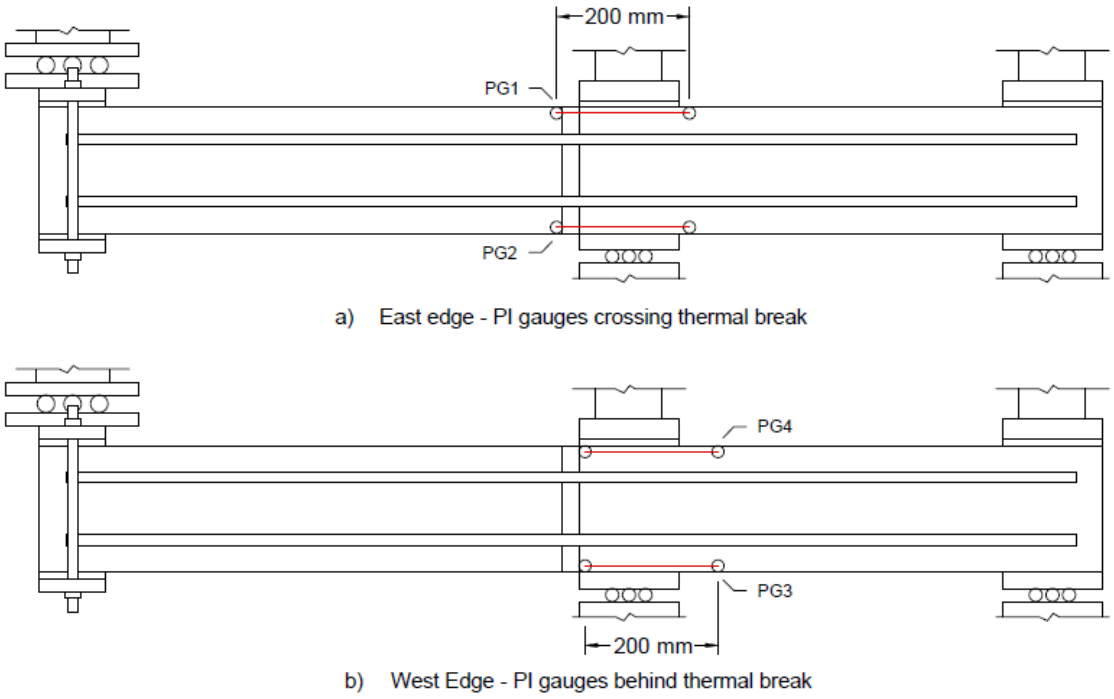

Figure 29 Structural Test Setup - PI gauge configuration

The PI gauges were mounted onto the samples using a combination of bolts and washers. The deflection occurring over a PI gauge was therefore measured from centerline to centerline of its two mounts. The washers directly in contact with the samples measured 18 mm in diameter. Therefore the centerline of the PI gauge mounts were aligned as shown in Figure 30, and are offset by 9 mm from the thermal break.

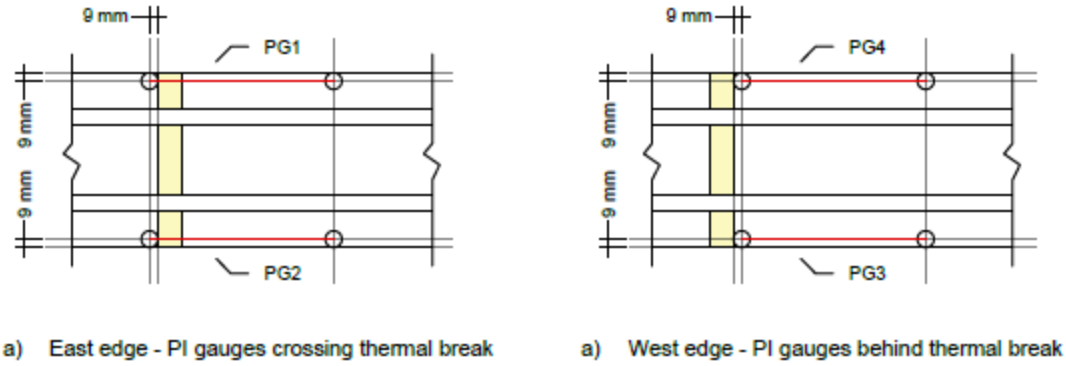

Figure 30 PI gauge mount alignment

One LVDT displacement sensor was placed at the cantilevered end of the samples and installed as shown in Figure 31 in order to record the maximum deflection of the sample. A small steel plate was welded to the structural test setup at mid-width of the samples, in line with the load point, providing a surface onto which the LVDT could be attached.

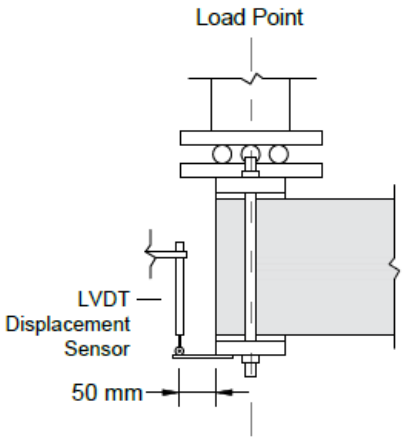

Figure 31 LVDT instrumentation

3.5 Specimen Details and Casting

Preparation and casting of the 18 test samples was done at the University of Manitoba W.R. McQuade Structures Laboratory. Wooden formwork was first built. The alignment of the thermal break was marked

inside of the formwork for all samples. The reinforcement cages, including the thermal break material for the samples that contained it, were first constructed outside of the formwork and lowered into position.

The steel and stainless steel reinforcement cages were tied together using steel ties, whereas the GFRP reinforcement cages were tied using cable ties. This is as it would be done in industry, since it is not desirable to introduce steel ties into GFRP reinforced members since this would introduce the possibility of corrosion. Reinforcing bars were supported by plastic chairs within the forms. The plastic chairs were cut to the required height to ensure accuracy in the depth of the reinforcing bars. Once prepared, the reinforcing cages were lowered into position within the formwork. For samples with the thermal break, the thermal break material was friction fit between the two side walls of the formwork, ensuring that it would not be displaced. For samples without the thermal break, care was taken to align the reinforcement properly when placing in the forms, as well as during casting. Figure 32 shows the formwork for samples containing the thermal break prior to casting.

Figure 32 Formwork prior to casting

To facilitate movement of the samples once cast, lifting hooks were embedded in the concrete. Quarter inch diameter wire rope was used for the lifting hooks. The hooks were installed 400 mm from each end of the sample, as this produced zero bending moment across the thermal break when lifted from the hooks, as shown in the force analysis in Figure 33.

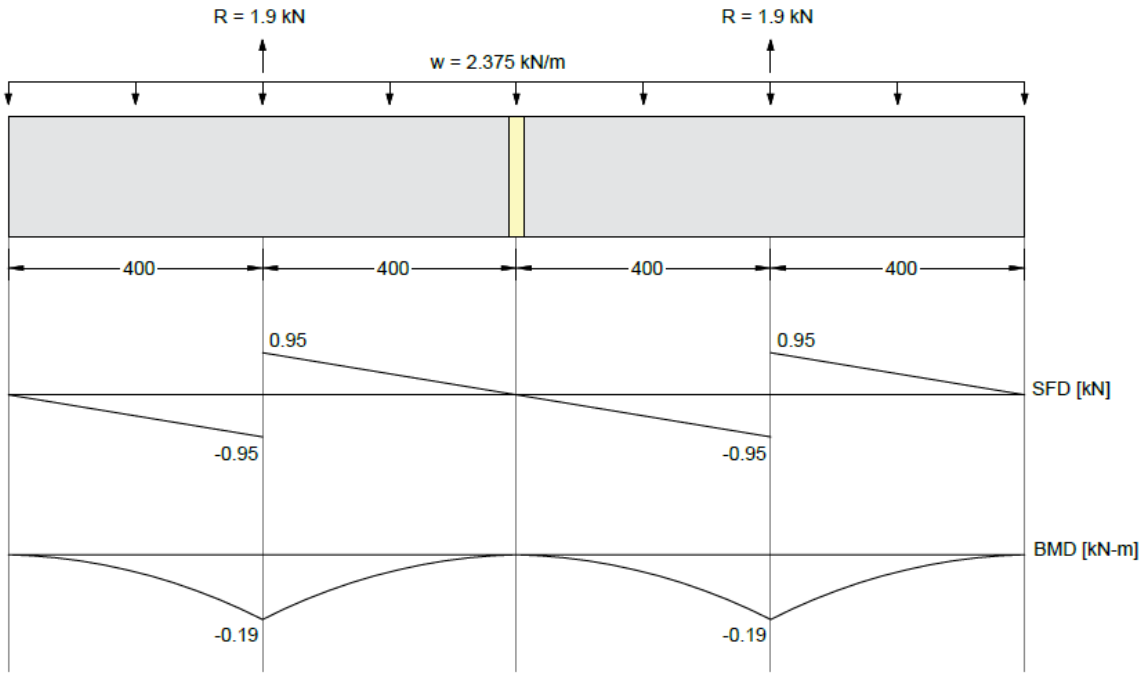

Figure 33 Force analysis for self-weight load induced by lifting hooks

The hooks were attached to the rebar using cable ties, as shown in Figure 34. One three foot section of rope was used for each tie. The ends of the rope were frayed to increase surface area in contact with the concrete in order to provide adequate bond. Once the reinforcement cages were in place with the lifting hooks installed, the thermal sensors were installed at the appropriate locations.

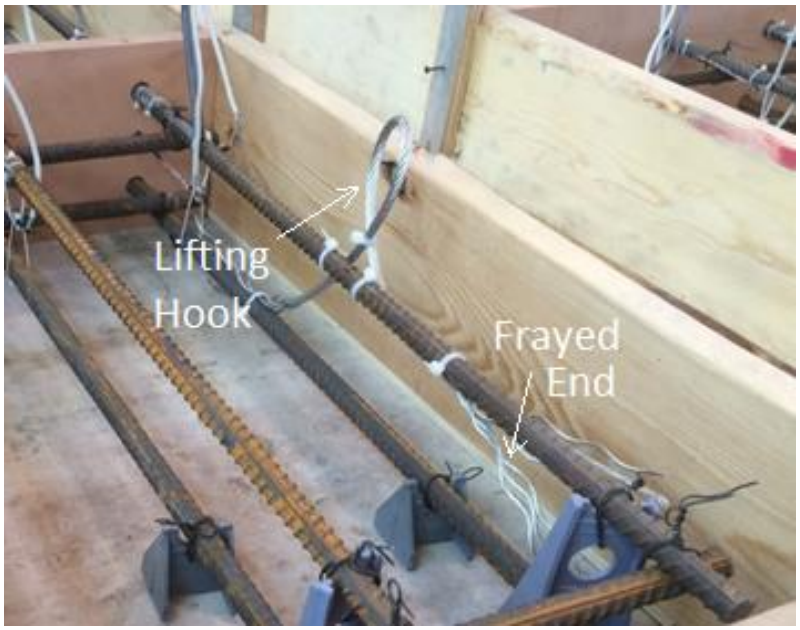

Figure 34 Lifting hook attached to reinforcing bar in formwork

The concrete for the project was donated by Building Products, and the samples were cast from two trucks of concrete over one day. The first casting was performed in the morning and the 9 samples containing the thermal break were cast. The second casting was performed in the afternoon and the remaining 9 samples without the thermal break were cast. Concrete cylinders were also cast for compressive strength testing in order to monitor the concrete strength during curing and testing.

During casting of the concrete, care was taken to avoid damaging the internal sensors. Concrete was either poured or shovelled into the ends of the forms, away from the sensors, and then moved or vibrated to fill the forms. Vibrating was not done within 150 mm of the thermal break in order to avoid damaging the internal sensors. Instead the surrounding area was vibrated thoroughly in order to ensure adequate compaction of the concrete around the sensors. The samples were then moist cured with water soaked burlap covered by plastic tarp to avoid inducing stresses in the concrete due to drying shrinkage.

4 Experimental Results and Analysis

The following section presents the results of thermal and structural experimental testing. The thermal testing results are first presented, and an analysis is performed to compare the experimental results to the numerical results and draw conclusions regarding the system. The structural testing results are then presented, and the failure mode, ultimate load carrying capacity, and deflection of each system are analysed, as well as the performance of GFRP reinforcement in compression. The structural experimental behaviour will be compared to the calculated behaviour presented in Section 3.1.

To identify each individual sample, they are numbered in the order in which they were thermally tested, from sample 1 through 18, as provided in Table 13 below.

Table 13 Test sample numbering scheme

	Sample Numbering Scheme	
Reinforcement	With Thermal Break	Without Thermal Break
GFRP	1,2,3	4,5,6
Carbon Steel	10,11,12	7,8,9
Stainless Steel	13,14,15	16,17,18

4.1 Experimental Thermal Results

The following section will present and evaluate the results obtained from the thermal testing program. The experimental data will first be presented, with the consistency of the results and the direction of heat flow within the test samples evaluated. The experimentally obtained temperature profiles of the samples are presented and discussed. The results from the numerical thermal modelling are then presented, with an analysis to determine the optimal value for the thermal conductivity of GFRP to be used in the models. The numerical results are then used to validate those obtained experimentally, and an analysis is performed using the results from Heat3 to determine the heat flow across the thermal break assemblies.

Prior to examining the steady state temperature data obtained from the thermistors, it is possible to draw preliminary conclusions about the systems from the infrared image provided below in Figure 35. This image shows the temperature gradient across two GFRP reinforced samples, one with a thermal break and one without, taken from the warm chamber. The sample without the thermal break shows significantly colder surface temperatures, shown by the deep purple area immediately adjacent to the insulating wall. Comparatively, the surface temperatures on the sample with the thermal break are significantly higher, demonstrating the effectiveness of the thermal break in isolating the warm and cold sides of the chamber from one another and decreasing the total heat flow through the slab.

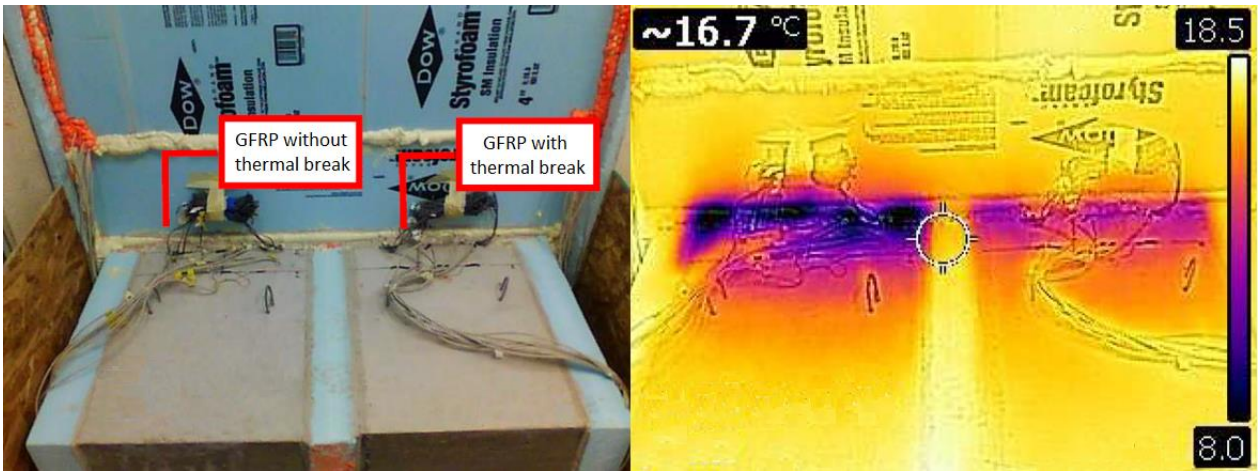

Figure 35 Photograph (left) and infrared image (right) of GFRP reinforced slabs tested in thermal chambers, taken from the warm chamber.

4.1.1 Quality and Consistency of Thermal Experimental Results

Before performing an analysis, the data obtained through experimental thermal testing will first be examined on its own. Data from thermal testing is composed of a temperature profile for each test sample, with the temperatures recorded by thermistors located as shown in Figure 18.

There are a maximum of 66 temperature points in carbon steel reinforced samples and 54 temperature points in stainless steel and GFRP reinforced samples. Several thermistors were damaged, likely during

casting of the concrete due to the aggressive nature of this process, and were therefore not functioning during thermal testing. For the steel reinforced samples, an average of 13% or 9 of the thermistors were damaged in each sample. For the stainless steel reinforced samples, an average of 6% or 3 of the thermistors were damaged. For the GFRP reinforced samples without a thermal break, an average of 4% or 2 of the thermistors were damaged. Due to an error in procedure while performing the experiments, the lead wires to the internal thermistors for samples one and two containing GFRP reinforcement with a thermal break were removed prior to testing. Therefore these two samples were instrumented with only the surface thermistors at level *I*, and only sample number three for the samples containing GFRP reinforcement with a thermal break was instrumented with the full thermistor layout. It is noted that there is a higher number of damaged thermistors in the carbon steel reinforced samples, however there are no obvious explanations for this discrepancy.

To observe the consistency in results between tests, the difference in temperatures recorded at identical locations within two samples of each sample type is compared, with the results summarized below in Table 14. The average temperature difference and standard deviation are provided for each sample type.

Table 14 Average temperature difference and standard deviation of individual temperature points calculated between two samples of the same type

		Average Temperature Difference [˚C]	Standard Deviation [˚C]
GFRP	With Thermal Break	0.9	0.89
	Without Thermal Break	1.3	1.03
Steel	With Thermal Break	0.8	0.85
	Without Thermal Break	1.0	1.01
Stainless Steel	With Thermal Break	0.8	0.62
	Without Thermal Break	0.6	0.48

The low average temperature difference and standard deviation show consistency between the results of different experimental tests on the same sample types and confirm the consistency of the experimental setup. The highest observed average temperature difference for a sample type is equal to 1.3 ± 1.03 ˚C. Including in consideration that the tolerance of the thermal sensors installed was ± 0.2˚C, from the results in the above table it can be concluded that the experimental setup produced consistent results.

4.1.2 Direction of Heat Flow

To observe the general direction of heat flow during thermal testing and to verify our assumption of predominantly longitudinal heat flow, the longitudinal, vertical, and transverse heat flows, Q, at a temperature point were calculated for several test samples using the approximation in Equation 8:

$$Q = -k\,\Delta T/\Delta d \tag{8}$$

where k is the thermal conductivity of the material through which heat flows, ΔT is the change in temperature between two points over which heat flow is calculated, and Δd is the distance between the two points. The temperature point about which the heat flow was calculated is located in cross-section C, row 2 and level II as labelled in Figure 18, and as indicated in Figure 36.

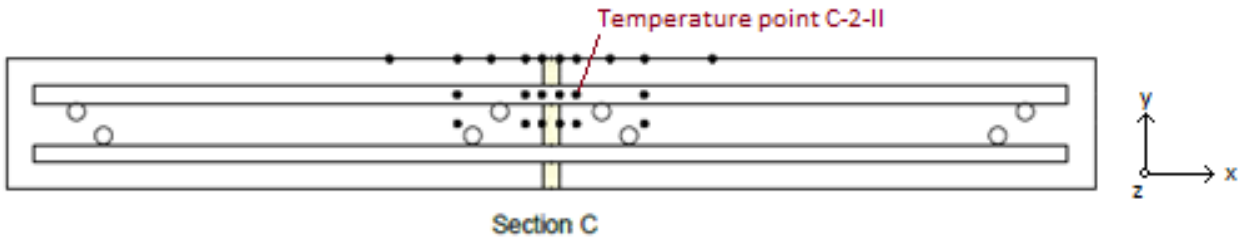

Figure 36 Temperature point selected for calculation of directional heat flows, located in cross-section C

As provided in Figure 37, the longitudinal heat flow is labelled as the x-direction, the vertical heat flow as the y-direction, and transverse heat flow as the z-direction. Temperature point C-2-II was selected as it is

surrounded by concrete in all directions, therefore the calculation of heat flow to each adjacent temperature point can be calculated using the thermal conductivity of concrete equal to 2 W/mK.

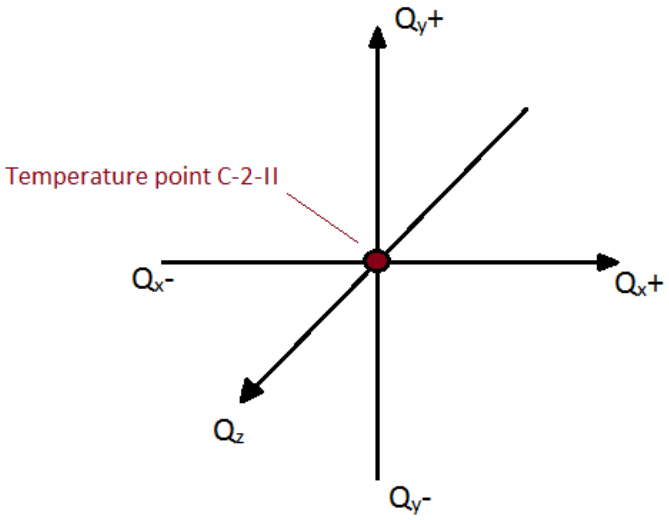

Figure 37 Heat flow labelling for direction of heat flow analysis

A summary of the obtained heat flows is presented in Table 15. Negative values indicate that the direction of flow is opposite of what is shown in Figure 37.

Table 15 Heat flow values calculated at discrete locations within test samples

	GFRP		Steel		Stainless Steel	
	Thermal Break	No Thermal Break	Thermal Break	No Thermal Break	Thermal Break	No Thermal Break
Sample Number	3	6	12	9	14	18
Q_x+	107.3	211.3	-	197.2	138.3	194.4
Q_x-	180.1	284.0	374.3	433.7	368.9	274.7
Q_y+	32.5	34.0	77.3	24.8	60.5	9.0
Q_y-	161.4	19.8	30.7	69.7	27.4	4.2
Q_z	10.9	7.7	35.5	9.8	1.3	4.4

As shown in Table 15, the longitudinal heat fluxes, Q_x+ and Q_x-, have significantly higher magnitudes than the vertical, Q_y+ and Q_y-, and transverse, Q_z, heat fluxes. This is with the exception of sample number 3, containing GFRP reinforcement with a thermal break, in which the upwards vertical heat flux is of

equivalent magnitude. Given that the five remaining sample types confirm the predominantly longitudinal heat flow within the system it can be confirmed that our assumption was correct. On average, longitudinal heat flow values are 4.9 times larger than vertical and 39.9 times larger than transverse. The significantly low transverse heat flow confirms that the provided plywood shelter within the thermal testing chambers effectively eliminated the transverse temperature gradient observed in the mock-up samples.

4.1.3 Experimental Temperature Profiles

The following section will present graphically the longitudinal temperature profiles observed from one of each sample type and will discuss the data. As the results between test samples are consistent, with an average standard deviation of 0.8˚C amongst all temperature profiles, one example from each type of sample (each type of reinforcement both with and without a thermal break) will be presented below for discussion. Blue data points on the following figures indicate negative temperatures whereas red data points indicative positive temperatures. A yellow shaded rectangle indicates the location of the thermal break for samples containing the break, whereas a blank rectangle indicates a sample without a thermal break and is in place to indicate the alignment of the break for the purpose of drawing comparisons, however it is in actuality continuous concrete for these samples.

Figure 38 provides the experimentally obtained cross-sectional temperature profiles for the GFRP reinforced samples both with and without a thermal break. Of immediate notice is the separation of positive and negative temperatures to either side of the thermal break in Figure 38a. This indicates the effectiveness of the thermal break in shifting and increasing the temperature gradient across the thermal break, reducing the penetration of cold temperatures to the interior of the building. Comparatively in Figure 38b, without the thermal break, temperatures as low as -7.7˚C are found to the interior of the break. By introducing the thermal break the system is now able to better isolate the two environments and prevent the colder temperatures from penetrating the warm side of the slab.

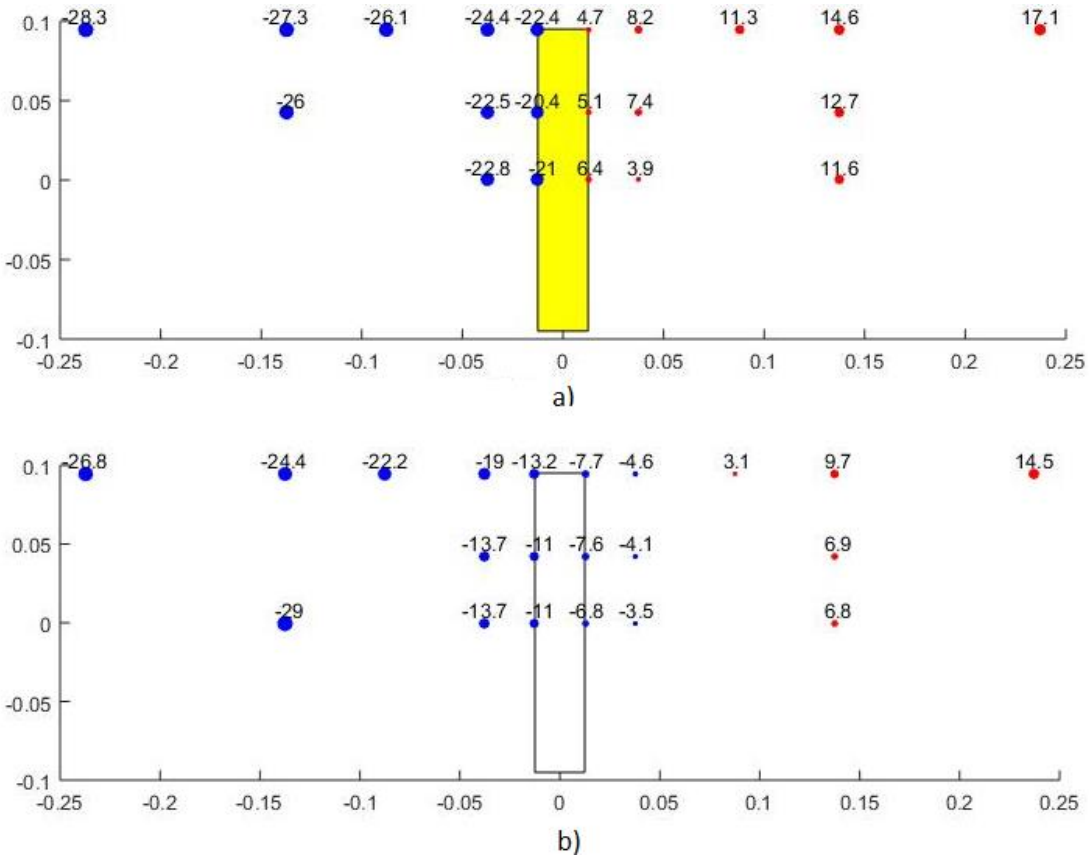

Figure 38 Experimentally obtained temperature profiles for a GFRP reinforced test sample a) with thermal break and b) without thermal break, all temperatures in ˚C

Figure 39 presents the longitudinal temperature profiles for samples reinforced with regular carbon steel. Figure 39b, containing carbon steel reinforcement without a thermal break, may be considered as the base case of a regularly reinforced balcony without any thermal break remediation. As was observed with the GFRP reinforced samples, the thermal break effectively separates the negative temperatures to the cold side and the positive temperatures to the warm side. However due to the increased thermal conductivity of the carbon steel in comparison to that of GFRP, the improvement is not as significant. When comparing Figure 38a for a sample containing GFRP with a thermal break and Figure 39a for a sample containing steel with a thermal break, temperatures on average 55% lower are found adjacent to the thermal break on the warm side for the steel reinforced sample compared to the GFRP reinforced sample. This indicates that the benefit introduced by the thermal break is optimised when used in combination with reinforcing materials

that also possess a lower thermal conductivity. Despite the increase in reinforcement surface area due to using larger diameter rebar for GFRP than carbon steel, the GFRP reinforced section still provides better performance with regards to reducing the penetration of cold temperatures to the interior.

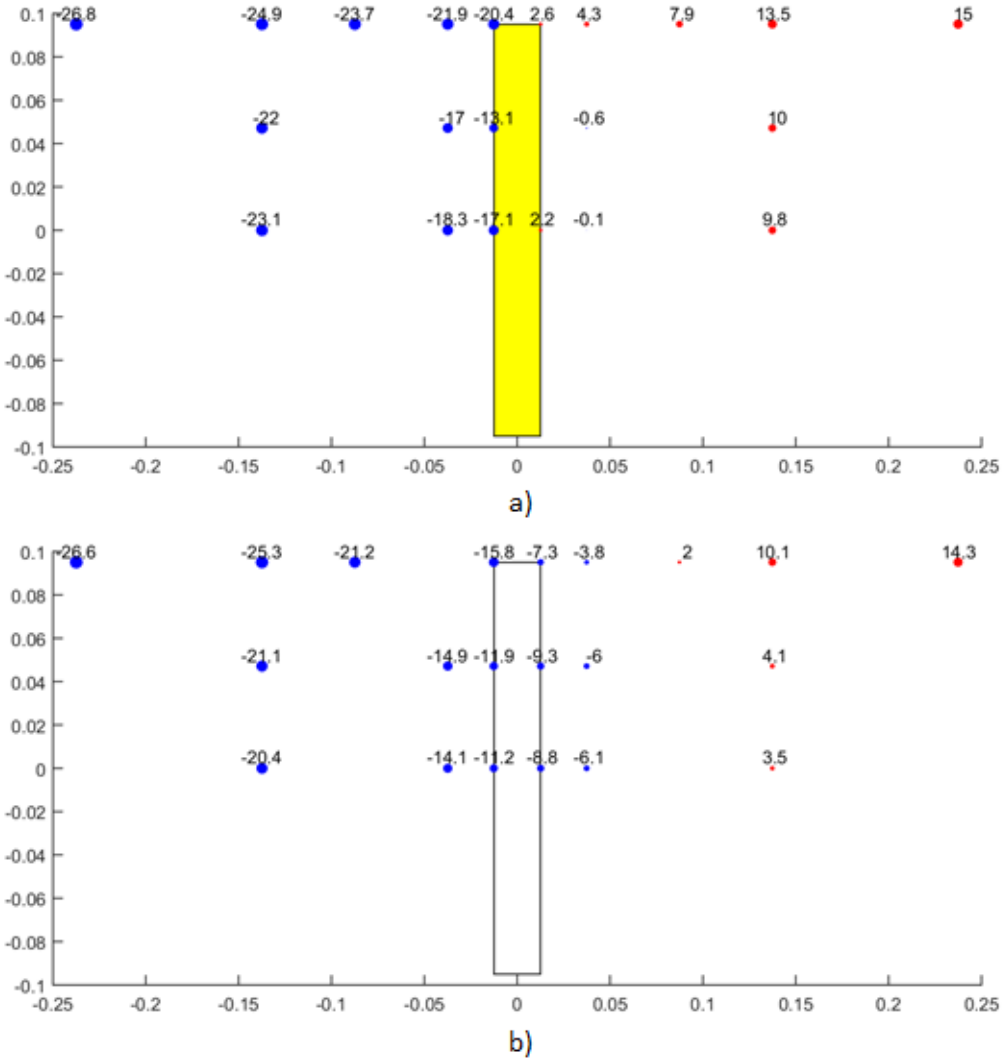

Figure 39 Experimentally obtained temperature profiles for a carbon steel reinforced test sample a) with thermal break and b) without thermal break, all temperatures in ˚C

Figure 40 presents the longitudinal temperature profiles for samples reinforced with stainless steel. As seen with the two other types of reinforcement, the thermal break effectively separates the negative temperatures to the cold side and the positive temperatures to the warm side. Since the thermal

conductivity of stainless steel is lower than that of carbon steel, the stainless steel reinforced section performs better than the carbon steel reinforced section in terms of reducing the penetration of colder temperatures to the warm side of the sample. The temperatures immediately adjacent to the thermal break on the warm side for the stainless steel reinforced sample are on average 147% higher than those found in the carbon steel reinforced sample with a thermal break. When comparing the temperatures immediately adjacent to the thermal break for both the GFRP reinforced and stainless steel reinforced samples, there is very little variance. At the top surface of the samples the temperature of the GFRP reinforced sample is 1.1˚C colder than that of the stainless steel reinforced sample, however at mid-height the GFRP reinforced sample is 0.4˚C warmer than the stainless steel reinforced sample. This indicates that the two systems perform similarly in terms of reducing the penetration of cold temperatures to the interior of the building. Further analysis in terms of heat flow and thermal modelling can be used to determine the overall performance of the systems relative to one another.

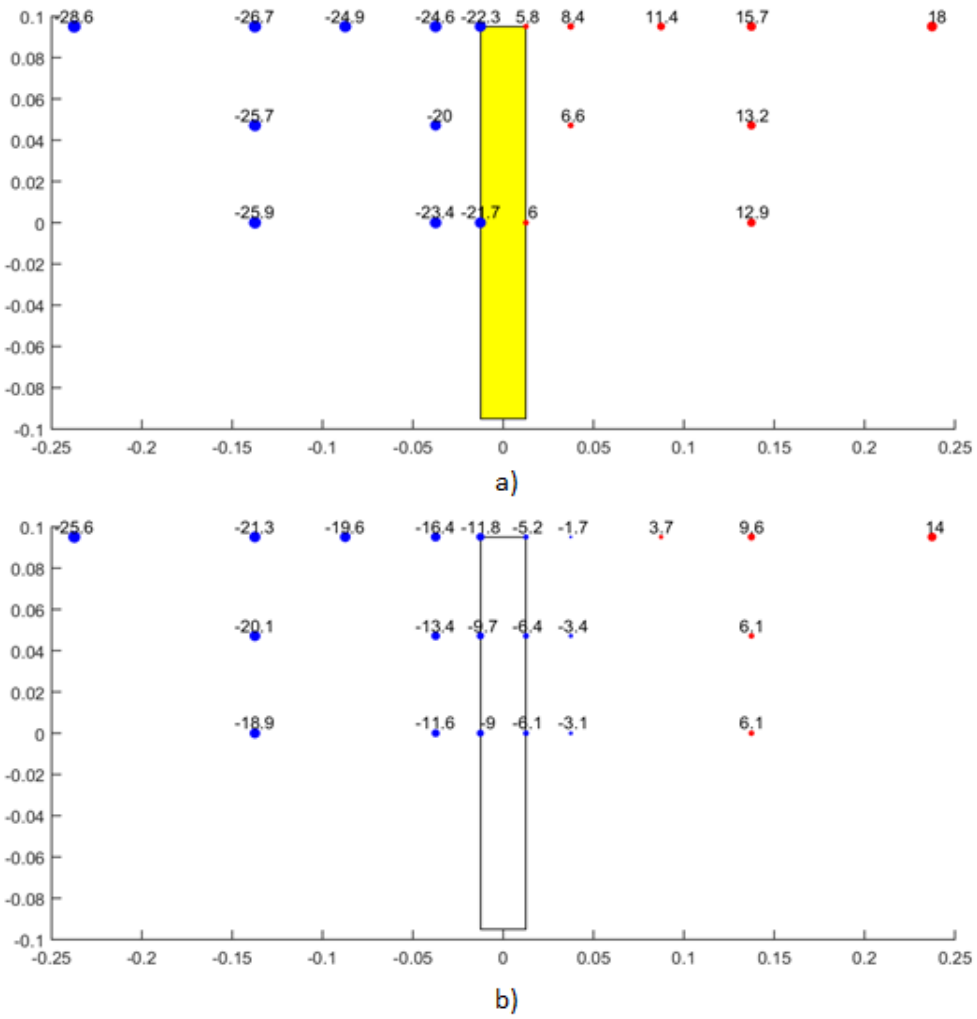

Figure 40 Experimentally obtained temperature profiles for a stainless steel reinforced test sample a) with thermal break and b) without thermal break, all temperatures in ˚C

The initial assessment of the temperature data obtained from thermal testing demonstrates the effectiveness of the thermal break in separating the two thermal environments. When compared to the base case of regular carbon steel reinforcement without a thermal break, the optimized system containing GFRP reinforcement with a thermal break increases the temperatures adjacent to the thermal break on the warm side by an average of 13.7˚C. To further quantify the performance and properties of the systems, thermal modelling will be employed in the following sections.

4.2 Thermal Modelling

As presented in section 3.3, thermal modelling was performed using Heat3 to verify the temperature profiles obtained through experimental testing, and to draw further conclusions regarding the systems and their thermal insulating properties. The general inputs and numerical mesh for thermal modelling were presented previously in section 3.3. The following sections will first provide the approach to determining the value for the thermal conductivity of GFRP to be used in thermal modelling. An analysis comparing the temperature profiles obtained through modelling and those obtained experimentally will follow, and the results from the models will be used to draw conclusions on the thermal performance of the systems.

4.2.1 Thermal Conductivity of GFRP

To model the cast in place balcony thermal breaks in Heat3D the thermal conductivity of each material was required. Unlike steel and stainless steel, different GFRP products are each composed of a different combination of polymers and fibers, and therefore have different thermal conductivities. For the GFRP product selected for testing, there is no available literature or manufacturer data provided regarding its thermal conductivity. As discussed in section 2.3.1 there are values for thermal conductivity found within literature for other GFRP products. Based on these values, an analysis was performed within Heat3D to determine the thermal conductivity of GFRP that would best reproduce the experimental results.

To determine the optimal thermal conductivity of GFRP, the system was modelled with a range of values and that which minimized the difference between the model results and experimental results was selected for all further analyses. The values selected range from 0.1 W/mK to 3.5 W/mk, based on data available in literature. A summary of the average and maximum temperature difference calculated over this ranges of thermal conductivity values is provided in Figure 41 and Figure 42, respectively.

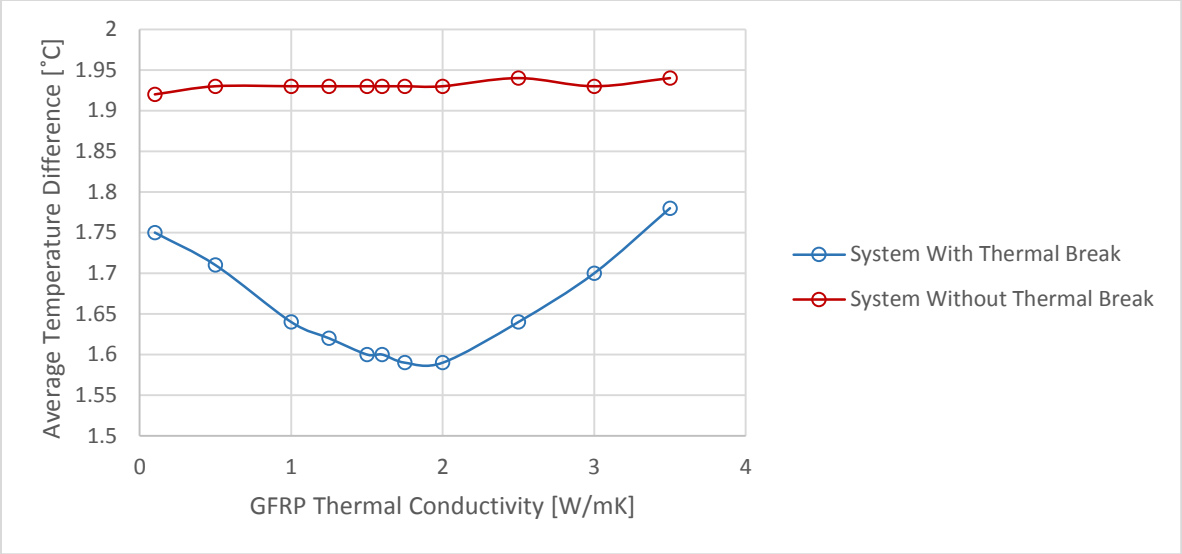

Figure 41 Average temperature difference calculated between experimental and numerical results for a range of GFRP thermal conductivities

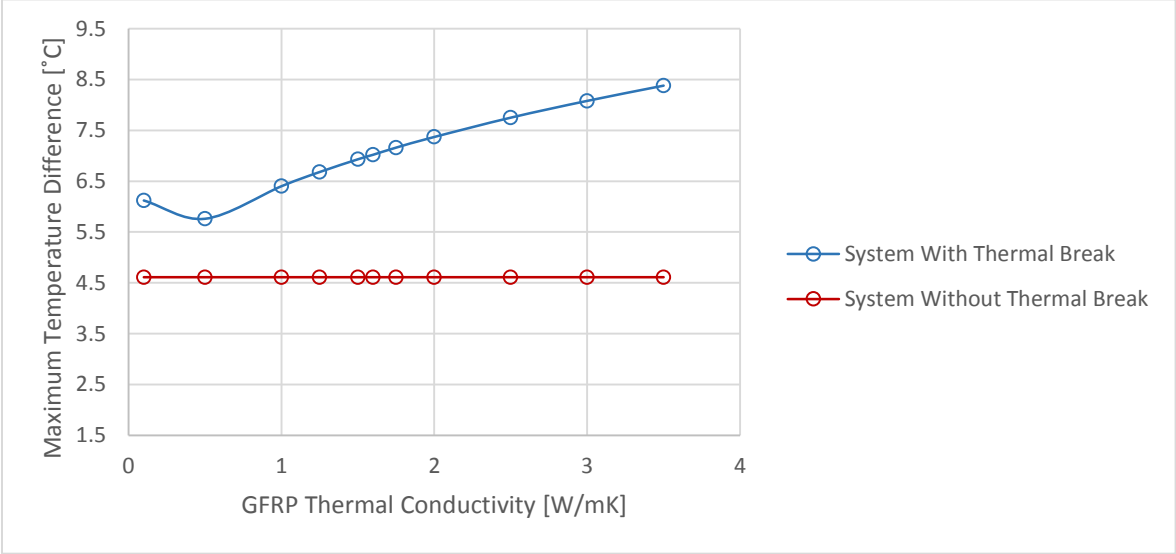

Figure 42 Maximum temperature difference calculated between experimental and numerical results for a range of GFRP thermal conductivities

For the samples containing a thermal break, the average temperature difference continues decreasing as the value for λ decreases towards 1.75 W/mK, and begins increasing as λ continues decreasing past 1.6 W/mK. The lowest maximum difference is observed when λ is equal to 1.5 W/mK. The total sum of differences when λ is equal to 1.5 W/mK is only 0.9˚C, or 1.3% higher than that when λ is equal to 1.6

W/mK. Based on these observations, a value of 1.5 w/mK for the thermal conductivity of GFRP provides an optimized representation of the experimental results.

For the samples without a thermal break there is very little difference observed within the obtained temperature profile of the model when the thermal conductivity of GFRP is varied. For each variation, a maximum local temperature difference of 4.61˚C is observed. The average decreases as λ decreases, but only by 1% over the range of values observed.

For the samples containing the thermal break the GFRP reinforcement is the main conduit for heat to flow across the thermal break, therefore it is anticipated that varying the thermal conductivity of the material would produce more significant of an effect than for the model without a thermal break. The thermal conductivity of concrete is larger than that of the GFRP, therefore for the samples without a thermal break the temperature distribution in the balcony is insensitive to the thermal conductivity of GFRP. Therefore, the results observed for samples containing the thermal break provide a better analysis for the effect of varying the thermal conductivity of GFRP. Based on the above observations, a thermal conductivity of λ=1.5 W/mK was selected for further analyses.

4.2.2 Comparison between Model and Experimental Results

To use the results from the models developed in Heat3D to draw conclusions regarding the balcony thermal breaks developed in this project, we must first compare results from the two methods to ensure that they agree within reasonable error. To do so, interpolation is performed on the temperature profiles obtained from Heat3D to obtain temperature values at the same coordinates as those recorded experimentally. This allows for a direct comparison between the two temperature profiles. Results from each test sample are compared to those from modelling by observing the absolute temperature difference at each point of sampling. Provided in the following section is a summary of the average and maximum temperature differences observed within each sample and a discussion regarding the analysis.

Table 16 presents the calculated average and maximum temperature differences observed between each experimental sample and the model for all GFRP reinforced samples. The average temperature difference ranges from 0.8 – 1.9˚C. The average temperature difference for samples containing GFRP without a thermal break is equal to 1.3˚C, while that for samples with a thermal break is equal to 1.37 ˚C. The average maximum temperature difference for samples containing GFRP without a thermal break is equal to 3.8 ˚C while that for samples with a thermal break is equal to 5.4˚C. In general, given the low average local temperature differences of 1.30˚C and 1.37˚C for samples without and with a thermal break, respectively, it can be concluded that the model provides an adequate representation of the systems and may be used to further analyse the systems containing GFRP reinforcement. Although local discrepancies are present, as shown by the increased maximum local temperature differences, the behaviour of the system as a whole is represented well by the model. These local discrepancies may also be accounted for by experimental error, such as exact placement of the thermal sensors during construction and casting of the concrete.

Table 16 Comparison between experimental and modelled temperature profiles for GFRP reinforced samples

GFRP Reinforced Samples						
	Without Thermal Break			With Thermal Break		
Test Sample	4	5	6	1	2	3
Average Temperature Difference [˚C]	0.8	1.2	1.9	1.6	0.9	1.6
Maximum Temperature Difference [˚C]	2.8	4.1	4.6	5.2	4.2	6.9

Table 17 presents the calculated average and maximum temperature differences observed between each experimental sample and the model for all steel reinforced samples. The average temperature difference ranges from 1.2 – 2.1˚C. The average for samples containing steel reinforcement without a thermal break is equal to 1.2˚C, while that for samples with a thermal break is equal to 1.8. The average maximum temperature difference for samples containing steel reinforcement without a thermal break is equal to 3.7˚C while that for samples with a thermal break is equal to 6˚C. For steel reinforced samples, the system

without a thermal break is slightly more accurately represented, with an absolute average local temperature difference of 1.2˚C, in comparison to that found for the samples with a thermal break equal to 1.8˚C. The local discrepancies are again present, as shown by the increased local maximum temperature differences.

Table 17 Comparison between experimental and modelled temperature profiles for carbon steel reinforced samples

Carbon Steel Reinforced Samples						
	Without Thermal Break			With Thermal Break		
Test Sample	7	8	9	10	11	12
Average Temperature Difference [˚C]	1.2	1.3	1.2	1.2	2.1	2
Maximum Temperature Difference [˚C]	4.9	3.6	2.5	3.5	7.8	6.7

Table 18 presents the calculated average and maximum temperature differences observed between each experimental sample and the model for all stainless steel reinforced samples. The average temperature difference ranges from 1.2 – 2˚C. The ultimate average for samples containing stainless steel reinforcement without a thermal break is equal to 1.27˚C, while that for samples with a thermal break is equal to 1.83. The average maximum temperature difference for samples containing steel reinforcement without a thermal break is equal to 3.7˚C while that for samples with a thermal break is equal to 5.37˚C. As was observed for the steel reinforced samples, the system without a thermal break is slightly more accurately represented, with an absolute average local temperature difference of 1.27˚C, in comparison that that found for the samples with a thermal break equal to 1.83˚C. Local discrepancies are again present, as shown by the increased local maximum temperature differences.

Table 18 Comparison between experimental and modelled temperature profiles for stainless steel reinforced samples

Stainless Steel Reinforced Samples						
	Without Thermal Break			With Thermal Break		
Test Sample	16	17	18	13	14	15
Average Temperature Difference [˚C]	1.2	1.4	1.2	1.9	1.6	2
Maximum Temperature Difference [˚C]	4.9	3.6	2.5	5.3	5.4	5.4

The systems modelled without a thermal break provide a marginally better representation than the systems modelled with a thermal break, showing an average temperature difference across all sample types of 1.27˚C and 1.66˚C for samples with and without the thermal break, respectively. Local temperature discrepancies are present within all sample types. These may however be accounted for by experimental error, such as the exact placement of the thermal sensors within the concrete during casting, and therefore do not discredit the performance of the model in representing the experimental conditions. For samples containing each type of reinforcement the model developed in Heat3D provides a sufficiently accurate representation of the temperature profile observed under the experimental conditions, as determined by the low average local temperature difference, and can therefore be used for further analysis of the systems.

4.2.3 Heat Flow across Thermal Breaks

The following section will present the results from the models developed in Heat3 pertaining to the heat flow through each modelled system. These results will be used to draw conclusions on the reduction in heat flow across the cast in place balcony slab introduced by the thermal break.

Boundary condition assignments are detailed in Section 3.3.2. The following section will analyze the heat flow through the thermal break assembly using the heat flow calculated through boundary conditions two and three representing the exposed concrete surfaces in the assembly for the interior and exterior surfaces, respectively.

As shown in the following results, the heat flows calculated through boundary conditions two and three for samples without a thermal break are equal in magnitude and opposite in direction. For samples containing a thermal break, the heat flow through boundary condition two is on average 7% larger than that calculated through boundary condition 3. This indicates that the thermal break is providing enough resistance to direct a portion of the total heat flow into the reinforced concrete slab from the cold side either upwards or downwards through the surrounding insulating wall. Given that the insulating wall is composed of a plain

insulating block and does not represent the construction of a typical wall system in which a balcony would be installed, the heat flow through this portion of the model is not used to represent the heat flow through the balcony thermal break system.

Table 19 provides the calculated heat flows for GFRP reinforced samples both with and without a thermal break. Without a thermal break, the average heat flow through the system is equal to 24.60 W. With the introduction of the thermal break, the average heat flow is reduced to 10.82 W, providing a 56.1% reduction is heat loss through the balcony system.

Table 19 Heat flows through samples containing GFRP reinforcement as calculated by Heat3

Surface	Without Thermal Break [W]	With Thermal Break [W]	Percent Reduction [%]
Interior Exposure	24.60	11.45	53.5
Exterior Exposure	-24.60	-10.18	58.6
Absolute Value Average	24.60	10.82	56.1

Table 20 provides the calculated heat flows for steel reinforced samples both with and without a thermal break. Without a thermal break, the average heat flow through the system is equal to 28.87 W. With the introduction of the thermal break, the average heat flow is reduced to 20.06 W. This only provides a 30.5% reduction in heat loss through the balcony system, which is significantly lower than the percent reduction observed for the GFRP reinforced samples. The average heat flow through the system containing steel reinforcement with a thermal break is also only 18% lower than that calculated for the GFRP reinforced system without a thermal break.

Table 20 Heat flows through samples containing carbon steel reinforcement as calculated by Heat3

Surface	Without Thermal Break [W]	With Thermal Break [W]	Percent Reduction [%]
Interior Exposure	28.87	20.40	29.3
Exterior Exposure	-28.87	-19.72	31.7
Absolute Value Average	28.87	20.06	30.5

Table 21 provides the calculated heat flows for stainless steel reinforced samples both with and without a thermal break. Without a thermal break, the average heat flow through the system is equal to 26.09 W. With the introduction of the thermal break, the average heat flow is reduced to 14.44W, providing a percent reduction of 44.7%.

Table 21 Heat flows through samples containing stainless steel reinforcement as calculated by Heat3D

Surface	Without Thermal Break [W]	With Thermal Break [W]	Percent Reduction [%]
Interior Exposure	26.09	14.94	42.8
Exterior Exposure	-26.09	-13.93	46.6
Absolute Value Average	26.09	14.44	44.7

A further comparison may be made between the conventional method of constructing a balcony and the three variations of thermal breaks. The conventional balcony is represented in this experimental program by the steel reinforced samples without a thermal break and is compared in Table 22 to the samples containing a thermal break reinforced with each carbon steel, stainless steel, and GFRP. The largest percent reduction in heat flow when compared to the conventional balcony is observed for the GFRP reinforced thermal break, equal to 62.5%, which is more than twice the percent reduction observed for carbon steel reinforced samples, equal to 30.5%. Stainless steel reinforced samples also provide a significant improvement, providing a 50% reduction in heat flow through the system.

Table 22 Comparison between heat flows through a conventional balcony system and the thermal break variations

Surface	Average Heat Flow [W]	Percent Reduction [%]
Continuous Balcony with Carbon Steel Reinforcement	28.87	-
Steel Reinforced Thermal Break	20.06	30.5
Stainless Steel Reinforced Thermal Break	14.44	50.0
GFRP Reinforced Thermal Break	10.82	62.5

In general, the introduction of the thermal break provides a significant reduction in total heat flow through the balcony system. The most significant improvement is observed for the GFRP reinforced samples,

indicating that the thermal performance of the cast in place balcony thermal break is optimized when used in conjunction with reinforcement with a low thermal conductivity. Stainless steel reinforcement also provides a significant reduction, reducing the total heat loss through the system by 50%. Therefore, a thermal break reinforced with either stainless steel or GFRP reinforcement will provide a significant reduction in the total heat loss of a building's envelope. These provide a promising solution for building greener buildings with lower environmental footprints. Based on the results of this thermal analysis, GFRP reinforcement is recommended as the preferred reinforcement for balcony thermal break systems.

4.3 Structural Testing Results

The following section presents and analyzes the data obtained through experimental structural testing. First, a general overview of the data obtained from the strain gauges, PI gauges, and LVDT sensors is presented. The compressive performance of GFRP in a thermal break is reviewed based on the data obtained from strain gauges. The ultimate failure and yield loads of the test samples is then discussed and compared with the calculated design values presented in section 3.1.8, followed by a discussion regarding the failure modes and physical performance of the samples. Lastly, serviceability performance including deflection of the samples is discussed.

Due to an error in the data acquisition system used for structural testing, the data sets obtained from two samples are disregarded. These samples are sample number four containing GFRP reinforcement without a thermal break and sample number 13 containing stainless steel reinforcement with a thermal break. The error was due to the data acquisition system scaling the recorded data using an unknown and incorrect reference, therefore it is not possible to process the data to have it scaled to the appropriate reference. The remaining two samples for each sample type in which one was lost produced consistent results, therefore these will be used to draw conclusions regarding the system.

4.3.1 Structural Experimental Data

The data obtained from structural experimental testing is composed of data from the reinforcement mounted strain gauges, surface mounted pi gauges, and the LVDT installed on each test sample. The following subsections will present and discuss data from representative samples for each type of sensor.

4.3.1.1 Strain Gauge Data

The strain gauge data obtained from structural testing is examined as a plot of the strain versus the point load applied over the course of a structural test. The data produced consistent results within each sample type, therefore one set of strain gauge data from each type of sample will be discussed below in detail. Strain gauges applied to the rebar at mid-depth of the thermal break material are referenced as location 1, and those applied 25 mm from the thermal break to the cantilevered edge will be referenced as location 2, as provided in Figure 43.

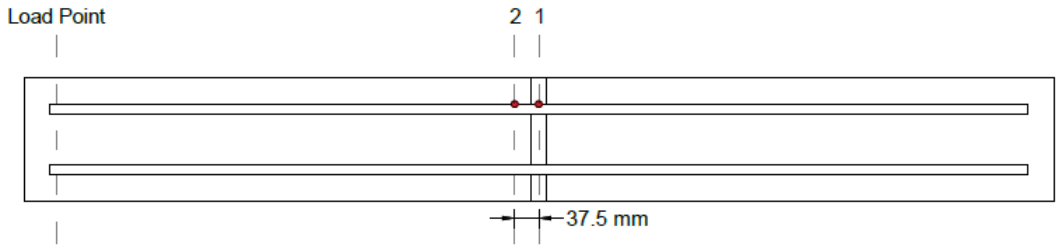

Figure 43 Strain gauge placement

For the GFRP reinforced samples both the top and bottom reinforcing bars were instrumented with strain gauges, therefore four plots obtained from strain gauges applied to two reinforcing bars (one tension reinforcing bar and one compression reinforcing bar) are presented below for the GFRP reinforced samples. Conversely, two plots are presented for each steel and stainless steel sample, obtained from one tension reinforcing bar, as these samples were only installed with strain gauges on the tensile reinforcement.

The first set of results shown in Figure 44 are obtained from sample number one containing GFRP reinforcement with a thermal break. The two strain gauges applied to the tension reinforcement confirm that this reinforcement was subjected to a tensile force for the entire duration of the test. The reinforcement demonstrates linear elastic deformation until failure of the specimen at 63 kN.

The two strain gauges applied to the compression reinforcement demonstrate that this reinforcement was subjected to a compressive force for the entire duration of the test. The reinforcement demonstrates linear-elastic behaviour until a load of approximately 30 and 40 kN for strain gauges at locations 1 and 2, respectively, after which the relationship becomes curvilinear before failure.

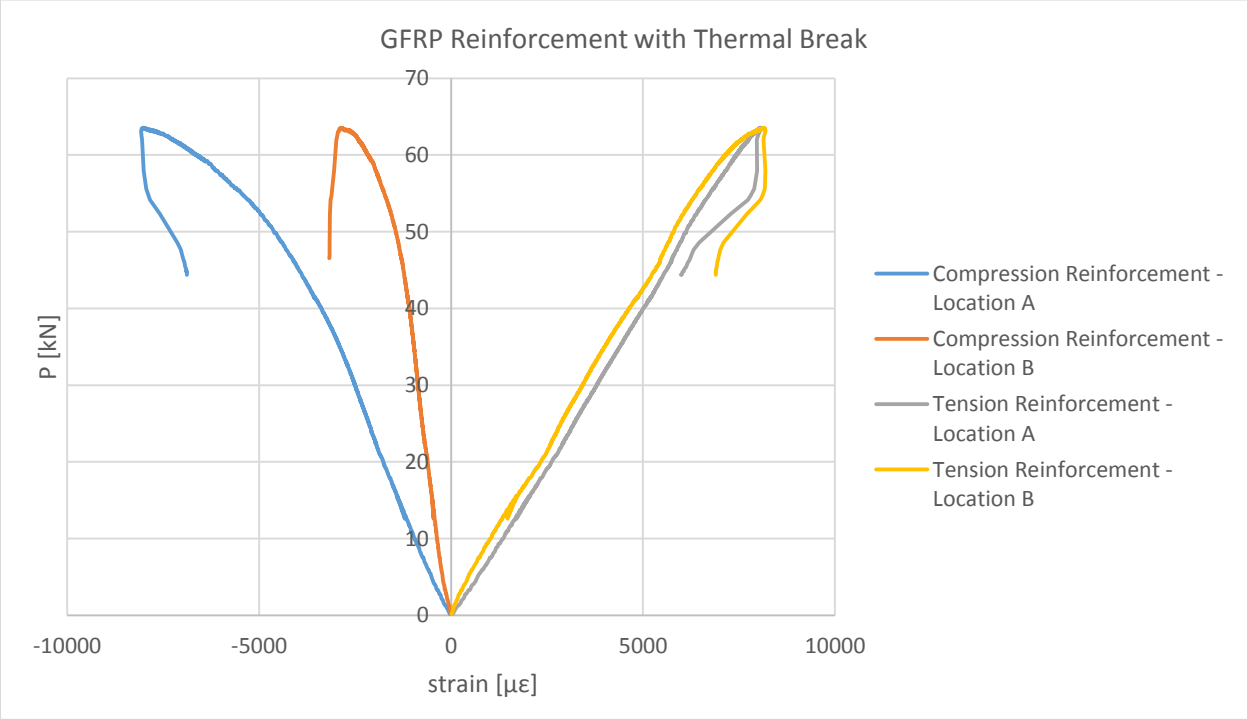

Figure 44 Strain gauge data for a GFRP reinforced sample with a thermal break

The following set of results in Figure 45 are from sample number six containing GFRP reinforcement without a thermal break. The two strain gauges applied to the tension reinforcement demonstrate that this reinforcement was subjected to a tensile force for the entire duration of the test. Both curves are composed of two linear sections with a depression occurring in between. The first linear section demonstrates an

increased slope and therefore increased stiffness in the system until a point load of approximately 13 kN, at which cracking in the concrete first occurs. This increased stiffness is due to the contribution of the concrete to the tensile capacity prior to cracking. The load then again increases as strain increases, but at a shallower slope and therefore a lower stiffness in the reinforcement, until reaching ultimate failure.

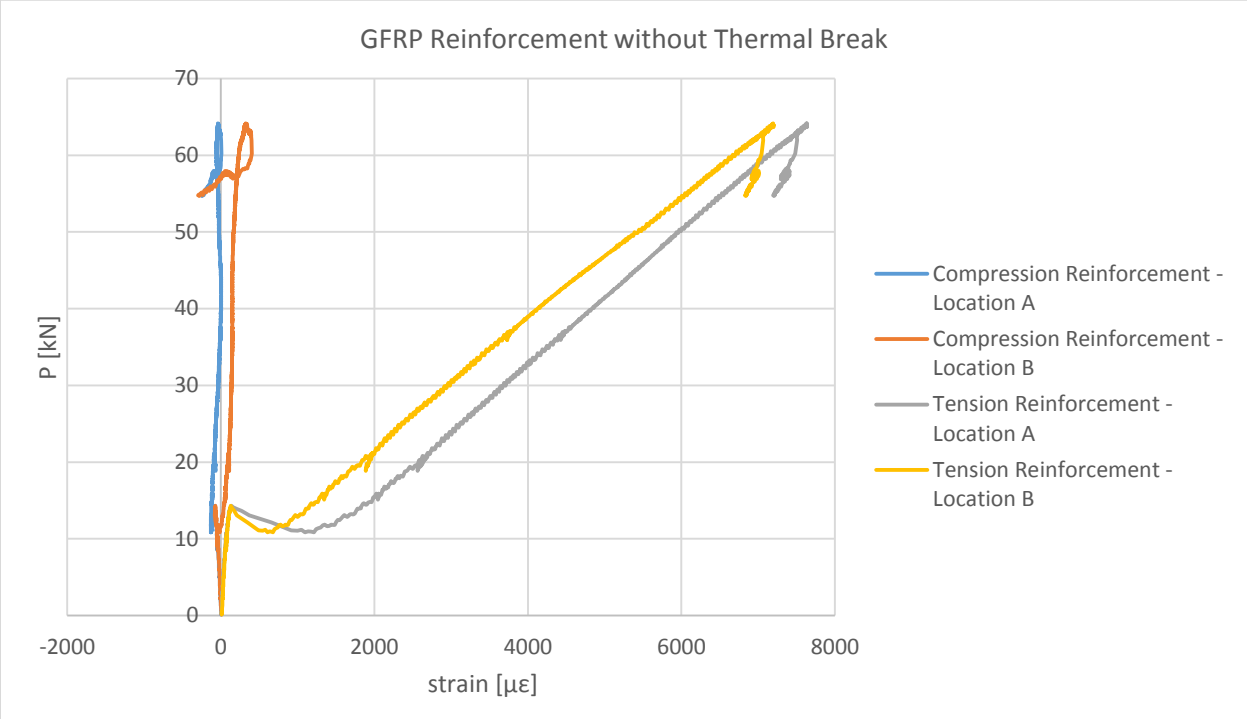

Figure 45 Strain gauge data for a GFRP reinforced sample without a thermal break

The results from the two strain gauges applied to the compression reinforcement demonstrate that the rebar experienced both tensile and compressive forces, indicating a fluctuating neutral axis. The location of the neutral axis over the duration of structural testing is provided in Figure 46. The labels 'Insulation' and 'Concrete' refer to the strain gauges installed in line with the thermal break and immediately adjacent to the thermal break in the concrete, respectively. The labels 'Bar 1' and 'Bar 2' differentiate between the two compressive reinforcing bars in the sample. The height of the tensile and compressive reinforcement are also plotted for reference.

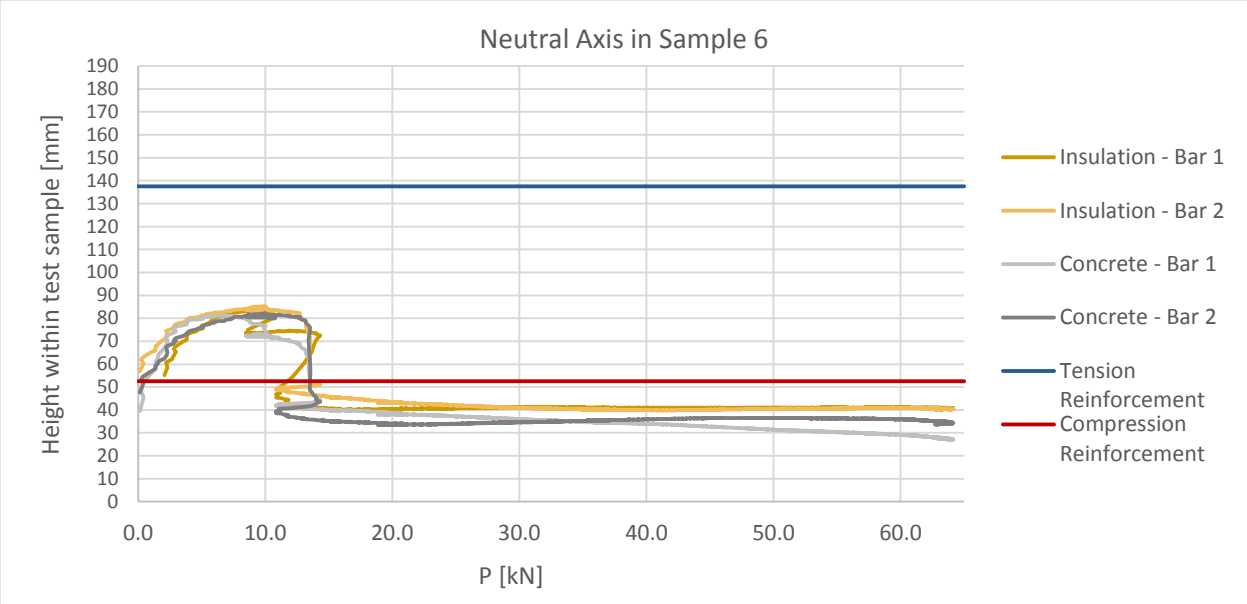

Figure 46 Neutral axis height measured from bottom surface of slab over duration of structural testing for sample 6, containing GFRP reinforcement without a thermal break

Prior to cracking of the concrete at approximately 13 kN, both bottom bars are subjected to compression with the neutral axis located above the compression reinforcement. After cracking of the concrete occurs, the neutral axis lowers and both the tensile and compressive reinforcement are subjected to tension. This indicates that cracking of the concrete has a larger effect on the behaviour of the reinforcement for samples not containing a thermal break. This is expected, as the thermal break provides a discontinuity in the concrete and isolates the behaviour of the reinforcement for samples in which it is installed.

The following set of results in Figure 47 are from sample number 12 containing steel reinforcement with a thermal break. As anticipated, the data from the two strain gauges applied to one of the tensile reinforcement demonstrates that this reinforcement is subjected to tension for the duration of the test. The reinforcement exhibits the typical behaviour of carbon steel subjected to tension, exhibiting linear elastic behaviour until the point of yielding, after which the steel yields and undergoes plastic deformation.

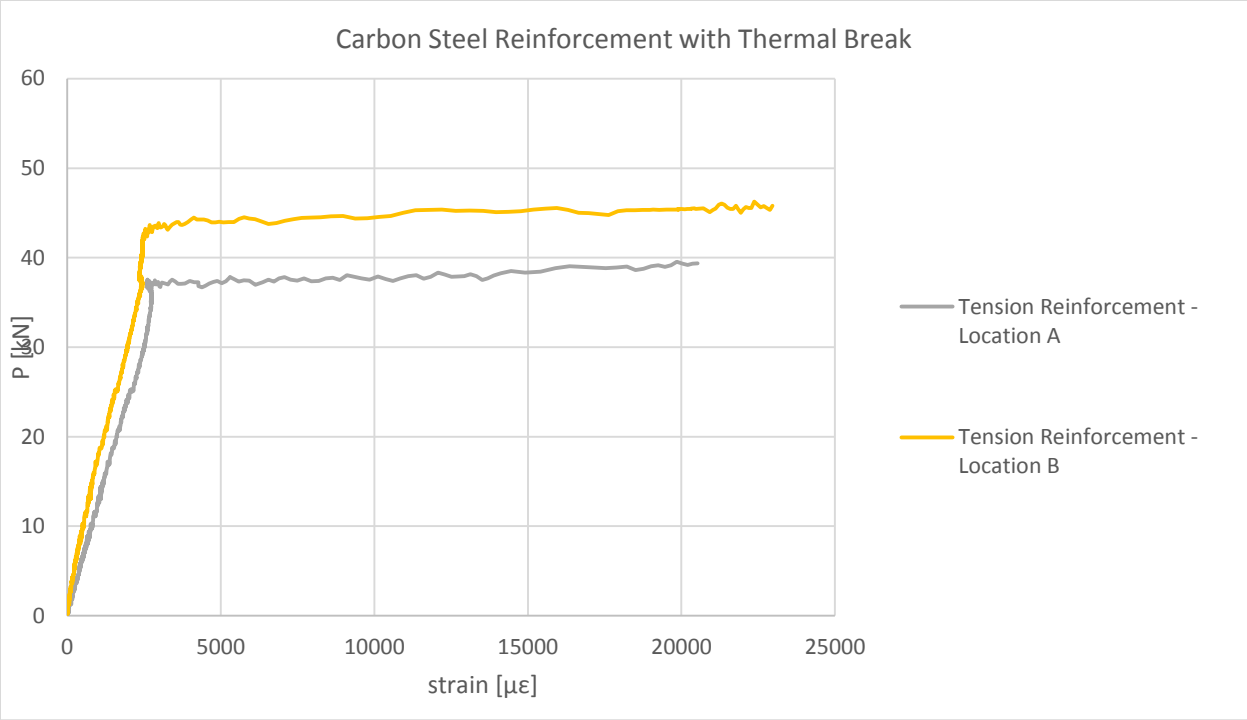

Figure 47 Strain gauge data for a carbon steel reinforced sample with a thermal break

The following set of results in Figure 48 are from sample number 7 containing steel reinforcement without a thermal break. Similar to the GFRP reinforced sample without a thermal break, there is a change in slope occurring at the onset of concrete cracking. The strain increases linearly until concrete cracking initiates at a point load of approximately 14 kN, after which the strain continues to increase but with a shallower slope. This behaviour is typical of a reinforced concrete slab.

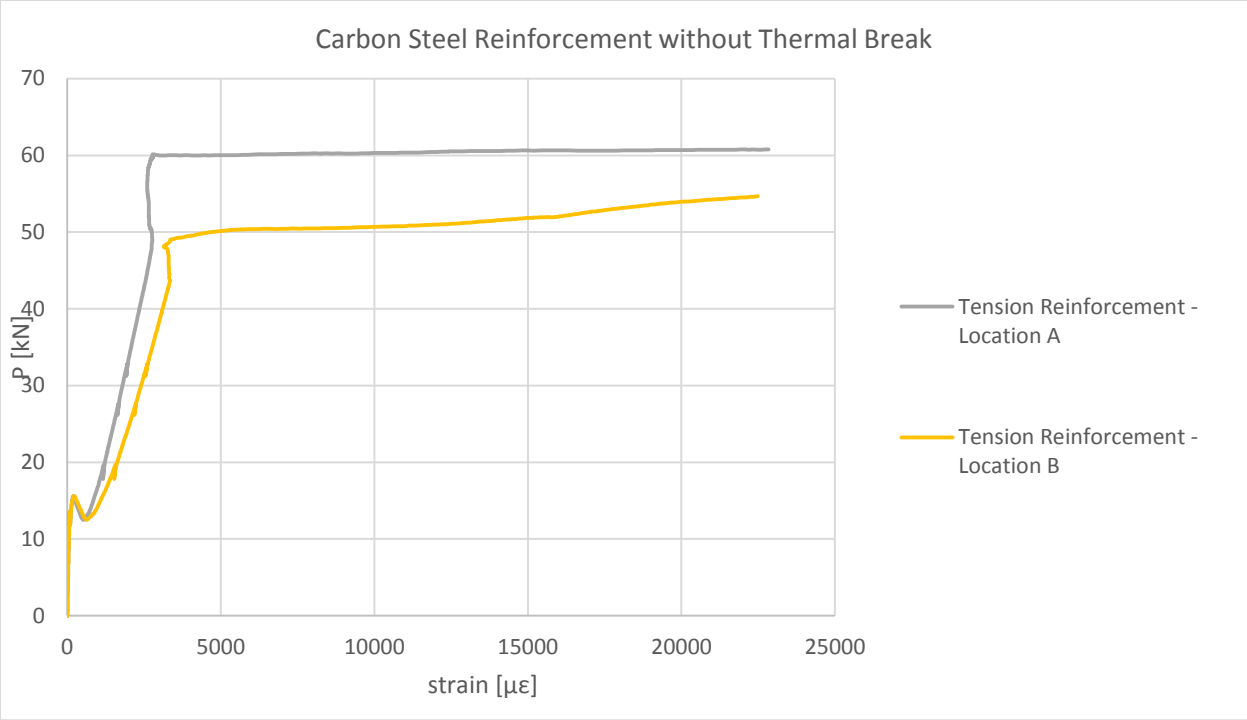

Figure 48 Strain gauge data for a carbon steel reinforced sample without a thermal break

The following set of results in Figure 49 are from sample number 14 containing stainless steel reinforcement with a thermal break. The data shows that the bars were subjected to tension for the duration of the test. The shape of the curve is curvilinear, which is anticipated as this was observed in the tensile tests performed on individual rebar. The minor fluctuations observed along the length of the curve indicate cracking within the concrete. Due to the lower reinforcement ratio used for stainless steel reinforced samples compared to carbon steel reinforced samples the stiffness of the section is lower, allowing for increased deflection and higher amounts of concrete cracking during loading.

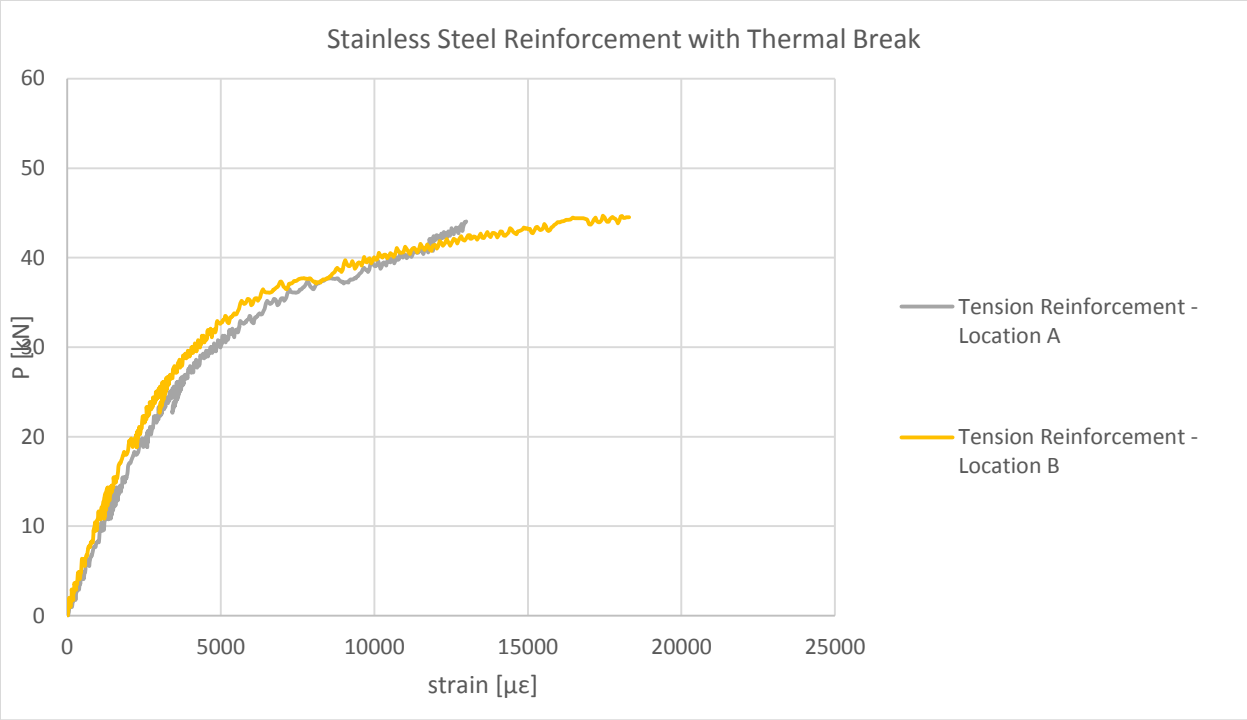

Figure 49 Strain gauge data for a stainless steel reinforced sample with a thermal break

The following set of results in Figure 50 are from sample number 17 containing stainless steel reinforcement without a thermal break. The results are similar to those observed in the samples containing GFRP and carbon steel reinforcement without a thermal break, with an initial steeper slope prior to concrete cracking and a shallower slop after cracking has occurred. The larger fluctuations within the curve are representative of larger concrete cracks, showing that the behaviour of the concrete has a greater impact on the behaviour of the reinforcement for samples without a thermal break. The shape of the curve is again curvilinear due to the properties of the stainless steel rebar.

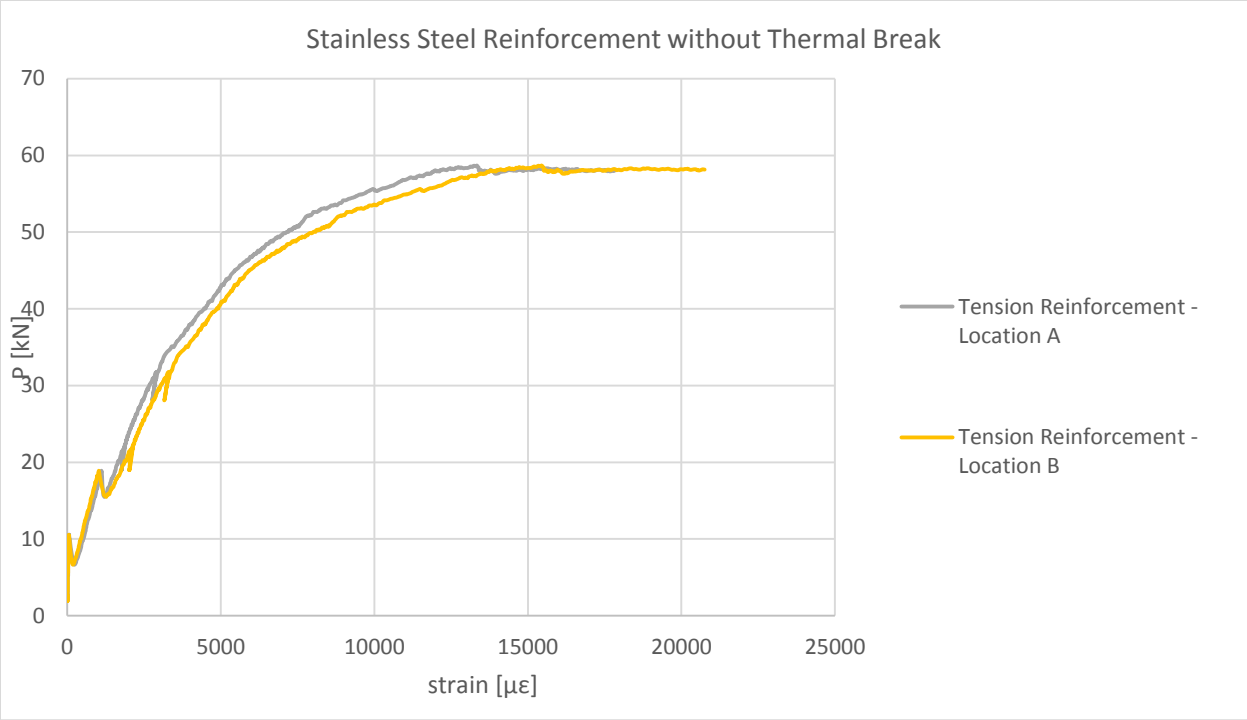

Figure 50 Strain gauge data for a stainless steel reinforced sample without a thermal break

In general, the data obtained from the strain gauges produced the anticipated results. Samples containing the thermal break isolated the behaviour of the reinforcement, whereas in the samples without a thermal break the behaviour of the concrete had a more significant effect on the behaviour of the reinforcement.

4.3.1.2 Deflection Data

The LVDT data obtained from structural testing is examined as a plot of the deflection versus the applied load over the course of a structural test. The data produced consistent results within each sample type, therefore one set of LVDT data from each type of sample will be discussed below in detail. The experimental data for each sample was cut off after the maximum deflection as recorded by the LVDT, as this was used to determine the end of testing.

Figure 51 below presents the LVDT data from samples numbered 2 and 5 containing GFRP reinforcement with and without a thermal break, respectively. The data curve for both samples shows intermittent

decreases in load with an increasing total deflection for the majority of the curve. These intermittent decreases in load are due to cracking within the concrete of the specimen under loading. The deflection curve of both samples is relatively similar until a load of approximately 35 kN, at which the deflection of the sample containing a thermal break begins to increase more rapidly. As anticipated, the final total deflection of sample number 2 containing a thermal break is larger than that of sample number 5 without a thermal break. Immediately prior to failure, the applied load decreases rapidly over a very short time frame while the deflection continues to increase.

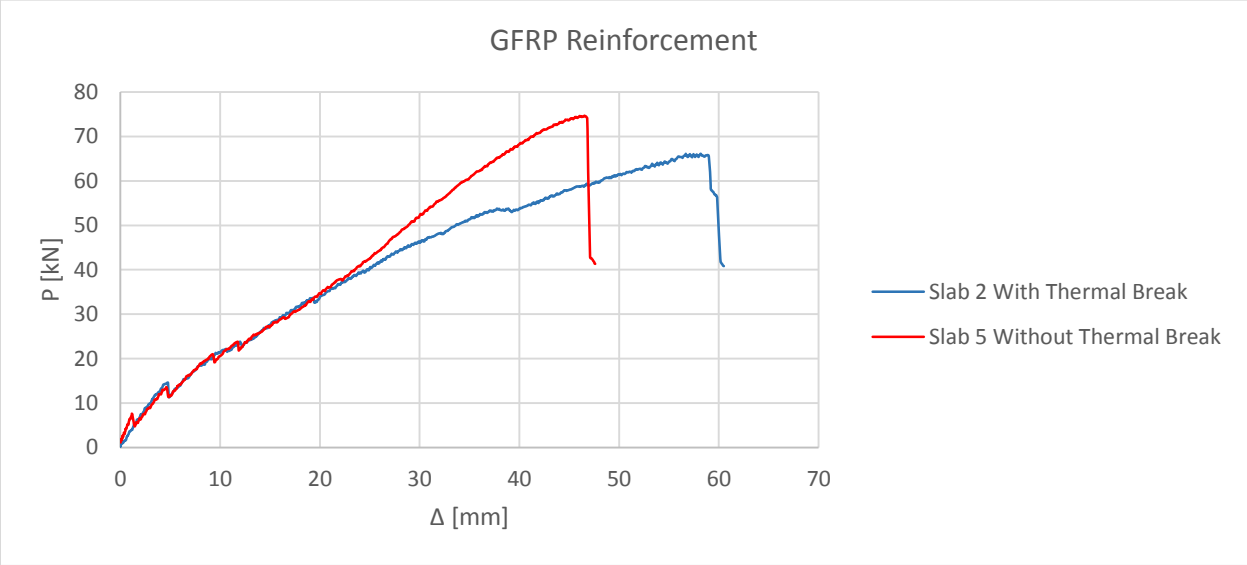

Figure 51 LVDT data obtained from samples containing GFRP reinforcement

Figure 52 below presents the LVDT data from samples numbered 10 and 7 containing steel reinforcement with and without a thermal break, respectively. Again, the data curve for both samples shows intermittent decreases in load with a continuously increasing total deflection up until yielding of the reinforcement. After yielding of the reinforcement, the slope of the curve decreases and the total deflection increases rapidly with minimal increase in applied load. As anticipated, the deflection curve for sample number 10 containing a thermal break is larger than that of sample number 7 without a thermal break for all applied loads.

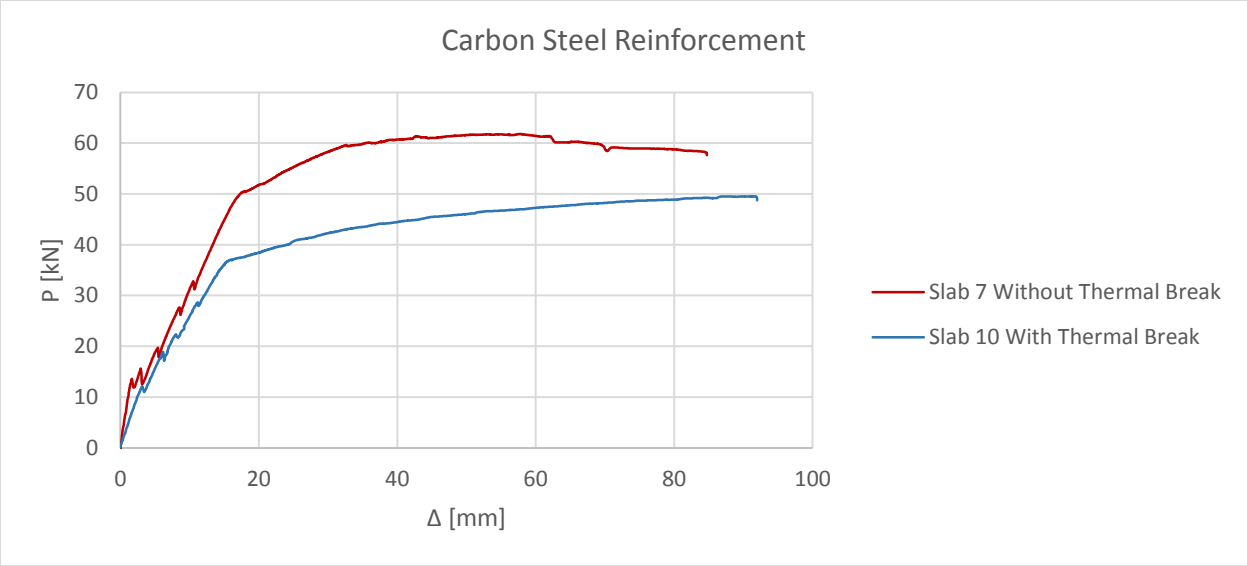

Figure 52 LVDT data obtained from samples containing steel reinforcement

Figure 53 below presents the LVDT data from samples numbered 13 and 18 containing stainless steel reinforcement with and without a thermal break, respectively. As observed for the two previous reinforcement types, the curve for both samples shows intermittent decreases in load with an increasing total deflection for the majority of the curve. The slope of the curve becomes gradually shallower as the steel reinforcement begins to yield, therefore increasing the rate of deflection. As anticipated and as observed with the two previous reinforcement types, the deflection curve for sample number 13 containing a thermal break is larger than that of sample number 18 without a thermal break.

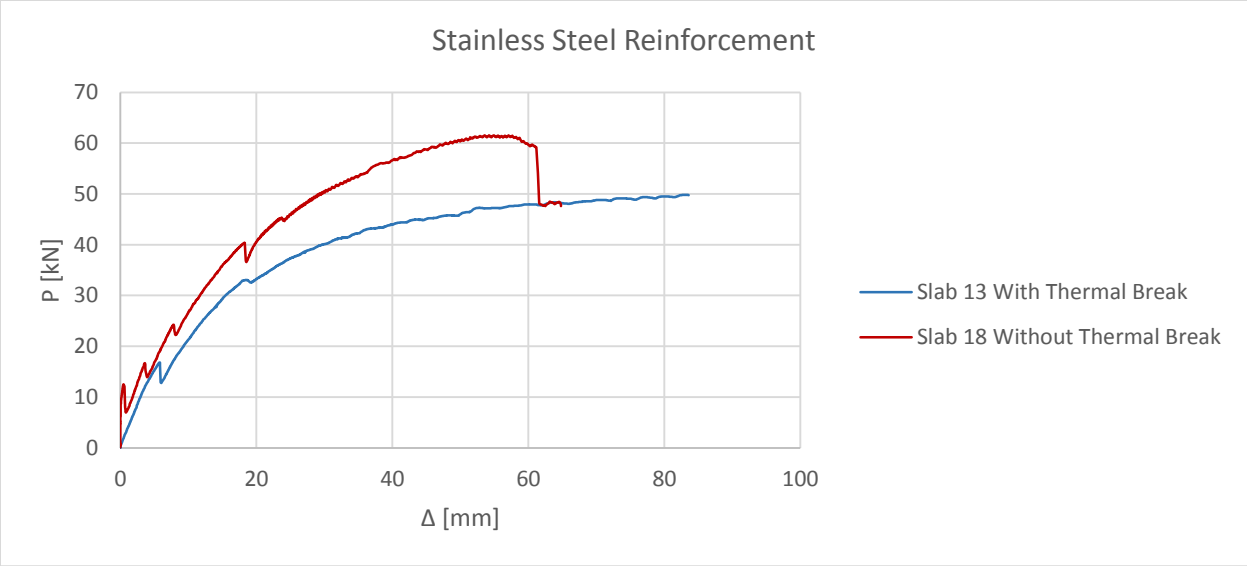

Figure 53 LVDT data obtained from samples containing stainless steel reinforcement

In general, samples containing the thermal break produced a larger deflection than those without a thermal break. This is due to the decrease in stiffness of the system with the introduction of the thermal break. The data obtained from the LVDT sensors will be used in the following sections to further analyse the deflection and serviceability performance of the samples.

4.3.1.3 PI Gauge Data

The PI gauge data obtained from structural testing is examined as a plot of the PI gauge extension versus the applied load over the duration of a structural test. The intention of the PI gauge placement was to capture the rotation of the thermal break.

The data obtained from PI gauges showed to be very inconsistent, regardless of reinforcement type and presence of a thermal break. Below in Figure 54 is an example of data obtained from a sample which produced the anticipated behaviour, taken from sample number 12 containing steel reinforcement with a thermal break. The PI gauge located across the thermal break at the top surface of the sample experiences a significant amount of elongation, increasing rapidly after yielding of the reinforcement. Similarly, the PI

gauge located across the thermal break but at the bottom of the sample experiences a significant amount of compression, also increasing in rate after yielding of the reinforcement. The two PI gauges installed immediately behind the thermal break exhibit a similar behaviour to the two installed across the thermal break but to a much smaller magnitude. For this sample it is concluded that the majority of the rotation recorded by the PI gauges extending across the thermal break is induced by the presence of the thermal break, whereas the rotation recorded immediately behind the thermal break is likely to be induced by cracking of the concrete in this region.

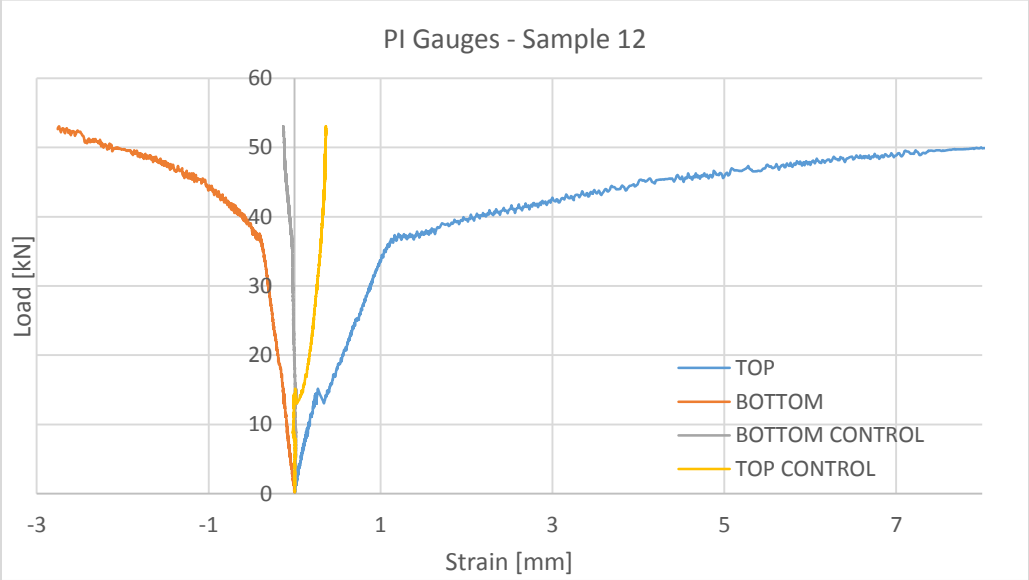

Figure 54 PI gauge data obtained from sample number 12 containing steel reinforcement with a thermal break

Figure 55 below provides the PI gauge data obtained from sample number 2 containing GFRP reinforcement with a thermal break, and does not follow the anticipated pattern. The PI gauge installed at the bottom edge of the sample behind the thermal break registers positive extension over the duration of the test, whereas this area should be compressing. The two PI gauges installed across the thermal break record extension and compression on the top and bottom PI gauges, respectively, indicating rotation of the sample towards the load point.

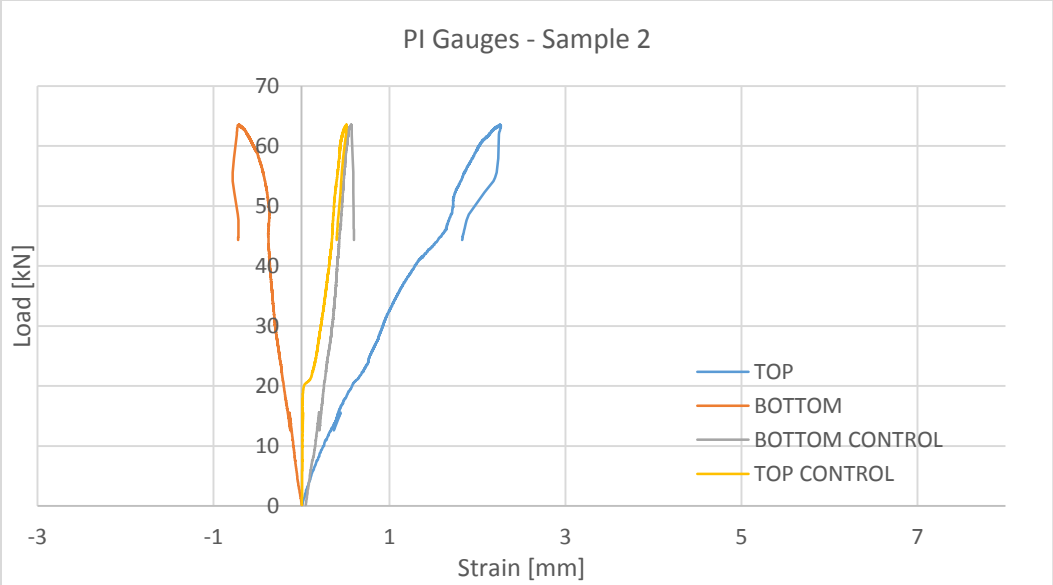

Figure 55 PI gauge data obtained from sample number 2 containing GFRP reinforcement with a thermal break

The rotation at the thermal break for each sample will be presented in Section 4.3.5, calculated based on the two PI gauges installed across the thermal break. The data from sample number 6, containing GFRP reinforcement without a thermal break, was disregarded due to a malfunction of the PI gauges.

4.3.2 Analysis of GFRP Reinforcement in Compression

The following section will investigate the performance of GFRP reinforcement in compression by evaluating the stress and strain distributions within the samples. Figure 56 provides the stress and strain distribution along a GFRP reinforced concrete cross-section subjected to cantilever loading. For a reinforced concrete section, the parabolic stress distribution is replaced by an equivalent rectangular stress block, with the dimensions governed by the parameters α_1 and β_1.

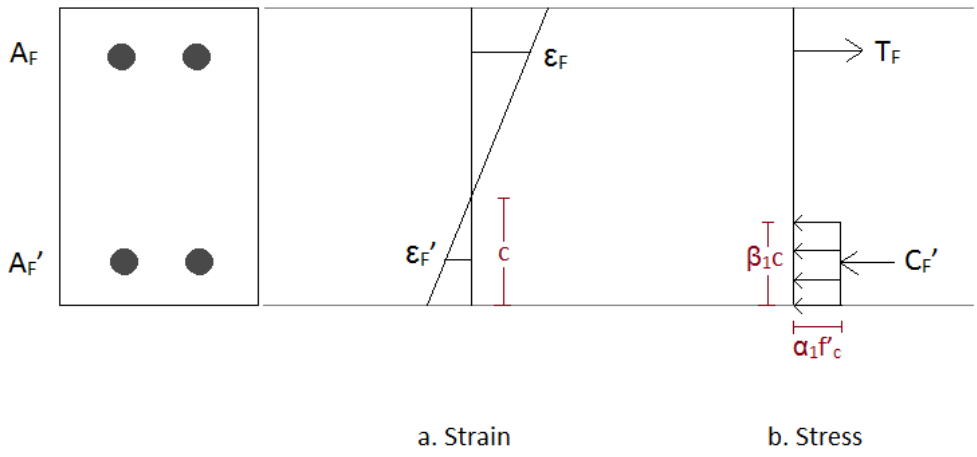

Figure 56 Stress and strain distribution for a GFRP reinforced concrete cross-section

For the thermal break cross-section, the compressive stress distribution within the thermal break is unknown. The parameters α_1 and β_1 applied for concrete may not be used for analysis as they are dependent on the properties and strength of concrete. The properties of the GFRP reinforcement will therefore be investigated by neglecting the capacity of the thermal break, as was done in design, and assuming that all force transferred across the thermal break is carried by the reinforcement. This produces the stress and strain distributions shown in Figure 57.

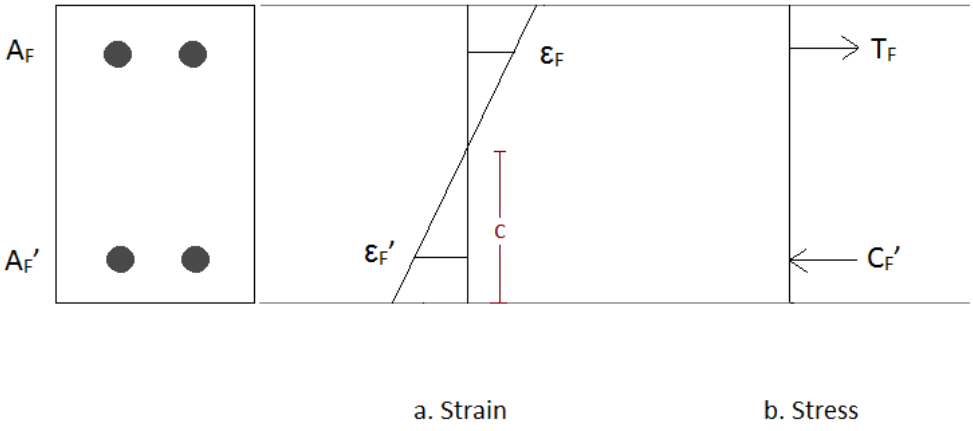

Figure 57 Stress and strain distribution for a GFRP reinforced thermal break, neglecting the capacity of the thermal break

Knowing the applied force during testing, P, and the dimensions of the test setup, the resulting forces in the reinforcement, T_F and C_F', can be calculated according to Equation 9:

$$T_F = -C_F = \frac{Pl}{d} \tag{9}$$

where *l* is the moment arm between *P* and the thermal break and *d* is the vertical distance between the reinforcing bars. Knowing the resulting forces in the reinforcement, and the strain as recorded by the strain gauges during testing, the stresses in the reinforcement, $\sigma_{tension}$ and $\sigma_{compression}$ can be calculated according to Equation 10:

$$\sigma_{tension} = \frac{T_F}{A_F} \tag{10}$$

for the tensile reinforcement and Equation 11:

$$\sigma_{compression} = \frac{-C_F}{A_F{}'} \tag{11}$$

for the compressive reinforcement. From these two values, the modulus of elasticity can be calculated according to Equation 12:

$$E_{tension} = \frac{\sigma_{tension}}{\varepsilon_F} \tag{12}$$

for the tensile reinforcement and Equation 13:

$$E_{compression} = \frac{\sigma_{compression}}{\varepsilon_F{}'} \tag{13}$$

for the compressive reinforcement. The resulting modulus of elasticity for the reinforcement within sample 1 over the duration of loading is provided in Figure 58. As there are two tensile and two compressive reinforcing bars within the width of each test sample, location 1 and 2 each refer to one longitudinal cross-

section containing the reinforcement. The tensile modulus of elasticity for the GFRP, $E_{tension}$, provided by the rebar manufacturer is equal to 66.4 GPa. The average $E_{tension}$ calculated from all samples using this method is equal to 69.3 GPa with a standard deviation of 0.52 GPa.

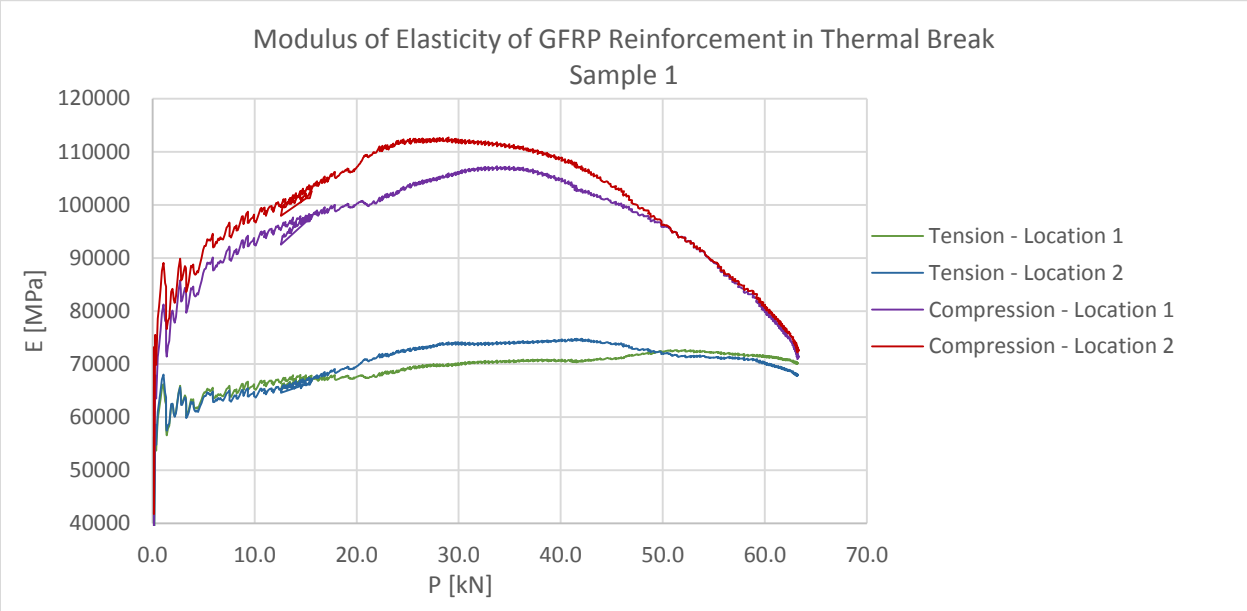

Figure 58 Modulus of elasticity of GFRP reinforcement in thermal break for sample 1, neglecting capacity of thermal break

The tensile reinforcement demonstrates a lower modulus of elasticity for the duration of the test compared to the compressive reinforcement. Given that previous research has found that the compressive modulus of FRP is typically a fraction of its tensile modulus, $E_{compression}$ is likely being influenced by the thermal break. By contributing to the compressive capacity of the cross-section, the thermal break is increasing the stiffness within this region and therefore increasing the calculated modulus of elasticity for the reinforcement when calculated in this method. This indicates that the thermal break does provide a significant contribution to the compressive capacity.

Of interest is the shape of the plot of $E_{comopression}$ over the duration of the test. Until an applied load of approximately 25 kN and 34 kN for bars one and two respectively, $E_{compression}$ is increasing, indicating an increase in stiffness in the system. This may be due to the increasing neutral axis incorporating more depth

of the thermal break to the compressive capacity. After this $E_{compression}$ begins to decrease, indicating a reduction in stiffness in the system and plastic deformation within the compressive region of the thermal break. This is introduced by the plastic deformation of the thermal break material as it experiences crushing under the applied load. .

The strain in compressive reinforcement at onset of plastic deformation in the compressive region of the thermal break is tabulated in

Table 23. There is a significant range in the strain at onset of plastic deformation. The average GFRP strain at onset of plastic deformation is equal to 2,512 micro-strain with a standard deviation of 340 micro-strain.

Table 23 Micro-strain in GFRP reinforcement at onset of plastic deformation within the thermal break

Sample	Bar	Micro-strain at onset of plastic deformation
Sample 1	1	1980
	2	2800
Sample 2	1	2600
	2	2280
Sample 3	1	2900

4.3.3 Test Sample Yielding and Failure Loads

The following section will provide an analysis of the ultimate failure and/or yielding loads observed for all thermally broken samples. The applied load, P, at the cantilevered edge of the sample is provided, as well as the resulting bending moment, M, at the location of the thermal break. For comparison, the theoretically calculated sample strengths are provided.

The GFRP reinforced samples were found to exhibit a brittle shear failure within the concrete. The load at which a brittle shear failure occurred within a GFRP reinforced sample was determined by observing the load-deflection curve of the sample and locating regions where the load decreased suddenly. Small decreases in load indicate small cracks appearing within the concrete and were not deemed to be a brittle

failure, whereas large decreases indicate a significant brittle fracture and were used to indicate the ultimate failure load.

The steel and stainless steel thermal breaks both exhibited yielding of the reinforcement. After yielding, the samples deflected significantly and reached the deflection capacity of the test configuration before concrete crushing. The moment resistance of the thermal break was based on the following Equation 14:

$$M_r = A_s f_y d \tag{14}$$

where A_s is the area of steel in tension, f_y is the steel's yield strength, and d is the distance between the compressive and tensile reinforcement. As such, the moment capacity of the system is based on the yield strength of the reinforcement, and will subsequently be referred to as the yielding moment, or the yielding load when referencing the experimentally applied load that caused yielding. In order to observe the reduction in capacity introduced by the thermal break, the moment at which yielding first occurs in the reinforcement will be compared between the thermally broken and regular concrete slabs. The load at which yielding first occurred within a steel or stainless steel reinforced sample was determined as that at which a strain gauge within the sample first recorded the yield strain. The yield strain for carbon and stainless steel reinforcement were previously determined through rebar tensile testing and were determined to be 0.00315 and 0.00434 for steel and stainless steel, respectively.

4.3.3.1 Ultimate Failure Loads of GFRP Reinforced Samples

Table 24 provides a summary of the ultimate failure loads observed for GFRP reinforced samples with a thermal break. For all samples, the calculated design strengths are lower than those observed experimentally. This may be due to the conservative assumption in design that all force being transferred across the thermal break is carried by the reinforcement, therefore neglecting the capacity of the thermal break material itself. It is also possible that the compressive strength of the GFRP reinforcement was

underestimated, since its compressive strength was taken as the lower end of values provided in literature. Between the three samples tested, the largest percent difference between the ultimate applied load is 4.2%, indicating that the performance of the three samples was consistent.

Table 24 Ultimate failure loads and moments for GFRP reinforced samples with a thermal break

	P_{ult} [kN]	M_{ult} [kN-m]
Calculated	48.8	37.21
SLAB 1	63.5	48.5
SLAB 2	66.1	50.4
SLAB 3	66.3	50.6

samples with a thermal break.

Table 25 provides a summary of the ultimate failure loads observed for GFRP reinforced samples without a thermal break. Again, the calculated design strengths are lower than those observed experimentally. It should be noted that the calculated ultimate load for the GFRP reinforced samples both with and without a thermal break are equal to one another as the shear capacity of the reinforced concrete slab governed in design. The percent difference between the ultimate applied load obtained for samples 5 and 6 is 14.2%, indicating that the performance was less consistent than what was observed for the GFRP reinforced samples with a thermal break.

Table 25 Ultimate failure loads and moments for GFRP reinforced samples without a thermal break

	P_{ult} [kN]	M_{ult} [kN]
Calculated using actual strengths	48.8	37.2
SLAB 5	74.7	56.9
SLAB 6	64.1	48.9

Table 26 provides a summary of the ratio between experimentally observed failure loads and calculated failure loads for all GFRP reinforced samples. Here, the calculated failure load is taken as that calculated using the actual material strengths. For all samples, the observed failure load is significantly larger than the

calculated failure load. The method of calculating the strength of the samples therefore provides a conservative approach. On average the experimental strengths for the samples containing a thermal break are 33.9% larger than the calculated strength. For the samples not containing a thermal break the experimental strengths are on average 42.2% larger than the calculated strengths. This discrepancy is likely due to underestimating the compressive capacity of the GFRP reinforcement.

Table 26 Ratio between experimental failure load and calculated failure load for GFRP reinforced samples

Sample	P_{ult}/P_{calc} [kN]
SLAB 1	1.302
SLAB 2	1.355
SLAB 3	1.359
Average with thermal break	1.339
SLAB 5	1.530
SLAB 6	1.314
Average without thermal break	1.422

On average, a 6% decrease in ultimate load capacity was experimentally observed between the samples reinforced with GFRP without a thermal break and those in which it was included.

4.3.3.2 Yielding Loads of Steel Reinforced Samples

Table 27 provides a summary of the yielding loads observed for steel reinforced samples with a thermal break. For sample number 11, the yielding load was not able to be calculated from experimental data due to a malfunction of the strain gauges. For samples 10 and 12, the calculated yielding load is lower than those observed experimentally. The percent difference between the yielding load for these two samples is 2.5 %, indicating that the performance was consistent.

Table 27 Yielding loads and moments for steel reinforced samples with a thermal break

	P_y [kN]	M_y [kN]
Calculated	34.2	26.1
SLAB 10	36.1	27.5

SLAB 11	N/A	N/A
SLAB 12	35.2	26.8

Table 28 provides a summary of the ratio between experimentally observed yielding loads and calculated yielding loads for the carbon steel reinforced thermal breaks. Here, the calculated yielding load is taken as that calculated using the actual material strengths. The observed yielding load is larger than the calculated yielding load. The method of calculating the strength at yielding for these samples therefore provides a conservative approach. On average the experimental strengths for the samples containing a thermal break are 4.1% larger than the calculated strength.

Table 28 Ratio between experimental failure load and calculated failure load for steel reinforced samples

Sample	P_y/P_{calc} [kN]
SLAB 10	1.055
SLAB 11	-
SLAB 12	1.027
Average with thermal break	1.041

On average, a 16% decrease in ultimate load capacity was observed by introducing a thermal break. The decrease in load carrying capacity is due to the concentration of stresses within the reinforcing bars across the thermal break, leading to yielding of the reinforcement at a lower applied load in comparison to samples without a thermal break.

4.3.3.3 Yielding Loads of Stainless Steel Reinforced Samples

Table 29 provides a summary of the yielding loads observed for stainless steel reinforced samples with a thermal break. It can be seen that the calculated yielding load is marginally larger than the observed experimental yielding load. The percent difference between the yielding load for the two samples is 3.8 %, indicating that the performance was consistent.

Table 29 Yielding loads and moments for stainless steel reinforced samples with a thermal break

	P_y [kN]	M_y [kN]
Calculated	27.3	20.8
SLAB 14	28.7	21.9
SLAB 15	29.82	22.7

Table 30 provides a summary of the ratio between experimentally observed yielding loads and calculated yielding loads for the stainless steel reinforced thermal breaks. The observed yielding load is larger than the calculated yielding load by 7.3% on average.

Table 30 Ratio between experimental failure load and calculated failure load for stainless steel reinforced samples

Sample	P_y/P_{calc} [kN]
SLAB 14	1.052
SLAB 15	1.093
Average with thermal break	1.073

On average, a 19.7% decrease applied load at yielding was observed between the samples reinforced with stainless steel without a thermal break and those in which it was included. As is the case with carbon steel reinforced samples, the decrease in load carrying capacity introduced by the thermal break is due to the concentration of stresses within the reinforcing bars across the thermal break, leading to yielding of the reinforcement at a lower applied load in comparison to samples without a thermal break.

4.3.3.4 General Remarks Regarding Ultimate Failure Loads

In general, the results pertaining to ultimate failure and yielding load from structural experimental testing were found to be more consistent among samples containing a thermal break in comparison to samples without the thermal break. The largest percent difference among samples containing a thermal break was calculated to be 4.2%, 2.5%, and 3.8% for samples containing GFRP, carbon steel, and stainless steel reinforcement, respectively. Comparatively, for samples without a thermal break the largest percent

difference was calculated to be 14.2%, 8.5%, and 6.4% for GFRP, carbon steel, and stainless steel reinforcement, respectively. The high consistency among results from samples containing a thermal break provides confidence in the conclusions drawn upon the newly designed system.

The decrease in ultimate load or yielding load capacity for each of the reinforcement types caused by the introduction of the thermal break is summarized in Table 31. The ultimate failure load of the GFRP reinforced section is only reduced by 6%, which is reasonable given that the failure occurs by concrete shearing. Shearing within the concrete is less influenced by the presence of the thermal break in comparison to the carbon steel and stainless steel reinforced sections, for which the moment capacity of the system is dependent on yielding of the reinforcement.

Table 31 Percent reduction in ultimate load capacity for GFRP reinforced samples and yielding load for carbon and stainless steel reinforced samples

Reinforcement Type	Percent Reduction [%]
GFRP	6
Carbon Steel	16
Stainless Steel	20

For all samples containing a thermal break, the calculated ultimate capacity was found to be lower than the experimentally obtained ultimate capacity. This indicates that the methods and assumptions used to calculate the system's capacity provide a conservative approach. For steel and stainless steel reinforced samples, in which yielding of the reinforcement at the location of the thermal break governs in design, the approach for calculating the capacity of the thermal break is underestimated by neglecting the capacity of the thermal break material itself.

The largest discrepancy between calculated and experimental ultimate loads was found for the GFRP reinforced samples, with the experimental capacity on average 33.9% higher than the calculated capacity. Shear failure of the reinforced concrete section governed in design for the GFRP reinforced samples both

with and without a thermal break. Comparatively, steel reinforced samples containing a thermal break yielded at a load on average 4.1% higher than the calculated capacity, while stainless steel reinforced samples yielded at a load on average 7.3% higher. The larger discrepancy for GFRP reinforced samples is likely due to underestimating the compressive strength of the GFRP.

Given that the cast in place balcony thermal break is a novel design which has not yet been introduced to industry, providing a conservative approach to calculating the strength of the system is ideal in order to persuade the industry to implement it in projects. Although the approach of neglecting the capacity of the thermal break may not provide an accurate analysis to the behaviour of the system, the results above show that it is a conservative method to predict the load carrying capacity of the system containing a thermal break.

4.3.4 Structural Failure Modes and Yielding Behaviour

The following section will present photographs taken during structural testing in order to identify and discuss failure modes and general behaviour of the samples. For sample types that failed or performed in the same manner, representative images from one sample will be provided for discussion. Figure 59 is provided below to show the structural test set up and to provide a reference for labelling areas in the following photographs. For clarity, all images will be shown from the same direction with the load point to the left hand side.

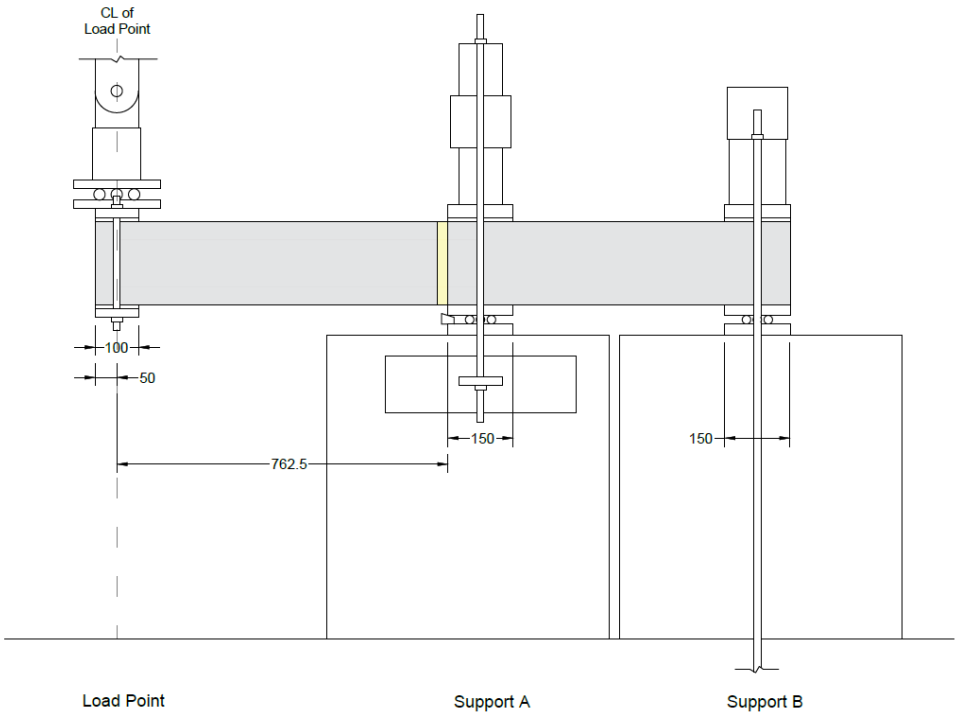

Figure 59 Structural Test Setup

4.3.4.1 Structural Failure Modes of GFRP Reinforced Samples

As anticipated based on design calculations, the samples containing GFRP reinforcement with a thermal break failed by shearing of the concrete, at two different locations within the slabs. Figure 60 provides two images taken of sample number 1, containing GFRP reinforcement with a thermal break. Shown on the right half of each image is Support A, with the load point towards the left. The thermal break material is visible and is immediately to the left of Support A. The most notable behaviour within this sample is the shear cracking, visible to the left of the thermal break. As the structural test progressed and load increased, the shear cracking continued to widen until ultimate load was reached, at which a brittle shear failure occurred along the plane shown by the cracking below.

Figure 60 Concrete shear cracking in sample 1 immediately adjacent to support A between support A and the load point a) early on in testing but after ultimate design load and b) shortly before ultimate failure.

Minor flexural cracking also appeared over the duration of the test immediately behind support A, as shown in Figure 61, due to the minor curvature of the slab at this location. This cracking was present for all samples tested in the experiment, regardless of reinforcement type or presence of the thermal break, and appeared very early on in testing for all samples. The fixity of support A was increased in order to minimize the curvature at this location and isolate the structural behaviour of the thermal break. It is recognised however that due to stresses carried through the concrete by the reinforcement it is not possible to entirely eliminate curvature in this location, and therefore minor cracking is acceptable.

Figure 61 Concrete flexural cracking between support A and B on sample 1

Figure 62 shows sample number 2, containing GFRP reinforcement with a thermal break, immediately prior to failure. Ultimate failure of this sample again occurred by shearing of the concrete to the left of Support A, along the shear plane shown by cracking below.

Figure 62 Concrete shear cracking immediately prior to failure in Sample 2

Figure 63 and Figure 64 provide images of Sample 3, containing GFRP reinforcement with a thermal break during structural testing. Figure 63 shows the presence of shear cracking occurring to the left of Support A towards the load point, prior to ultimate failure, as was also observed for Samples 1 and 2. Figure 64

however shows the sample after ultimate failure, which occurred by shearing of the concrete between support A and support B. Due to the configuration of the testing setup, the magnitude of the shear force within the sample between the load point and support A, as well as that between support A and support B, were equal in magnitude and equal to the applied point load. Therefore it is dependent on each individual sample whether the ultimate failure was to occur to the left or to the right of support A.

Figure 63 Concrete shear cracking to the left of Support A prior to ultimate failure in sample 3

Figure 64 Concrete shear failure occurring between support A and B in sample 3

Samples containing GFRP reinforcement without a thermal break also exhibited shear failure within the concrete, as was observed for the GFRP reinforced samples containing a thermal break. Figure 65 shows

sample number 5 after having reached ultimate failure load, at which a brittle shear failure occurred between supports A and B, similar to the failure seen in sample 10 above.

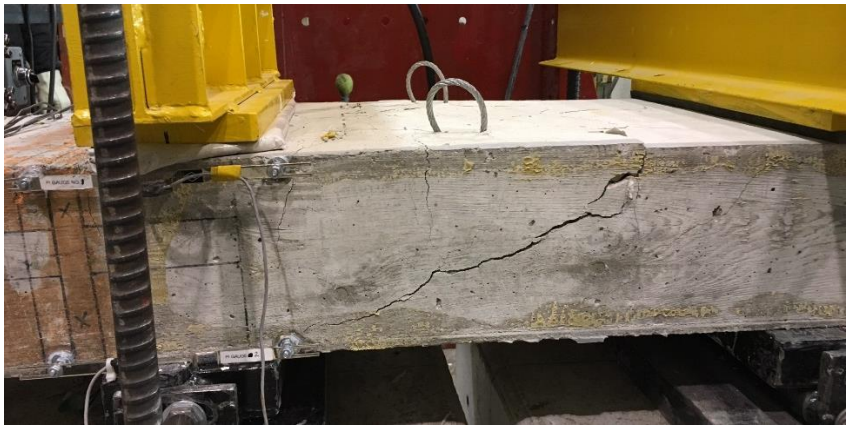

Figure 65 Concrete shear failure between support A and support B in sample 5

Figure 66 shows sample number 6, also containing GFRP without a thermal break, after having reached ultimate load at which a brittle shear failure occurred between support A and the load point. Compared to shear failure occurring at this location in samples containing a thermal break, the angle of the shear cracking occurred at a steeper slope, and therefore the shear crack propagated a longer length along the slab towards the load point.

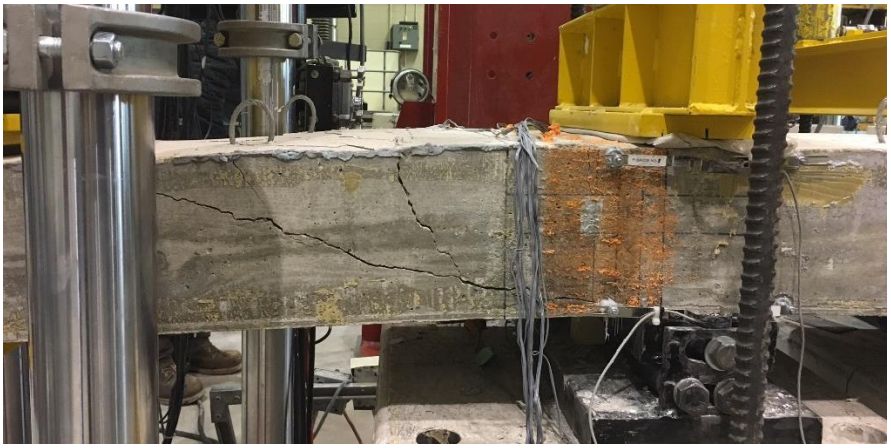

Figure 66 Concrete shear failure between support A and the load point in sample 6

A preferred or ideal mode of failure within the above system would be by gradual crushing of the thermal break material, which would progress gradually and provide warning. However, given that the system design concluded that the shear strength of the concrete would govern, for both samples with and without a thermal break, and the experimental results reflected as such, this is a positive outcome.

4.3.4.2 Yielding Behaviour of Carbon Steel Reinforced Samples

As anticipated based on design calculations, the samples containing carbon steel reinforcement both with and without a thermal break experienced yielding of the steel reinforcement.

The image provided in Figure 67 is taken of sample number 10, containing steel reinforcement with a thermal break. This image was taken very shortly prior to yielding of the steel reinforcement, and shows the thermal break immediately adjacent to support A, with the load point out of frame to the left. Very minimal separation between the thermal break material and the concrete is present.

Figure 67 Image of sample number 10 showing minimal opening of the thermal break prior to steel yielding

Figure 68 shows sample number 10 again, however after yielding of the steel reinforcement. Flexural shear cracks have begun to appear to the left of support A. Minor flexural cracking also appeared between support A and B over the duration of the test for all steel reinforced samples, both with and without a thermal break, due to the curvature of the sample. Most notably, the separation between the thermal break and concrete has significantly increased.

Figure 68 Image of sample number 10 after yielding of the steel reinforcement

Figure 69 shows sample number 11, also containing steel reinforcement with a thermal break, at the end of structural testing with the steel reinforcement fully yielded. The sample has deflected significantly due to the elongation of the reinforcing bars after yielding. The lack of bond between the reinforcing bars and the thermal break material allows for the bars to yield unrestrained in this location, increasing the total deflection of the samples.

Figure 69 Deflection of sample number 10 at the end of testing

Figure 70 shows sample number 8, containing steel reinforcement without a thermal break, after yielding of the reinforcement. The image shows support A with the location where a thermal break would be installed immediately to the left of it, with the load point to the left out of the frame of the image. Flexural cracking occurred to the left of support A, and increased significantly in width after yielding of the reinforcement.

Figure 70 Sample number 8 after yielding of the steel reinforcement

Sample number 8 is shown again in Figure 71, showing the deflection of the sample at the end of testing. It is noted that the curvature of this sample is gradual over its length, in comparison to sample number 10 shown in Figure 69, in which the curvature is concentrated about the thermal break.

Figure 71 Figure 15 Deflection of sample number 8 at the end of testing

As designed, the steel reinforced samples both with and without a thermal break reached yielding of the steel reinforcement before exhibiting any mode of ultimate failure. Yielding of the steel reinforcement prior to concrete crushing is desirable as the steel will deflect after yielding and provide significant warning before ultimate collapse. As seen above, the presence of the thermal break allows for the steel to elongate unrestrained at this location, therefore increasing the curvature across the thermal break significantly after yielding. Yielding of the reinforcement also greatly increases the separation between the thermal break and concrete, exposing the reinforcing bars. Additional design considerations will need to be included to protect the reinforcing bars from corrosive elements that may be introduced through the opening, as well as to maintain the fire resistance of the system.

4.3.4.3 Yielding Behaviour of Stainless Steel Reinforced Samples

Stainless steel reinforced samples performed very similarly to steel reinforced samples during structural testing in terms of physical performance and yielding. As anticipated based on design calculations, the

samples containing stainless steel reinforcement both with and without a thermal break experienced yielding of the reinforcement.

Figure 72 is taken of sample number 13, containing stainless steel reinforcement with a thermal break. This image was taken very shortly prior to yielding of the stainless steel reinforcement, and shows the thermal break immediately adjacent to support A, with the load point out of frame to the left. Separation is visible between the thermal break and concrete.

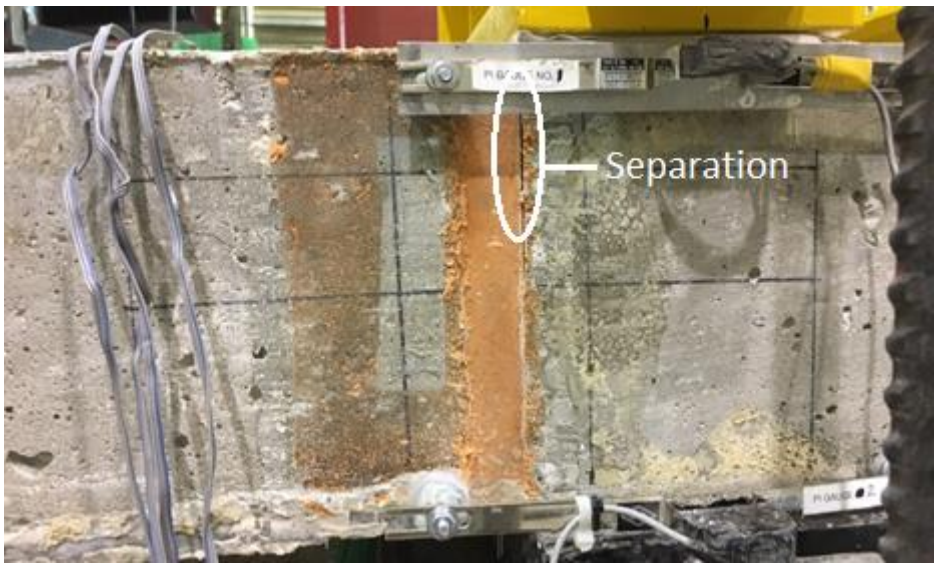

Figure 72 Sample 13 prior to yielding of the stainless steel reinforcement

Figure 73 shows sample 13 again, however after yielding of the stainless steel reinforcement. As was the case with carbon steel reinforced samples containing a thermal break, flexural shear cracking has appeared to the left of support A towards the load point, and the separation between the thermal break and concrete has significantly increased.

Figure 73 Sample 13 after yielding of the stainless steel reinforcement

Figure 74 shows sample 16, containing stainless steel reinforcement without a thermal break, after yielding of the reinforcement. As was seen with steel reinforced samples without a thermal break, flexural cracking has appeared in the tension zone to the left of support A towards the load point. The curvature along the length of the sample is again gradual, in comparison to the stainless steel reinforced samples with a thermal break in which the curvature is concentrated over the thermal break.

Figure 74 Sample 16 after yielding of the stainless steel reinforcement

As designed, the stainless steel reinforced samples both with and without a thermal break reached yielding of the reinforcement before exhibiting failure, such as concrete crushing. The samples performed very similarly to steel reinforced samples in terms of physical performance and failure modes. Significant separation between the thermal break and concrete was again present after yielding of the reinforcement, and curvature along the sample was visibly concentrated about the thermal break for samples in which it was included.

4.3.5 Thermal Break Rotation

The rotation across the thermal break, Φ, of each sample was calculated based on the data recorded by PI gauges according to Equation 15 as follows

$$\Phi = \frac{\Delta_{top} - \Delta_{bottom}}{h} \tag{15}$$

where Δ_{top} is the extension recorded by the top PI gauge, Δ_{bottom} is the contraction recorded by the bottom PI gauge, and h is the vertical distance between the two PI gauges, equal to 172 mm.

The rotation for all GFRP reinforced samples is presented in Figure 75. It is apparent that sample number 5, without a thermal break, presents less rotation than the three samples containing a thermal break. The rate of increase in rotation for all samples is approximately linear in relationship with the applied load, which is reflective of the linear-elastic behaviour of the GFRP.

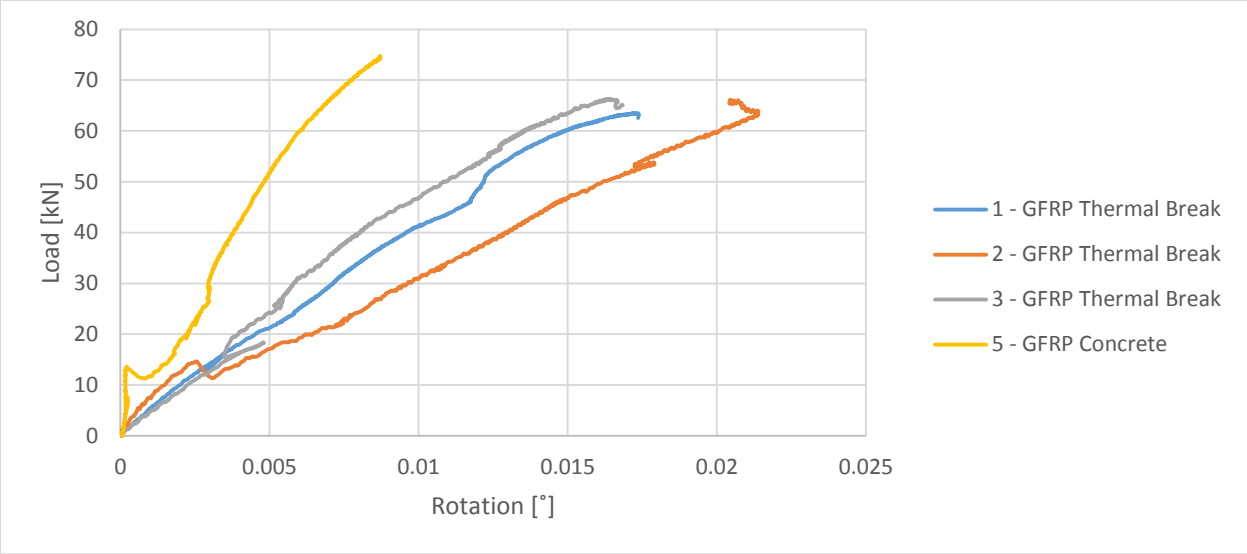

Figure 75 Thermal break rotation for GFRP reinforced samples

The rotation for all carbon steel reinforced samples is presented in Figure 76. Consistent behaviour is observed among the samples. The rate of increase in rotation with respect to the applied load is significantly higher after yielding of the reinforcement.

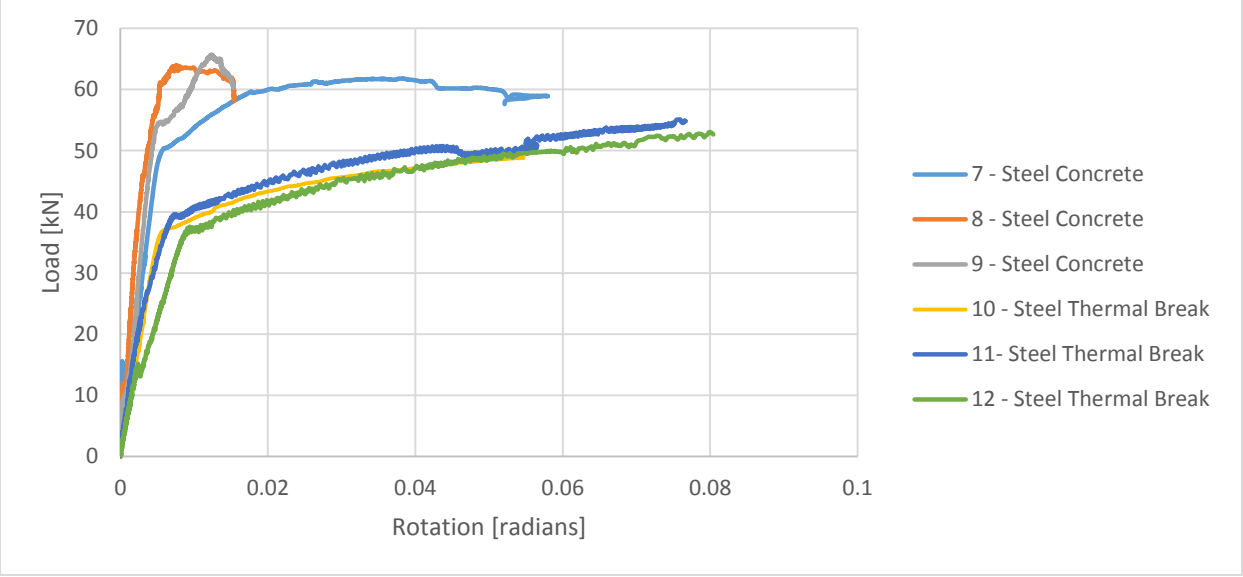

Figure 76 Thermal break rotate on for carbon steel reinforced samples

The rotation for all stainless steel reinforced samples is presented in Figure 77. The behaviour is generally inconsistent, with sample number 13 containing a thermal break demonstrating lower rotation than

samples 16 and 18 without a thermal break for a range of applied load. The rate of increase in rotation with respect to the applied load again increases due to yielding of the reinforcement, with the roundhouse curve shaped observed during yielding of stainless steel.

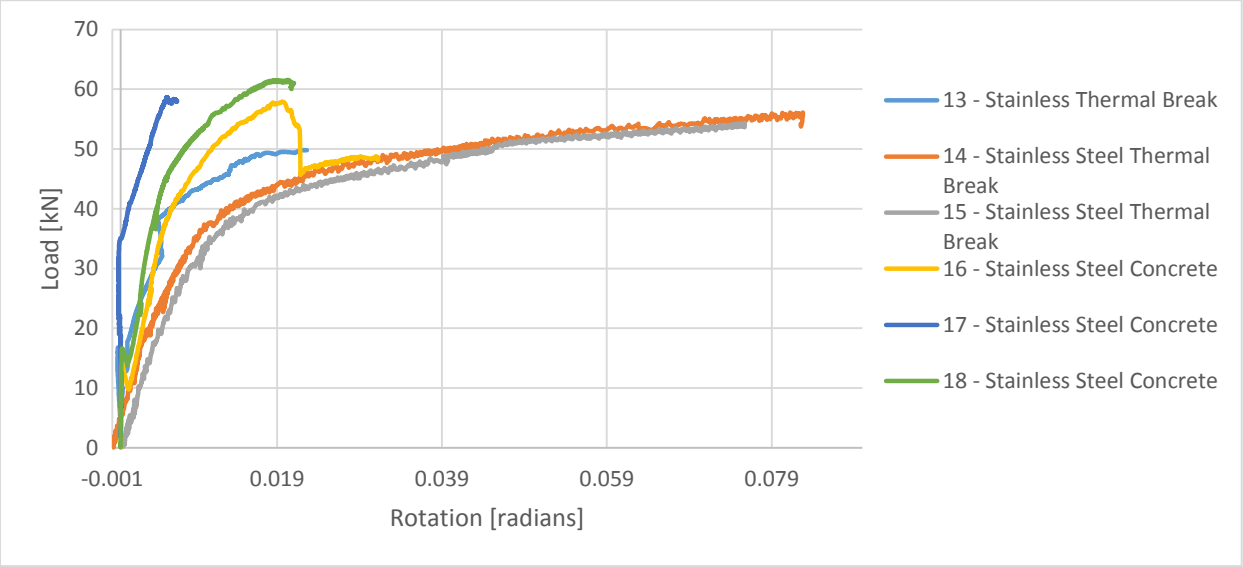

Figure 77 Thermal break rotation for stainless steel reinforced samples

The average rotation of each sample type at the equivalent service load, P_s, is presented in Table 32. A significant increase in rotation is introduced by the thermal break, equal to 109% on average for all samples. This is due to the lack of bond between the thermal break-concrete interface and therefore reduced stiffness at this section. The standard deviation of the rotation is significant, equal to 21%, 24%, and 61% of the average observed rotation for the GFRP, carbon steel, and stainless steel reinforced samples, respectively. This indicates that the behaviour of the thermal breaks in terms of rotation is variable from sample to sample.

Table 32 Rotation calculated at equivalent service load

		Average Rotation [radians]	Standard Deviation	% Increase by Thermal Break
GFRP	Thermal Break	0.0049	0.06	117
	No Thermal Break	0.0023	N/A	
Carbon Steel	Thermal Break	0.0031	0.05	88
	No Thermal Break	0.0017	0.02	
Stainless Steel	Thermal Break	0.0033	0.09	122
	No Thermal Break	0.0014	0.06	

4.3.6 Sample Deflection

The following section will investigate the deflection of the samples. The experimental deflection is evaluated at the equivalent service load, P_s, equal to 19.7 kN. According to the design calculations for the thermal break systems, in order to accommodate the deflection requirements as prescribed by the National Building Code of Canada the systems would need to be installed with a precamber. The following results will therefore not be compared directly to the allowable deflection as prescribed by the National Building Code of Canada, which is equal to the span length divided by 360. This provides an allowable deflection equal to 2.12 mm, which as shown in the following results is exceeded by all samples. The increase in deflection of the samples with the introduction of a thermal break will therefore be focused upon, and the required precamber for each sample to meet the deflection requirements will be discussed.

Table 33 below provides the experimental deflection for GFRP reinforced samples. The average observed deflection at service load for samples without a thermal break is equal to 9.63 mm. Conversely to what was anticipated, the average observed deflection at service load for samples with a thermal break is 9% smaller and equal to 8.77 mm. When observing the data from individual test results, sample number 5 without a thermal break deflected nearly the same amount as samples with a thermal break. Sample number 6 however, deflected 2.08 mm further than sample number 5, for a total of 10.67 mm, which significantly increased the average deflection. The variation in deflection within samples of the same type may be due

to the inconsistent nature of concrete cracking, which is dependent on the aggregate placement and concrete compaction of each individual sample, which impacts the stiffness of the sample. It may also be influenced by the inconsistent behaviour of GFRP reinforcement in compression.

Table 33 Deflection at service load for GFRP reinforced samples

	Sample	Deflection [mm]	Required Precamber [mm]
Samples with Thermal Break	1	8.84	
	2	8.77	
	3	8.69	
	Average	8.77	7
Samples without Thermal Break	5	8.59	
	6	10.67	
	Average	9.63	8

The deflection of the GFRP reinforced samples over the duration of testing is plotted in Figure 78. It is observed that at the service load conditions, the samples containing a thermal break are deflecting less than those with a thermal break. Considering the stiffness of the thermal break material and concrete, which are equal to 49.3 GPa and 29.2 GPa, respectively, it is understood that the thermal break is effectively increasing the stiffness of this cross-section and therefore reducing deflection. When plastic deformation begins to occur in the thermal break, at approximately 33 kN, a reduction in stiffness in the thermally broken samples is observed and they begin to deflect more than the samples without a thermal break. In general, this provides very good results for the GFRP reinforced thermal breaks as they provide a reduction in deflection under service conditions.

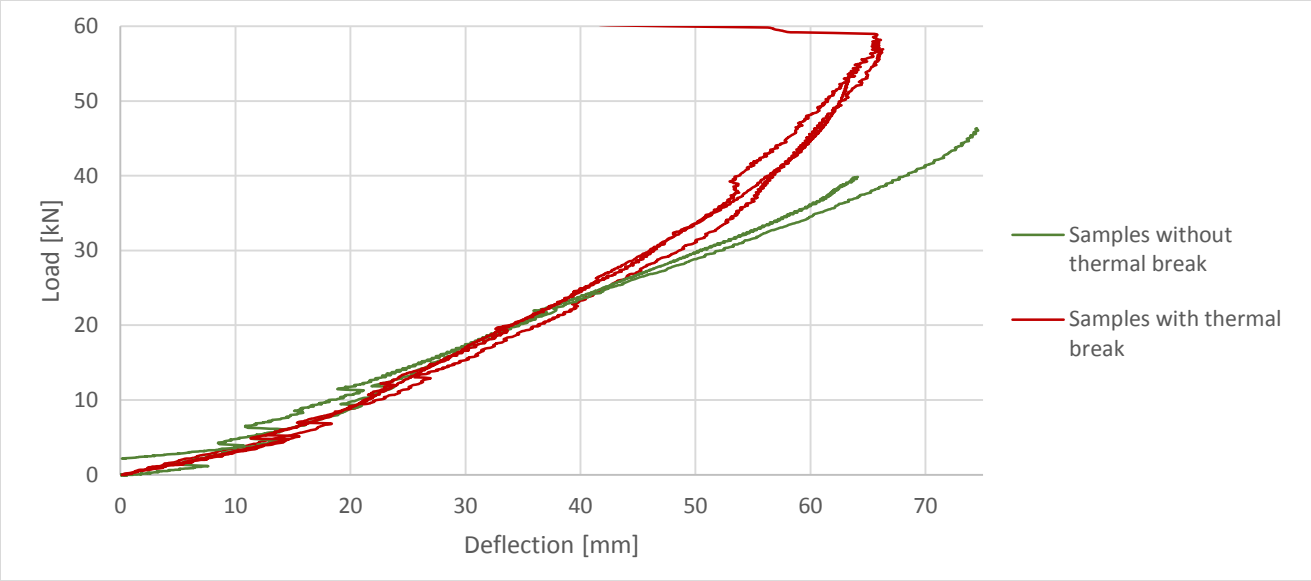

Figure 78 Deflection of GFRP reinforced samples

Table 34 below provides the experimental deflection for steel reinforced samples. The average observed deflection at service load for samples without a thermal break is equal to 6.59 mm. The samples containing a thermal break deflected on average 9.7% more, with an average deflection of 7.3 mm. This confirms the anticipated behaviour of the thermal break increasing the total deflection of the sample, and is opposite to what was observed for the GFRP reinforced samples. In terms of the required precamber, the presence of the thermal break increases the required precamber by 13.9%.

Table 34 Deflection at service load for steel reinforced samples

	Sample	Deflection [mm]	Required Precamber [mm]
Samples with Thermal Break	10	6.97	
	11	7.45	
	12	7.48	
	Average	7.30	6
Samples without Thermal Break	7	5.96	
	8	5.83	
	9	7.97	
	Average	6.59	5

Table 35 below provides the experimental deflection for stainless steel reinforced samples. The average observed deflection at service load for samples without a thermal break is equal to 7.08 mm, which is increased by 36.7% to 11.18 mm for samples containing a thermal break. This again confirms the anticipated behaviour. The stainless steel reinforced section with a thermal break deflects 34.7% more than the equivalent sample containing steel reinforcement. This is due to the decrease in reinforcement ratio, where the stainless steel reinforcement is placed at 250 mm on center, whereas the steel reinforcement is placed at 167 mm on center, providing an overall higher stiffness to the system. In terms of the required precamber, the presence of the thermal break increases the required precamber by 45.3%.

Table 35 Deflection at service load for stainless steel reinforced samples

	Sample	Deflection [mm]	Required Camber [mm]
Samples with Thermal Break	14	11.01	
	15	11.34	
	Average	11.18	9
Samples without Thermal Break	16	7.44	
	17	7.79	
	18	6.02	
	Average	7.08	5

The deflection data observed for the steel and stainless steel reinforced samples produced the anticipated results, with these samples showing a significant effect on the sample deflection when thermal break was included. The samples containing a thermal break deflected on average 9.7% and 36.7% more than those without a thermal break for samples reinforced with steel and stainless steel, respectively. The increase in deflection for the stainless steel reinforced samples is due to their lower reinforcement ratio, with the stainless steel samples containing 66% as much reinforcement area as the carbon steel samples. This indicates that the influence of the thermal break on increasing deflection is larger for sections with a lower initial stiffness.

For GFRP reinforced samples, the behaviour of the two sample types was not significantly different. The samples containing GFRP reinforcement deflected 9% less for samples containing a thermal break when compared to those without. This is most likely due to the fact that GFRP reinforcement in tension has a linear stress strain relationship, exhibiting linear elastic behaviour until failure. Therefore, the deflection of the samples is not increased by the plastic deformation of the reinforcement as is the case with carbon and stainless steel reinforced samples. This indicates that the GFRP reinforced thermal break provides the best performance in terms of serviceability and deflection requirements in comparison to the carbon and stainless steel reinforced thermal breaks.

4.3.7 Summary

The structural experimental results pertaining to ultimate and yielding loads, rotation at service load, and deflection at service load are summarized in Table 36.

Table 36 Summary of structural experimental results

Sample Type		Ultimate Failure (GFRP) or Yielding (Carbon and Stainless Steel) Load [kN]	Rotation at Service Load [radians]	Deflection at Service Load [mm]
Carbon Steel	Thermal Break	35.7	0.0031	7.30
	No Thermal Break	42.6	0.0017	6.59
Stainless Steel	Thermal Break	29.3	0.0033	11.18
	No Thermal Break	36.4	0.0014	7.08
GFRP	Thermal Break	65.3	0.0049	8.77
	No Thermal Break	69.4	0.0023	9.63

5 Conclusions & Recommendations

Thermal and structural testing were conducted on representative sample sizes of reinforced concrete balcony slabs with and without thermal break to investigate the thermal insulation and ultimate strength capacity of the systems. Three variations of reinforcement type were examined, including GFRP reinforcement, steel reinforcement, and stainless steel reinforcement. Although multiple manufacturers currently provide balcony thermal break products reinforced with stainless steel, GFRP reinforcement presents an alternative solution for developing an efficient thermal break due to its low thermal conductivity in comparison to stainless steel. The following conclusions and recommendations summarize the results of the experimental program and provide recommendations for future research pertaining to the project.

5.1 Conclusions

Thermal experimental testing was performed to simulate the conditions of a reinforced concrete balcony slab in service conditions, exposed to an interior temperature of 21˚C and an exterior temperature of -31˚C. The temperature profiles obtained from thermal experimental testing demonstrated the efficiency of the thermal break in separating the two thermal environments. When used in conjunction with GFRP reinforcement, providing the lowest thermal conductivity of the three reinforcement types, the performance of the thermal break in terms of increasing the interior floor slab temperature was improved. The GFRP reinforced thermal break effectively increased the temperatures adjacent to the thermal break on the warm side by an average of 13.7˚C. This will consequentially increase the thermal comfort for inhabitants and reduce the potential for surface condensation and mould growth.

The thermal models developed using Heat3 were in agreement with experimental thermal results and were used to draw further conclusions of the system. The models were developed using a refined numerical

mesh in order to provide increased accuracy in the calculated temperature locations. The numerical models were found to accurately predict the thermal behaviour of the test samples under the experimental conditions, with individual temperature points varying on average by only 1.5˚C, and were therefore used to draw further conclusions regarding the performance of the systems. The models showed that the GFRP reinforced thermal break performed the best in terms of reducing heat flow across the thermal break. When compared to the conventionally built reinforced concrete balcony slab, represented by the samples containing steel reinforcement without a thermal break, the heat flow across the thermal break was reduced by 30.5%, 50%, and 62.5% for thermal breaks reinforced with carbon steel, stainless steel, and GFRP respectively. These results showed that the GFRP reinforced balcony thermal break outperforms the stainless steel reinforced thermal break in terms of thermal performance. The additional 12.5% reduction in heat flow obtained from replacing stainless steel with GFRP reinforcement will provide a substantial reduction in the total heat loss for a building.

Structural experimental testing was performed in order to verify the ultimate load carrying capacity and serviceability performance of the balcony thermal break systems. The test samples were monotonically loaded as cantilevers to reproduce the load on a balcony in service conditions, and were tested until ultimate failure. Each test specimen was instrumented with strain gauges to record the strain of the internal reinforcing bars, an LVDT to record deflection at the cantilevered tip of the specimen, and PI gauges to record strain at the thermal break. The experimentally obtained failure loads (for GFRP reinforced samples) and yielding loads (for carbon and stainless steel reinforced samples) for samples containing a thermal break were found to be 33.9%, 4.1%, and 7.3% higher than the calculated strengths for GFRP, carbon steel, and stainless steel reinforced samples, respectively. This indicates that the methods used to calculate the ultimate strength capacity of the thermal break system for each reinforcement type provided a conservative approach.

The GFRP reinforced samples both with and without a thermal break experienced shear failure within the reinforced concrete slab. This is a positive outcome, given that the sample containing a thermal break did not experience failure at the thermal break but instead performed as a GFRP reinforced concrete slab would without the thermal break. The steel and stainless steel reinforced sections containing a thermal break both experienced yielding of the reinforcement at the location of the thermal break prior to failure in the concrete.

Upon visual inspection during structural testing, a separation between the thermal break material and the concrete of the test specimens had developed along the top half of the samples due to the lack of bond between the thermal break material and the concrete. The width of this opening increased significantly after yielding of the steel and stainless steel reinforcement. The rotation at the balcony connection was found to approximately double with the introduction of the thermal break, but is significantly variable from sample to sample with a standard deviation equal to 38% of the observed rotation on average.

The GFRP reinforced thermal break performed optimally in terms of deflection requirements at service conditions in comparison to the steel and stainless steel reinforced thermal breaks. The samples containing a thermal break deflected on average 11% and 58% more than those without a thermal break for samples reinforced with steel and stainless steel, respectively. The samples containing GFRP reinforcement however deflected 9% less for samples containing a thermal break when compared to those without when evaluated at the service load condition.

5.2 Lessons Learned

Provided that the results of this experimental program will be built upon in future work, it is important to discuss the lessons learnt throughout the experimental program to provide guidance in improving the program. The majority of the lessons learnt relate to experimental set ups and instrumentation. One area

that could be greatly improved upon is the installation of thermal sensors within the concrete. Given the nature of casting concrete, it is important to adequately protect these sensors within the formwork such that fewer sensors are damaged. I would recommend applying a protective coating, such as a coating of hot glue or heat shrink wrap, over the sensors to provide additional protection. It is important that the selected protection is not bulky such that it won't interfere with the thermal properties of the system.

The most significant lesson learnt throughout the project is the importance of communication. Given the collaborative work between different organizations required to execute this project, a high level of communication is required at all stages. Maintaining constant and clear communication between all parties will improve the efficiency of the project, and will prevent unnecessary delays or errors from occurring.

5.3 Recommendations

Based on the results of the experimental program, the GFRP reinforced thermal break provides the best performance in terms of reducing heat transfer across the balcony to building interface, while providing sufficient structural performance in terms of ultimate load capacity. It is therefore recommended that the development of a GFRP reinforced balcony thermal break system continue to be investigated in order to produce a product that may be readily adopted by industry.

Further research is recommended to refine the reinforcement layout in order to determine the design which provides an optimal balance between the thermal and structural performance. In terms of thermal performance, the benefit provided by the GFRP reinforced thermal break is significant. It may therefore be reasonable to increase the reinforcement ratio in order to benefit the structural performance of the system, at a loss to the thermal performance. However the goal in developing the thermal break system should remain to optimize the thermal performance while providing sufficient structural performance in terms of ultimate load capacity and serviceability requirements.

Further research is recommended to evaluate the serviceability performance of the GFRP reinforced thermal break. It is recommended that the rotation of the thermal break be of focus in order to determine a method to predict and evaluate the rotation at this location. It is highly recommended that the separation between the concrete and thermal break interface be addressed. The width of this separation may possibly be reduced by methods such as increasing the reinforcement ratio, decreasing the reinforcement bar size but maintaining the same reinforcement ratio, or by alternative methods such as applying an adhesive between the two materials or installing near surface mounted reinforcement. The performance of these methods must be experimentally verified before they are suggested as a practical solution to reducing the separation between concrete and thermal break.

To conclude, the GFRP reinforced thermal break system should be further investigated and developed into an industry adoptable product as it provides the optimal solution for reducing thermal bridging across reinforced concrete balcony slabs, providing the ideal product to improve the energy efficiency of building envelopes and lead the industry towards a greener future.

References

[1] "LEED," U.S. Green Building Council, 2018. [Online]. Available: https://new.usgbc.org/leed. [Accessed 20 June 2018].

[2] "National Energy Code of Canada for Buildings 2017," National Research Council Canada, 2017. [Online]. Available: https://www.nrc-cnrc.gc.ca/eng/publications/codes_centre/2017_national_energy_code_buildings.html. [Accessed 2 June 2018].

[3] R. Park and T. Paulay, Reinforced Concrete Structures (https://books.google.ca/books?hl=en&lr=&id=QPDvchXv5zUC&oi=fnd&pg=PA1&dq=reinforced+concrete&ots=__RT8fs0fA&sig=NVQtfVWFgT52kb9buXcNmE7BpQM#v=onepage&q&f=false), Canada: John Wiley & Sons, Inc. , 1975.

[4] "Natural Resources Canada, Energy Use Data Handbook," [Online]. Available: http://oee.nrcan.gc.ca/publications/statistics/handbook2010/handbook2013.pdf. [Accessed 6 June 2017].

[5] "The Importance of Slab Edge & Balcony Thermal Bridges Report # 1: Impact of Slab Thermal Breaks on Effective R-Values and Energy Code Compliance," RDH Building Engineering Ltd., 2013.

[6] G. Hua, V. R. McClung and S. Zhang, "Impact of balcony thermal bridges on the overall thermal performance of multi-unit residential buildings: A case study," *Energy and Buildings 60,* pp. 163-173, 2013.

[7] O. C. G. Adan and R. A. Samson, Fundamentals of mold growth in indoor environments and strategies for healthy living, The Netherlands : Wageningen Academic Publishers, 2011.

[8] *ISO 10456 - Building materials and products - Hygrothermal properties,* Geneva: International Organization for Standardization , 2007.

[9] S. Bagherpour, "Fibre Reinforced Polyester Composites," In Tech, Najafabad.

[10] P. K. Mallick, Fiber Reinforced Composites, Materials, Manufacturing, and Design, New York: Marcell Dekker Inc. , 1988.

[11] W. T. Freeman and G. C. Kuebeler, "Mechanical and Physical Properties of Advanced Composites," ASTM International, 1974.

[12] R. C. Wetherhold and J. Wang, "Difficulties in the theories for predicting transverse thermal conductivity of continuous fiber composites," *Journal of Composite Materials,* vol. 28, pp. 1491-1498, 1994.

[13] H. Zhang, Building materials in civil engineering, Beijing: Woodhead Publishing, 2011.

[14] A. Nanni, "North American design guidelines for concrete reinforcement and strengthening using FRP: principles, applications and unresolved issues," Elsevier, Rolla.

[15] A. Nanni, A. De Luca and H. J. Zadeh, Reinforced Concrete with FRP Bars: Mechanics and Design, CRC Press, 2014.

[16] M. S. Al-Homoud, "Performance characteristics and practical applications of common building thermal insulation materials," *Building and Environment,* vol. 40, pp. 353-366, 2005.

[17] "STYROFOAM™ HIGHLOAD 40, 60 and 100 Extruded Polystyrene Insulation," Dow, Midland.

[18] "Thermal Break Material Armatherm 500," Armadillo Structural Connections, New Bedford.

[19] "Mightylite™ Structural Insulation Panels-Calcium Silicate Insulation," Refractory Specialties Inc., 2017. [Online]. Available: https://www.rsifibre.com/products/mightylite-structural-insulation-panels-calcium-silicate-insulation/. [Accessed 10 August 2017].

[20] "Redwood Plastics PVC & CPVC," 2017. [Online]. Available: https://www.redwoodplastics.com/products/pvc-cpvc/. [Accessed 10 August 2017].

[21] "UL 94 Flame Classifications," Professional Plastics, 2017. [Online]. Available: http://www.professionalplastics.com/UL94FlameClassificationsForPlastics?gclid=CjwKEAjwiLDMBRDF586Bwe2Sq3ISJAAjZol_WWeMTxL1Obu7f5ZCwvxIXAXRFYsKnoTAzMVnVW3vDRoC2LPw_wcB. [Accessed 10 August 2017].

[22] "Thermal Break Material Armatherm Grade FRR," Armadillo Structural Connections, New Bedford.

[23] RDH Building Engineering Ltd., "The Importance of Slab Edge & Balcony Thermal Bridges Report # 1: Impact of Slab Thermal Breaks on Effective R-Values and Energy Code Compliance," 2013. [Online]. Available: https://rdh.com/wp-content/uploads/2014/07/Part-1-The-Importance-of-Slab-Edge-Balcony-Thermal-Bridges.pdf. [Accessed 25 January 2018].

[24] RDH Buiding Engineering Ltd., "The Importance of Slab Edge & Balcony Thermal Bridges Report # 4: Thermal Modeling Considerations for Balconies and Various Thermal Break Strategies," 2013. [Online]. Available: https://rdh.com/wp-content/uploads/2014/07/Part-4-Other-Considerations.pdf. [Accessed 26 January 2018].

[25] Schöck, "Thermal Bridge Solutions. Schöck Isokorb Product Guide," Schöck, Kitchener, 2017.

[26] T. Keller, F. Riebel and A. Zhou, "Multifunctional Hybrid GFRP/Steel Joint for Concrete Slab Structures," *Journal of Composites for Construction ,* vol. 10, no. 6, pp. 550-560, 2006.

[27] K. GouLouti, J. de Castro, A. P. Vassilopoulos and T. Keller, "Thermal performance evaluation of fiber-reinforced polymer thermal breaks for balcony connections," Elsevier, Lausanne, 2013.

[28] Schock, "Design Guide Solutions to Prevent Thermal Bridging," Schock , Baden-Baden, 2014.

[29] Ancon, "Thermally Insulated Balcony Connectors for the Construction Industry," Ancon, Sheffield, 2015.

[30] "Halfen HIT - Insulated Balcony Connection Technical Product Information," Halfen, Converse, 2013.

[31] H-Bau, "Thermal insulation elements DIN EN 1992-1-1," H-Bau, 1992.

[32] Concrete Design Handbook, Third Edition, Ottawa: Cement Association of Canada, 2010.

[33] CSA Standard S806-12 Design and construction of building structures with fiber-reinforced polymers, Mississauga: Canadian Standards Association , 2012.

[34] "Reinforcing Concrete Structures with Fibre Reinforced Polymers," ISIS Canada Research Network, Winnipeg , 2007.

[35] National Building Code of Canada Volume 2, Ottawa: Canadian Commission on Building and Fire Codes, National Research Council of Canada, 2010.

[36] C. E. Reynolds, J. C. Steedman and A. J. Threlfall, Reinforced Concrete Designer's Handbook, Eleventh Edition, New York : Taylor & Francis , 2007.

[37] G. F. G. M. Division, "Approximate Weight of Architectural Flat Glass," Glass Association of North America , Topeka.

[38] S16-09 Design of Steel Structures, Mississauga: Canadian Standards Association, 2009.

[39] f. i. d. beton, "FRP Reinforcement in RC Structures, fib Bulleting 40," International Federation for Structural Concrete, Lausanne, 2007.

[40] "Fiberglass Rebar," TUF-BAR, 2017. [Online]. Available: https://www.tuf-bar.com/products/tuf-bar/. [Accessed 4 January 2017].

[41] "GFRP Specification Guide," V-ROD Canada, 2017. [Online]. Available: http://www.vrodcanada.com/product-data/gfrp-specification-guide. [Accessed 4 January 2017].

[42] B. Steeve and R. Wingate, "Aerospace Threaded Fastener Strength in Combined Shear and Tension Loading," National Aeronautics and Space Administration, Huntsville, Alabama, 2012.

[43] S. S. Kumar and A. S. Kumar, "Combined Shear and Tension Failure," Indian Institute of Technology Madras, Chennai, India.

[44] S. Grieff, Interviewee, *Professional Engineer.* [Interview]. 28 January 2017.

[45] ASTM International, "ASTM A370 Standard Test Methods and Definitions for Mechanical Testing of Steel Products," ASTM International , West Conshohocken, 2003.

[46] ASTM International, "ASTM C39 Standard Test Method for Compressive Strength of Cylindrical Concrete Specimens," ASTM International , West Conshohocken, 2014.

[47] *ISO 10211 Thermal bridges in building construction - Heat flows and surface temperatures - Detailed calculations,* Geneva: International Organization for Standardization, 2007.

[48] D. T. Blomberg, "HEAT3 A PC-program for heat transfer in three dimensions," 28 September 2001. [Online]. Available: https://www.buildingphysics.com/manuals/HEAT3_4.pdf. [Accessed 19 August 2018].

[49] J. Tejchman and J. Bobinski, Continuous and Discontinuous Modelling of Fracture in Concrete Using FEM, Berlin: Springer, 2013.

[50] "Difference between Stainless Steel and Mild Steel," Pearlite Steel, 2015. [Online]. Available: http://pearlitesteel.com/difference-between-stainless-steel-and-mild-steel/. [Accessed 3 August 2017].

[51] "Comparison of structural design in stainless steel and carbon steel," British Stainless Steel Association, 2017. [Online]. Available: http://www.bssa.org.uk/topics.php?article=125. [Accessed 3 August 2017].

Appendix

A.1 Full-Scale Balcony Ultimate Strength Design - GFRP Reinforcement

Reinforcement Data

VRod GFRP #8 Bars

f_u = 1000 MPa

E_f = 66.4 GPa

ε_{fu} = 0.0151

A_b = 506.7 mm^2

d_b = 25 mm

$f_{u,comp} = 0.6\ f_u$ = 600 MPa

$E_{f,comp} = 0.8\ E_f$ = 53.12 GPa

$\varepsilon_{fu,comp}$ = 0.0106

Thermal Break Moment Capacity Design

Moment arm between A_f and A_f'

$d = h - 2\ c_c - d_b$

d = 85 mm

Moment resistance $M_r = T_f\ d = C_f\ d$

$T_f = f_{u,comp}\ A_f$

$C_f = f_{u,comp}\ A_f'$

$M_r = M_f$ = 38.2 kN-m

Solving for minimum required A_f and A_f'

$A_f = A_f' = M_f / f_{u,comp}\ d$ = (38.2 kN-m) (10^6) / (600 MPa) (85 mm) = 749 mm^2

Selected Bar Spacing

Selected spacing is based on results from deflection calculations (see Appendix Z).

s = 250 mm

A_f = (500 mm^2) (1000 mm) / 250 mm = 2000 mm^2

Moment resistance of the connection

$M_r = f_{u,comp}\ A_f\ d$ = (600 MPa) (2000 mm^2) (85 mm) (10^{-6}) = 102 kN-m

Thermal Break Shear Capacity Check

Shear Capacity

The shear strength of frp, f_v, is assumed to be $0.1\ f_{u,comp}$ = 0.1 (600) = 60 MPa

$V_r = f_v\ A_f$ = (60 MPa) (2000 mm^2) = 120 kN

Factored shear force applied to upper row of rebar = V_f / 2 = 19.1 kN

V_f / V_r = 19.1 kN / 120 kN = 0.16

Tensile Capacity

$T_r = f_{u,comp}\ A_f$ = (600 MPa) (2000 mm^2) = 1200 kN

$T_f = M_f / d$ = (38.2 kN-m) / (85 mm) = 449 kN

T_f / T_r = 449 kN / 1200 kN = 0.37

Interaction Equation

$(V_f / V_r)^2 + (T_f / T_r)^2 \leq 1.0$

$(0.16)^2 + (0.37)^2 = 0.163 \leq 1.0$

Reinforced Concrete Slab Design (S806-12)

Check Minimum Slab Reinforcement

$A_{fmin1} = 400 (A_g / E_f) = (400) (1000 \text{ mm}) (190 \text{ mm}) / (66{,}400 \text{ MPa}) = 1145 \text{ mm}^2 / \text{m}$

$d = h - c_c - d_b/2 = 137.5 \text{ mm}$

$A_{fmin2} = M_f / f_u j\, d = (38.2 \text{ kN-m}) (10^6) / (1000 \text{ MPa}) (0.85) (137.5 \text{ mm}) = 327 \text{ mm}^2$

Check shear capacity of the section

$V_c = 0.05 \lambda k_m k_r f'^{1/3}_c b_w d_v$ with $V_c > 0.11 f'^{1/2}_c b_w d_v$

$\lambda = 1.0$

$d_v > 0.9 d = 124$ or $0.72 h = 137$

$k_m = (V_f d / M_f)^{1/2} = [(38.2) (10^3) (137.5) / (38.2) (10^6)]^{1/2} = 0.37$

$\rho_{fw} = A_f / b d = 0.015$

$k_r = 1 + (E_f \rho_{fw})^{1/3} = 10.99$

$V_c = (0.05) (0.37) (10.99) (30)^{1/3} (1000) (137) (10^{-3}) = 86.5 \text{ kN}$

$V_c > 0.11 (30)^{1/2} (1000) (137) (10^{-3}) = 82.5 \text{ kN}$

$V_c = 86.5 \text{ kN} > V_f = 38.2 \text{ kN}$ ∴ the section is adequate for shear

Check moment resistance of the section

$A_{frp} = 500 \text{ mm}^2 (1000)/ 250 = 2000 \text{ mm}^2$

$d = h - c_c - d_b/2 = 137.5 \text{ mm}$

$\rho_{fb} = \alpha_1 \beta_1 (f'_c / f_u) (\varepsilon_{cu} / \varepsilon_{cu} + \varepsilon_{frpu}) = (0.8) (0.9) (30 / 1000) (0.0035 / 0.0035 + 0.0151) = 0.0041$

$\rho_f = (2000) / (1000) (137.5) = 0.0145 > \rho_{fb}$

The section will fail by concrete rupture.

$f_{frp} = 0.5 E_{frp} \varepsilon_{cu} [(1 + 4 \alpha_1 \beta_1 f'_c / \rho_{frp} E_{frp} \varepsilon_{cu})^{1/2} -1]$

$f_{frp} = (0.5)(66{,}400 \text{ MPa})(0.0035) [(1 + (4)(0.9)(0.8)(30 \text{ MPa})/(0.015)(66{,}400 \text{ MPa})(0.0035))^{1/2} -1]$

$= 474 \text{ MPa}$

$a = A_{frp} f_{frp} / \alpha_1 f'_c b = (2000 \text{ mm}^2) (474 \text{ MPa}) / (0.8) (30) (1000 \text{ mm}) = 39.5 \text{ mm}$

$M_r = A_{frp} f_{frp} (d - a/2) = (2000 \text{ mm}^2) (474 \text{ MPa}) (137.5 \text{ mm} - 39.5 \text{ mm} /2) (10^{-6}) = 111.6 \text{ kN-m}$

$M_{cr} = f_r I_g / y_t$

$f_r = 0.6 f'^{1/2}_c = (0.6) (30 \text{ MPa})^{1/2} = 3.29 \text{ MPa}$

$M_{cr} = (3.29 \text{ MPa}) (1000 \text{ mm})(190 \text{ mm})^3 / (12) (190 \text{ mm} /2) (10^{-6}) = 19.8 \text{ kN-m}$

$M_r = 111.6 \text{ kN-m} > M_f = 38.2 \text{ kN-m}$ and $M_r = 111.6 \text{ kN-m} > 2 M_{cr} = 40 \text{ kN-m}$

Development Lengths

Clause 9.6.3

Embedment length = l_d + d or l_d + $12d_b$

d = 137.5 mm

$12d_b$ = 300 mm

Tension

$l_d = 1.15\ k_1\ k_2\ k_3\ k_4\ k_5\ f_f\ A_b\ /\ f'_c{}^{0.5}\ d_{cs}$

k_1 = 1.0

k_2 = 1.0 normal density concrete

k_3 = 1.0 for $A_b > 300\ mm^2$

k_4 = 1.0 CFRP

k_5 = 1.0 surface treatment

$d_{cs} = 52.5 < 2.5\ d_b = 62.5$ mm

$f'_c{}^{0.5} < 5$

Using f_f = 474 MPa

$l_d = (1.15)\ (1.0)\ (474\ MPa)\ (500\ mm^2)\ /\ (5)\ (52.5\ mm) = 1038$ mm

Factored by $A_{f,required}\ /\ A_{f,provided} = 749\ /\ 2000 = 0.3745$

$l_d = (0.3745)\ (1038\ mm) = 389$ mm

Total Embedment length = 389 + 300 = 689 mm

Transverse Reinforcement

Transverse reinforcement will be placed at 250 mm on center throughout the entire slab.

Beam Deflection

Calculated deflections are for the reinforced concrete slab only and neglect the influence of the thermal break.

$M_{cr} = f_r\ I_g\ /\ y_t$

$f_r = 0.6\ f'_c{}^{1/2} = 3.29$

$I_g = (1000)\ (190)^3\ /\ 12 = 5.72 \times 10^8$

y_t = 95 mm

$M_{cr} = (3.29)\ (5.72)\ (10^8)\ /\ (95)\ (10^6) = 19.8$ kN-m < M_s = 30.1 kN-m ∴ section is cracked

Entire beam length - #8 @ 250 mm o.c. ISIS Design Manual for Deflection Equations

$n = E_f\ /\ E_c = (46000)\ /\ (4500)\ (30)^{1/2} = 1.87$

$d = h - c_c - d_b/2 = 137.5$ mm

$\rho_f = (2000\ mm^2)\ /\ (1000\ mm)\ (137.5\ mm) = 0.015$

$k = [(\rho n)^2 + (2\rho n)]^{1/2} - \rho n = [(0.015)^2(1.87)^2 + (2)(0.015)(1.87)]^{1/2} - (0.015)(1.87) = 0.21$

kd = 28.9

$I_{cr} = (1/3)\ (1000)\ (28.9)^3 + (1.87)\ (2000)\ (137.5 - 28.9)^2 = 5.22 \times 10^7\ mm^4$

Deflection due to point load $\Delta_p = \frac{PL^3}{3EI_{cr}}\left[1 - \eta\left(\frac{L_g}{L}\right)^3\right]$

Deflection due to distributed load $\Delta_w = \frac{wL^4}{8EI_{cr}}\left[1 - \eta\left(\frac{L_g}{L}\right)^4\right]$

$\eta = 1 - I_{cr}/I_g = 0.9$

L = 1830 mm, L_g = 1464 mm from cantilever end to M_{cr}

$E_c = 4500\ f'_c{}^{1/2} = 24648$

$P_s = 1.02 + 1.5 = 2.52$ kN

$w_s = 8.7 + 4.8 + 1.72 = 15.22$ kN/m

$\Delta_p = [(2.52)\ (10^3)\ (1830)^3 / (3)\ (24648)\ (5.22)\ (10^7)]\ [1 - 0.9\ (1464/1830)^3] = 2.16$mm

$\Delta_w = [(15.22)\ (1830)^4 / (8)\ (24648)\ (5.22)\ (10^7)]\ [1 - 0.9\ (1464/1830)^4] = 10.47$ mm

$\Delta_{total} = 12.63$ mm > $\Delta_{allow} = 5$ mm ∴ precamber will be required at selected spacing

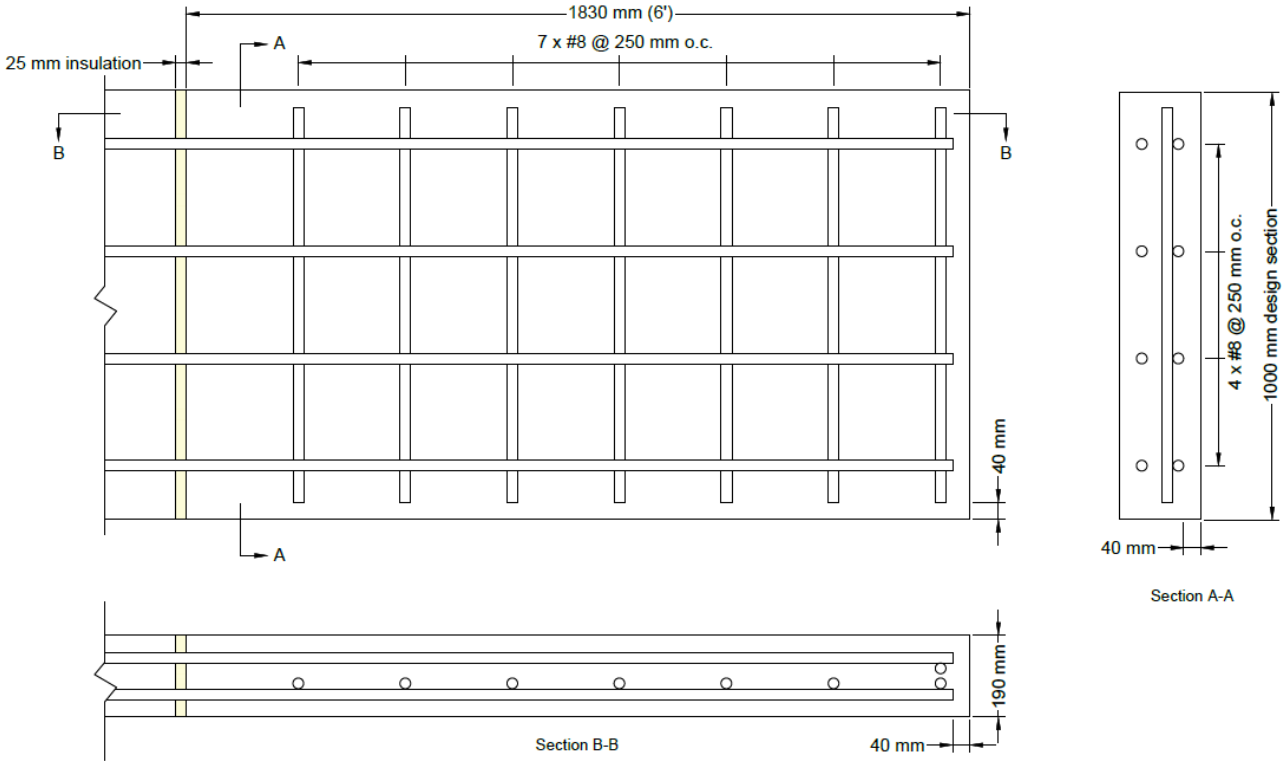

A.2 Full-Scale Balcony Ultimate Strength Design - Steel Reinforcement

Reinforcement Data

15M Steel Bars

f_y = 4 00 MPa

E_s = 200 GPa

A_b = 200 mm^2

d_b = 16 mm

Thermal Break Moment Capacity Design

Moment arm between A_s and A_s'

$d = h - 2\ c_c - d_b$

d = 94 mm

Moment resistance $M_r = T_s\ d = C_s\ d$

$T_s = f_y\ A_s$

$C_s = f_y\ A_s'$

$M_r = M_f$ = 38.2 kN-m

Solving for minimum required A_s and A_s'

$A_{ss} = A_{ss}' = M_f / f_y\ d$ = (38.2 kN-m) (10^6) / (400 MPa) (94 mm) = 1016 mm^2

Selected Bar Spacing

s = 167 mm

A_s = (200 mm^2) (1000 mm) / 167 mm = 1200 mm^2

Moment resistance of the connection

$M_r = f_y\ A_s\ d$ = (400 MPa) (1200 mm^2) (94 mm) (10^{-6}) = 45.1 kN-m

Thermal Break Shear Capacity Check

Shear Capacity

$V_r = 0.66\ f_y A_s$ = 0.66 (400 MPa) (1200 mm^2) = 316.8 kN

Factored shear force applied to upper row of rebar = V_f / 2 = 19.1 kN

V_f / V_r = 19.1 kN/ 316.8 kN = 0.06

Tensile Capacity

$T_r = f_y\ A_s$ = (400 MPa) (1200 mm^2) = 480 kN

$T_f = M_f / d$ = (38.2 kN-m) / (94 mm) = 406 kN

T_f / T_r = 406 kN / 480 kN = 0.85

Interaction Equation

$(V_f / V_r)^2 + (T_f / T_r)^2 \leq 1.0$

$(0.06)^2 + (0.85)^2 = 0.73 \leq 1.0$

Reinforced Concrete Slab Design (CSA A23.3) - Section 1

Check Minimum Slab Reinforcement

$A_{smin} = 0.002\ A_g$ = 0.002(1000mm) (190mm) = 380 mm^2 / m

Moment resistance of the section

A_s = (200 mm^2) (1000 mm)/ (167 mm) = 1200 mm^2

$a = f_y A_s / \alpha_1 f'_c b$ = (400 MPa) (1200 mm^2) / (0.8) (30 MPa) (1000 mm) = 20 mm

$d = h - c_c - d_b/2$ = 190 mm – 40 mm – 16 mm/2 = 142 mm

$M_r = f_y A_s (d - a/2)$ = (400 MPa) (1200 mm^2) (144 mm – 17.2 mm/2) (10^{-6}) = 65 kN-m

Check shear capacity of the section

$V_c = \lambda \beta f'^{1/2}_c b_w d_v$

d = 190 – 40 – 16/2 = 142 mm

$d_v > 0.9 d$ = 127.8 or 0.72 h = 136.8

b_w = 1000 mm

λ = 1

β = 0.21 (clause 11.3.6.2)

V_c = (0.21) (30 MPa)$^{1/2}$ (1000 mm) (136.8 mm) (10^{-3}) = 157 kN

V_c = 157 kN > V_f = 38.2 ∴ kN the section is adequate for shear

Slab Design at Cantilevered End - Section 2

Design with Minimum Slab Reinforcement and Check Capacity

$A_{smin} = 0.002 A_g$ = 0.002(1000mm) (190mm) = 380 mm^2 / m

Select 15M at 500 mm o.c.

A_s = (200 mm^2) (1000 mm)/ (500 mm) = 400 mm^2

Moment resistance of the section

$a = f_y A_s / \alpha_1 f'_c b$ = (400 MPa) (400 mm^2) / (0.8) (30 MPa) (1000 mm) = 6.7 mm

$d = h - c_c - d_b/2$ = 190 – 40 – 16/2 = 142 mm

$M_r = f_y A_s (d - a/2)$ = (400 MPa) (400 mm^2) (144 mm – 6.7 mm/2) (10^{-6}) = 22.5 kN-m

Reinforcement Summary

15M @ 500 mm o.c. top and bottom for M_r = 22.5 kN-m

Development Lengths

Clause 12.10.4

Embedment length = $l_d + d$ or $l_d + 12d_b$

d = 142 mm

$12d_b$ = 192 mm

Development length required in tension

$l_d = 0.45 k_1 k_2 k_3 k_4 f_y d_b f'^{-0.5}_c$

k_1 = 1.0

k_2 = 1.0 uncoated bars

k_3 = 1.0 normal density concrete

k_4 = 0.8 bar size

l_d = (0.45) (0.8) (400 MPa) (16 mm) (30 MPa)$^{-0.5}$ = 421mm

Embedment length = 421 mm + 192 mm = 613 mm (620 mm)

Development length required in compression

$l_{db} = 0.24\ d_b\ f_y\ f'_c{}^{-0.5}$ = (0.24) (16 mm) (400 MPa) (30 MPa)$^{-0.5}$ = 280 mm

Embedment length = 280 mm + 192 mm = 472 mm (480 mm)

Transverse Reinforcement

Transverse reinforcement will be placed at 500 mm on center throughout the entire slab.

Reinforcement Summary

Connection & Slab Section 1

15M at 167 (500/3) mm o.c. top and bottom

Embedment length of 620 mm provided into interior and exterior floor slabs.

Slab Section 2

15M at 500 mm o.c. top and bottom

M_f = 22.19 kN-m at 480 mm from connection

Beam Deflection

Calculated deflections are for the reinforced concrete slab only and neglect the influence of the thermal break.

$M_{cr} = f_r\ I_g\ /\ y_t$

$f_r = 0.6\ f'_c{}^{1/2}$ = 3.29

I_g = (1000) (190)^3 / 12 = 5.72 x 10^8

y_t = 95 mm

M_{cr} = (3.29) (5.72) (10^8) / (95) (10^6) = 19.8 kN-m

15 M @ 125 mm o.c.

M_s = 30.1 kN-m > M_{cr} ∴ section is cracked

$n = E_s / E_c$ = 8.11

$B = b / n\ A_s$ = 1000 / (8.11) (1032) = 0.119

$d = h - c_c - d_b/2$ = 144 mm

$kd = [(2\ d\ B + 1)^{1/2} - 1] / B$ = 41.5 mm

$I_{cr} = b\ (kd)^3/ 3 + n\ A_s\ (d - kd)^2$ = (1/3) (1000) (41.5)^3 + (8.11) (1032) (144 – 41.5)^2 = 1.12 x 10^8 mm^4

M_{cr} / M_a = 0.66

$I_e = (M_{cr}/M_a)^3\ I_g + [1 - (M_{cr}/M_a)^3]\ I_{cr}$ = (0.66)^3 (5.72) (10^8) + (1 – 0.66^3) (1.12) (10^8) = 2.44 x 10^8

$\Delta_p = Pl^3/3EI$ = (2.52)(10^3)(1830^3)/(3)(24648)(2.44x 10^8) = 0.86 mm

$\Delta_w = wl^4/8EI = (15.22)(1830^4)/(8)(24648)(2.44 \times 10^8) = 3.55$ mm

$\Delta_{total} = 4.41$ mm > <$\Delta_{allow} = 5$ mm

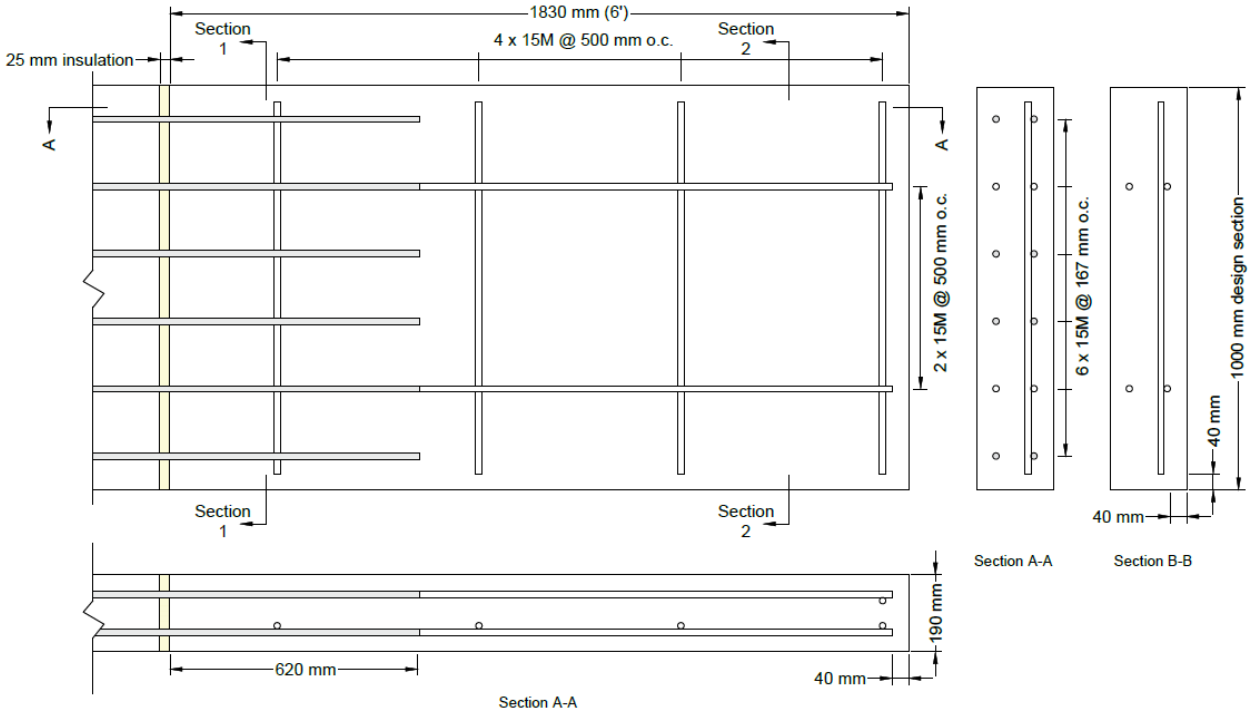

A.3 Full-Scale Balcony Ultimate Strength Design - Stainless Steel Reinforcement

Reinforcement

Number 5 Stainless Steel Bars - Provided by Salit Steel

f_y = 518 MPa

E_s = 200 GPa

A_b = 200 mm^2

d_b = 16 mm

Thermal Break Moment Capacity Design

Moment arm between A_{ss} and A_{ss}'

$d = h - 2\ c_c - d_b$

d = 94 mm

Moment resistance $M_r = T_{ss}\ d = C_{ss}\ d$

$T_{ss} = f_y\ A_{ss}$

$C_{ss} = f_y\ A_{ss}'$

$M_r = M_f$ = 38.2 kN-m

Solving for minimum required A_{ss} and A_{ss}'

$A_{ss} = A_{ss}' = M_f / f_y\ d$ = (38.2 kN-m) (10^6) / (518 MPa) (94 mm) = 784 mm^2

Selected Bar Spacing

s = 250 mm

A_{ss} = (200 mm^2) (1000 mm) / 250 mm = 800 mm^2

Moment resistance of the connection

$M_r = f_y\ A_{ss}\ d$ = (518 MPa) (800 mm^2) (94 mm) (10^{-6}) = 39.0 kN-m

Thermal Break Shear Capacity Check

Shear Capacity

$V_r = 0.66\ f_y A_{ss}$ = 0.66 (518 MPa) (800 mm^2) = 273.5 kN

Factored shear force applied to upper row of rebar = V_f / 2 = 19.1 kN

V_f / V_r = 19.1 kN / 273.5 kN = 0.07

Tensile Capacity

$T_r = f_y\ A_{ss}$ = (518 MPa) (800 mm^2) = 414 kN

$T_f = M_f / d$ = (38.2 kN-m) / (94 mm) = 406 kN

T_f / T_r = 406 kN / 414 kN = 0.98

Interaction Equation

$(V_f / V_r)^2 + (T_f / T_r)^2 \leq 1.0$

$(0.07)^2 + (0.98)^2 = 0.97 \leq 1.0$

Slab Capacity Adjacent to Connection (CSA A23.3) – Section 1

Check Minimum Slab Reinforcement

$A_{ss,min} = 0.002\ A_g = 0.002(1000mm)\ (190mm) = 380\ mm^2 / m$

Moment resistance of the section

$A_s = (200\ mm^2)\ (1000\ mm)/\ (250\ mm) = 800\ mm^2$

$a = f_y\ A_{ss} / \alpha_1\ f'_c\ b = (518\ MPa)\ (800\ mm^2) / (0.8)\ (30\ MPa)\ (1000\ mm) = 17.3\ mm$

$d = h - c_c - d_b/2 = 142\ mm$

$M_r = f_y\ A_{ss}\ (d - a/2) = (518\ MPa)\ (800\ mm^2)\ (142\ mm - 17.3\ mm/2)\ (10^{-6}) = 55.3\ kN\text{-}m$

Check shear capacity of the section

$V_c = \lambda\ \beta\ f'^{1/2}_c\ b_w\ d_v$

$d_v > 0.9\ d = 127.8\ mm$ or $0.72\ h = 136.8\ mm$

$b_w = 1000\ mm$

$\lambda = 1$

$$\beta = \frac{0.4}{1+1500\varepsilon_x} \cdot \frac{1300}{1000+s_{ze}}$$

$s_{ze} = 35\ s_z / 15 + a_g = (35)\ (136.8) / (15 + 20) = 136.8$

$$\varepsilon_x = \frac{\frac{M_f}{d_v}+V_f}{2E_sA_s} = [(38.2)\ (10^6) / (136.8) + (38.2)\ (10^3)] / [2\ (200{,}000)\ (400)] = 0.00198$$

$B = [0.4 / (1 + 1500\ (0.00198))] \cdot [1300 / (1000 + 136.8)] = 0.115$

$V_c = (0.115)\ (30)^{1/2}\ (1000\ mm)\ (136.8)\ (10^{-3}) = 86.2\ kN$

$V_c = 86.2\ kN > V_f = 38.2\ \therefore\ kN$ the section is adequate for shear

Slab at Cantilevered End – Section 2

Design with Minimum Reinforcement and Check Capacity

$A_{ss,min} = 0.002\ A_g = 0.002(1000mm)\ (190\ mm) = 380\ mm^2 / m$

Select #5 at s = 500 mm o.c.

$A_{ss} = 200\ mm^2\ (1000)/\ 500 = 400\ mm^2$

Check moment resistance of the section

$A_{ss} = (200\ mm^2)\ (1000\ mm)/\ (500\ mm) = 400\ mm^2$

$a = f_y\ A_{ss} / \alpha_1\ f'_c\ b = (518\ MPa)\ (400\ mm^2) / (0.8)\ (30\ MPa)\ (1000\ mm) = 8.63\ mm$

$d = h - c_c - d_b/2 = 142\ mm$

$M_r = f_y\ As_s\ (d - a/2) = (518\ MPa)\ (400\ mm^2)\ (142\ mm - 8.63mm/2)\ (10^{-6}) = 28.53\ kN\text{-}m$

Reinforcement Summary

#5 at 500 mm o.c. top and bottom for $M_r = 28.53\ kN\text{-}m$

$M_f = 28.53\ kN\text{-}m$ at 280 mm from connection

Development Lengths

Clause 12.10.4

Embedment length = l_d + d or $l_d + 12d_b$

d = 142 mm

$12d_b$ = 192 mm

Development length required in tension

$l_d = 0.45\ k_1\ k_2\ k_3\ k_4\ f_y\ d_b\ f'_c{}^{-0.5}$

k_1 = 1.0

k_2 = 1.0 uncoated bars

k_3 = 1.0 normal density concrete

k_4 = 0.8 #5 bars

$l_d = (0.45)\ (0.8)\ (518\ MPa)\ (16\ mm)\ (30\ MPa)^{-0.5}$ = 545 mm

Embedment length = 545 mm + 192 mm = 737 mm (740 mm)

Development length required in compression

$l_{db} = 0.24\ d_b\ f_y\ f'_c{}^{-0.5} = (0.24)\ (16\ mm)\ (518\ MPa)\ (30\ MPa)^{-0.5}$ = 363 mm

Embedment length = 363 mm + 192 mm = 455 mm (460 mm)

Reinforcement Summary

Thermal Break & Slab Section 1

#5 at 250 mm o.c. top and bottom

Embedment length of 740 mm provided into interior and exterior floor slabs

Slab Section 2

#5 at 500 mm o.c. top and bottom

Beam Deflection

Calculated deflections are for the reinforced concrete slab only and neglect the influence of the thermal break.

$M_{cr} = f_r\ I_g\ /\ y_t$

$f_r = 0.6\ f'_c{}^{1/2} = 3.29$

$I_g = (1000)\ (190)^3\ /\ 12 = 5.72 \times 10^8$

y_t = 95 mm

$M_{cr} = (3.29)\ (5.72)\ (10^8)\ /\ (95)\ (10^6)$ = 19.8 kN-m

Section 1 – #5 @ 500 mm o.c.

M_s = 15.7 kN-m < M_{cr} ∴ section is uncracked and I_g is used

$I_g = (1000)\ (190)^3\ /\ 12 = 5.72 \times 10^8$

Section 2 – 15M @ 167 mm o.c.

M_s = 30.1 kN-m > M_{cr} ∴ section is cracked

$n = E_s / E_c = 8.11$

$B = b / n A_s = 1000 / (8.11)(800) = 0.154$

$d = h - c_c - d_b/2 = 142$ mm

$kd = [(2 d B + 1)^{1/2} - 1] / B = 36.9$ mm

$I_{cr} = b (kd)^3/ 3 + n A_s (d - kd)^2 = (1/3)(1000)(36.9)^3 + (8.11)(800)(142 - 36.9)^2 = 8.84 \times 10^7$ mm^4

$M_{cr} / M_a = 0.66$

$I_e = (M_{cr}/M_a)^3 I_g + [1 - (M_{cr}/M_a)^3] I_{cr} = (0.66)^3 (5.72)(10^8) + (1 - 0.66^3)(8.84)(10^7) = 2.27 \times 10^8$

$\Delta_p = Pl^3/3EI = (2.52)(10^3)(1830^3)/(3)(24648)(2.27 \times 10^8) = 0.92$ mm

$\Delta_w = wl^4/8EI = (15.22)(1830^4)/(8)(24648)(2.27 \times 10^8) = 3.81$ mm

$\Delta_{total} = 4.73$ mm > <$\Delta_{allow} = 5$ mm

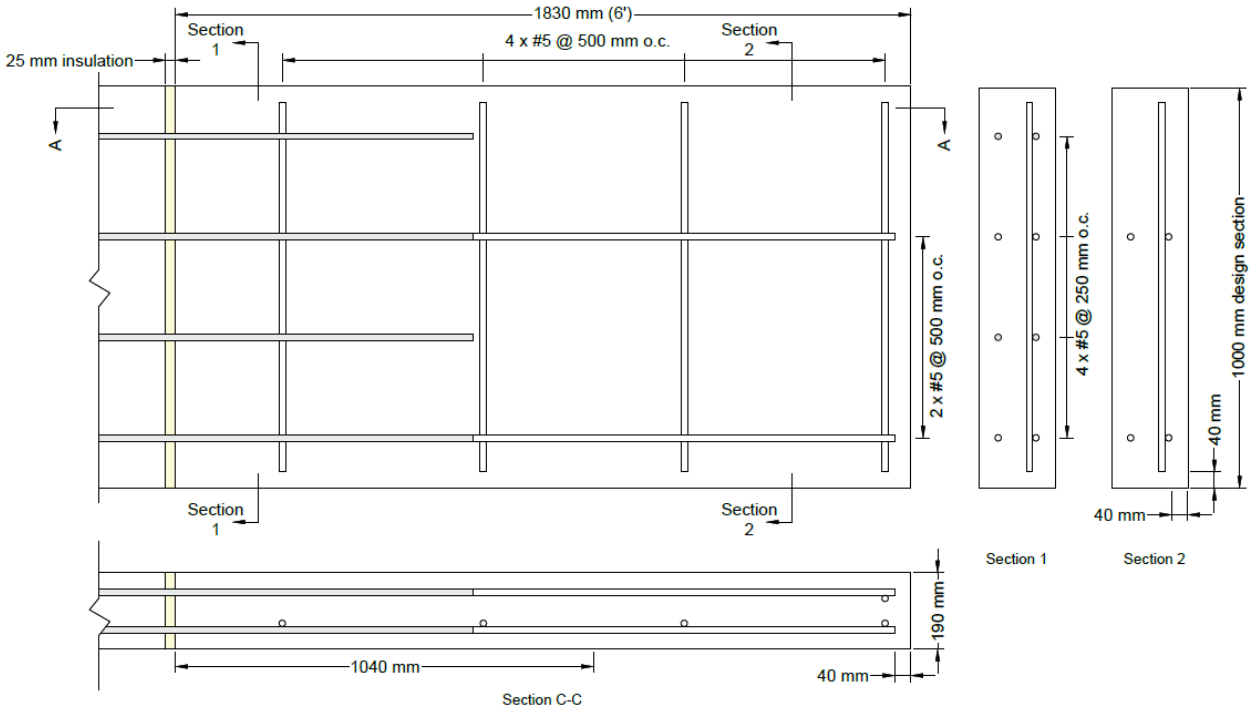

A.4 Load Takeoff for Structural Design

Distributed loads

Slab Self-Weight

Dimensions

l_n = 1830 mm (6 ft)

h = 190 mm

w = 1000 mm

Reinforced concrete density = 25 kN/m^3

w_d = (1.83) (0.19) (25) = 8.69 kN/m per m

Live Load

Specified in the 2010 NBCC

Exterior Balconies

w_{ll} = 4.8 kN/m per m

Snow Load

$w_{snow} = I_s [S_s (C_b C_w C_s C_a) + S_r]$

$I_s = C_w = C_s = C_a = 1.0$

C_b = 0.8

S_s = 1.9, S_r = 0.2 for Winnipeg

w_{snow} = (1.9) (0.8) + (0.2) = 1.72 kN/m

Factored Distributed Load

$w_f = 1.25\ w_d + 1.5\ w_{ll} + 0.5\ w_{snow}$

= 18.9 kN/m

Concentrated Loads

Balcony Railing Self-weight

h = 1070 mm from NBCC

¾" glass weight = 0.478 kN/m^2

Assume 2 panes for calculations

P_d = (2) (0.478) (1.070) = 1.02 kN

Case 1: Vertical Load on Guard

NBCC 4.1.5.14.4)

P_l = 1.5 kN per m acting vertically

Case 2: Horizontal Load on Guard

h = 1070 mm from NBCC

P_l = 1 kN acting horizontally at h

Factored Vertical Concentrated Load

$P_f = 1.25\ P_d + 1.5\ P_l$

= 1.275 kN Case 2

= 3.525 kN Case 1

Concentrated Moment

Horizontal Load on Guard

P_l = 1 kN acting horizontally at h

M_l = 1.07 kN-m

Factored Concentrated Moment

Case 1 only

$M_f = 1.5\ M_l$

= 1.605 kN-m

Shear Force and Bending Moment Diagrams

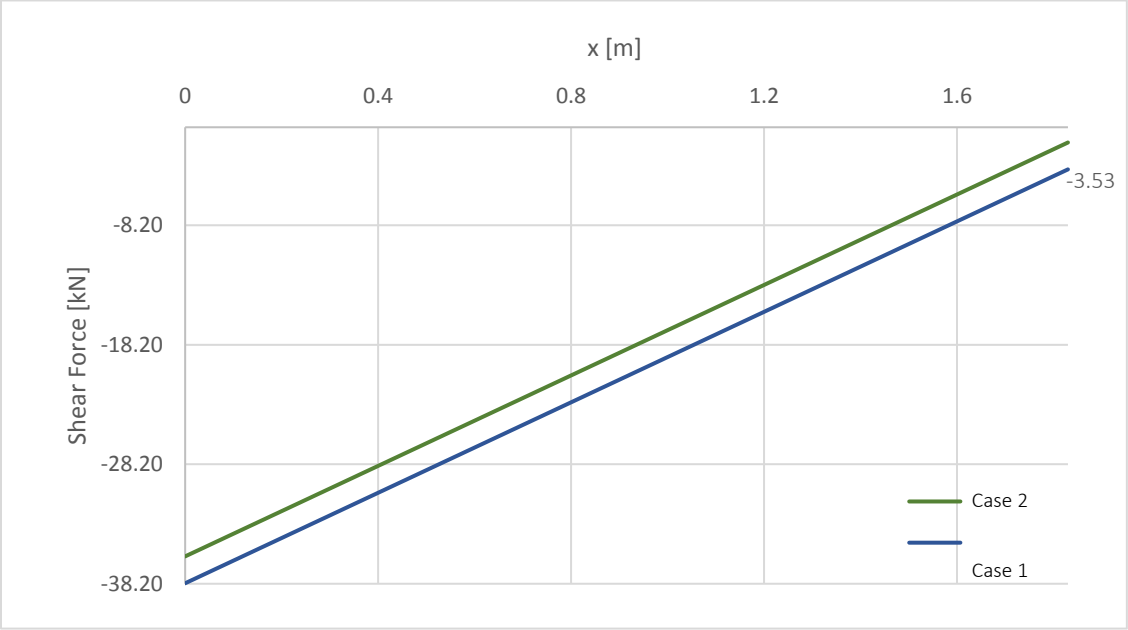

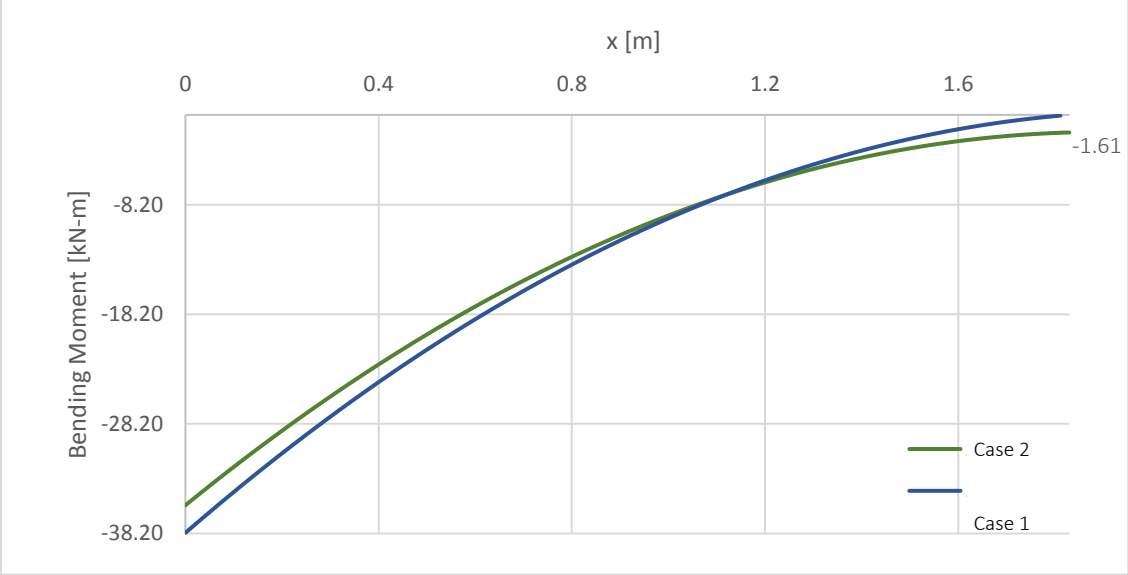

Connection Loads

Case 1 produces critical design loads at the thermal break connection.

M_f = 38.2 kN-m

V_f = 38.2 kN

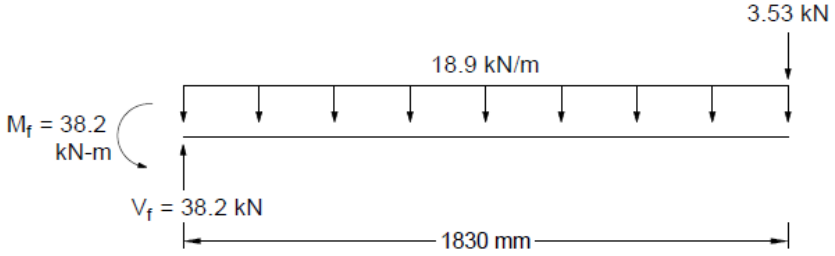

A.5 Rebar Tensile Testing

Carbon Steel

The yield point is calculated using the 0.2% offset method for carbon steel samples.

Carbon steel rebar specifications for tensile testing

Rebar Size	Diameter (mm)	Cross sectional area (mm^2)	f_y (MPa)	L (mm)	Number of specimens
15M	16	200	400	25	3

Carbon steel tensile test results

Test	f_y (MPa)	f_y average	ε_y	ε_y average	E_{ave} (Gpa)
1	471.8	462	0.0033	0.00315	160
2	446.2		0.0029		
3	468.2		0.0032		

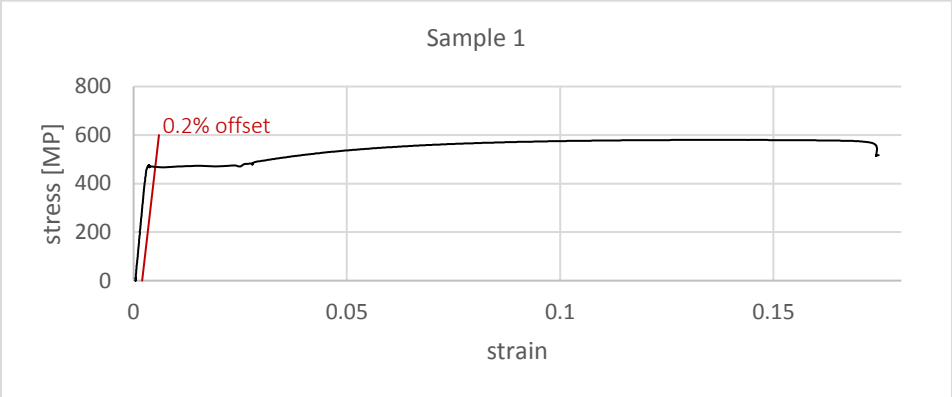

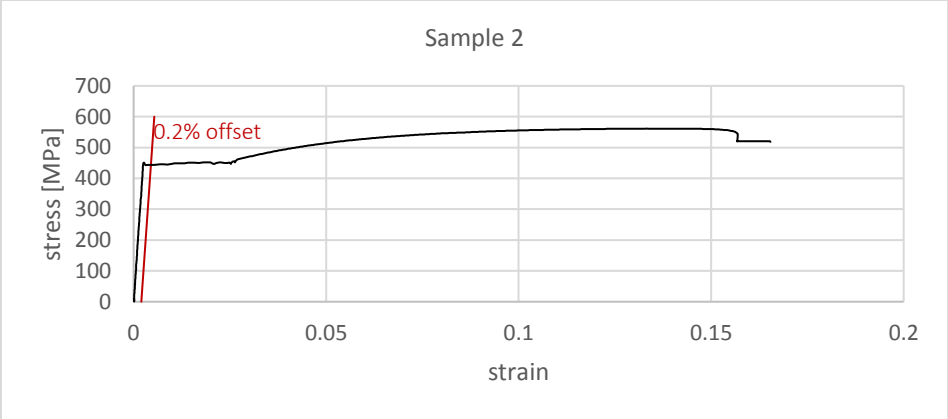

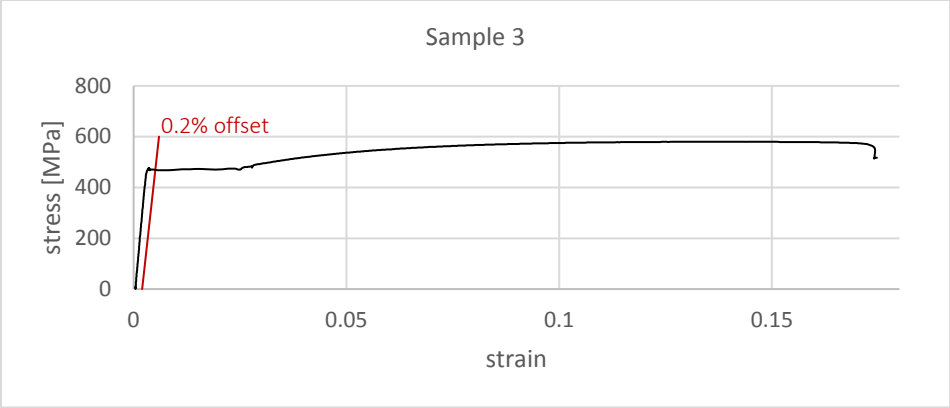

Stainless Steel

The yield point is calculated using the 0.5% extension method for stainless steel samples.

Stainless steel rebar specifications for tensile testing

Rebar Size	Diameter (mm)	Cross sectional area (mm^2)	f_y (MPa)	L (mm)	Number of specimens
#5	16	200	518	25	3

Stainless steel tensile test results

Test	f_y (MPa)	f_y average	ε_y	ε_y average	E_{ave} (Gpa)
SS1	555.0	554	0.0041	0.00434	128
SS2	555.4		0.0042		
SS3	551.5		0.0047		

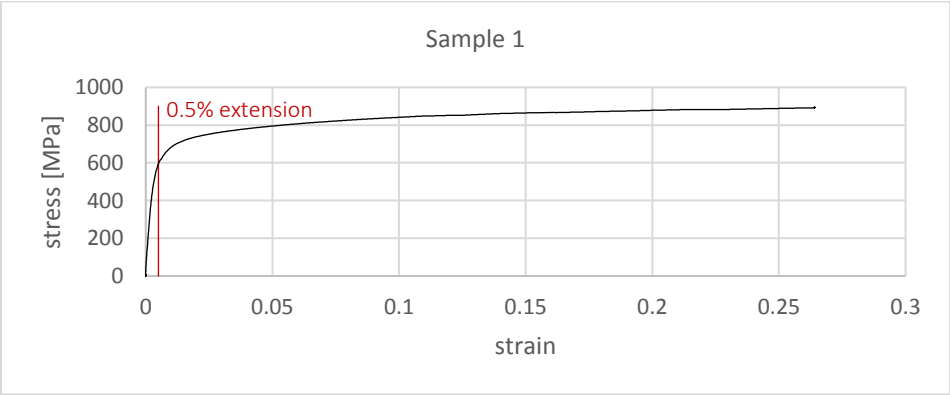

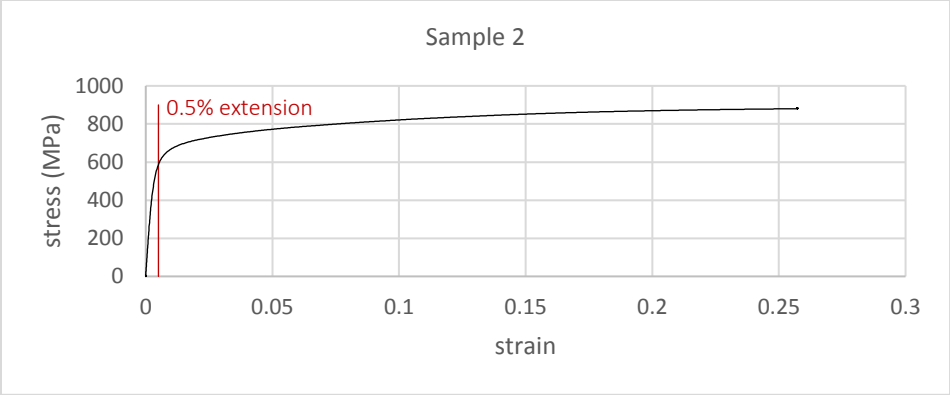
Sample 2
1000
800
600
400
200
0
stress (MPa)
0.5% extension
0
0.05
0.1
0.15
0.2
0.25
0.3
strain

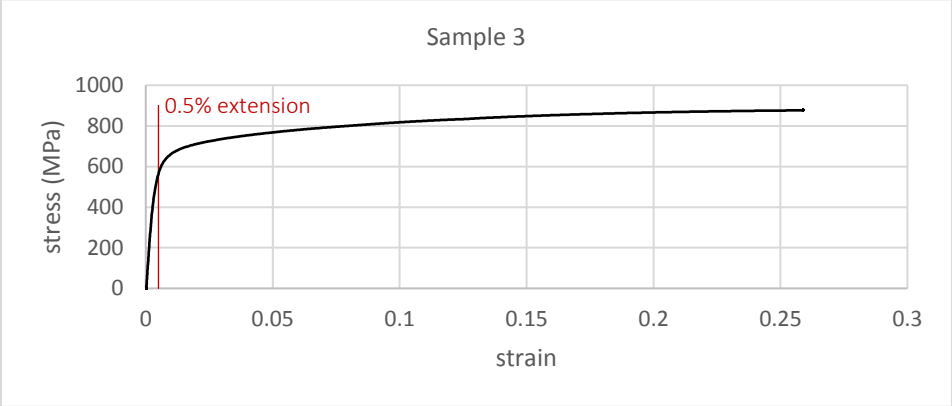
Sample 3
1000
800
600
400
200
0
stress (MPa)
0.5% extension
0
0.05
0.1
0.15
0.2
0.25
0.3
strain

A.6 Concrete Compressive Strength and Density

Concrete Cylinder Testing

Concrete cylinders were cast in order to monitor the strength of concrete during testing. The samples were cast using two pours – pour 1 was done in the morning and was used to cast the samples with the thermal break, and pour 2 was done in the afternoon and was used to cast the samples without the thermal break.

28 Day Concrete Strength

Based on 28 day concrete strength results, a concrete strength of 42 MPa was used to calculate the actual strength of the test samples.

	Cylinder	Diameter (mm)	Height (mm)	Area (mm^3)	Load (lb)	Load (N)	Stress (MPa)	Average Stress (MPa)
Pour 1	1	100	200	7.9E+03	74280	330414	42	42
	2				71950	320050	41	
	3				74200	330058	42	
Pour 2	1	100	200	7.9E+03	72740	323564	41	43
	2				75650	336508	43	
	3				77140	343136	44	

Test Day Concrete Strength

	Cylinder	Diameter (mm)	Height (mm)	Area (mm^3)	Load (lb)	Load (N)	Stress (MPa)	Average Stress (MPa)
Pour 1	1	100	200	7.9E+03	68210	303413	39	39
	2				67630	300833	38	
	3				70810	314979	40	
Pour 2	1	100	200	7.9E+03	77850	346294	44	44
	2				78450	348963	44	
	3				75250	334729	43	

Concrete Density

Concrete density is obtained in order to determine the corresponding thermal conductivity from ISO 10456 [8]. For thermal modelling a thermal conductivity of 2 W/mK was applied for all models based on these results.

	Cylinder	Volume (m^3)	Mass (kg)	Density (kg/m^3)	Average Density (kg/m^3)	Thermal Conductivity (W/mK)
Pour 1	1	0.00157	3.655	2327	2331	1.88
	2	0.00157	3.615	2301		
	3	0.00157	3.715	2365		
Pour 2	1	0.00159	3.820	2408	2403	2
	2	0.00157	3.750	2387		
	3	0.00153	3.695	2413		

A.7 Test Specimen Ultimate Strength Calculations – GFRP Reinforcement

Reinforcement

VRod GFRP #8 Bars

f_u = 1000 MPa

E_f = 66.4 GPa

ε_{fu} = 0.0151

A_b = 506.7 mm^2

d_b = 25 mm

$f_{u,comp} = 0.6\ f_u$ = 600 MPa

$E_{f,comp} = 0.8\ E_f$ = 53.12 GPa

$\varepsilon_{fu,comp}$ = 0.0106

Concrete f'_c = 42 MPa

Thermal Break Moment Capacity Design

Moment arm between A_f and A_f'

$d = h - 2\ c_c - d_b$

d = 85 mm

Moment resistance $M_r = T_f\ d = C_f\ d$

$T_f = f_{u,comp}\ A_f$

$C_f = f_{u,comp}\ A_f'$

$M_r = M_f$ = 19.1 kN-m

Selected Bar Spacing

s = 250

A_f = (500) (500) / 250 = 1000 mm^2

Moment resistance of the connection

$M_r = f_{u,comp}\ A_f\ d$ = (600 MPa) (1000 mm^2) (85 mm) (10^{-6}) = 51 kN-m

Thermal Break Shear Capacity Check

Shear Capacity

The shear strength of frp, f_v, is assumed to be $0.1\ f_{u,comp}$ = 0.1 (600) = 60 MPa

$V_r = f_v\ A_f$ = (60 MPa) (1000 mm^2) = 60 kN

Factored shear force applied to upper row of rebar = V_f / (2 x 2) = 9.55 kN

V_f / V_r = 9.55 / 60 = 0.159

Tensile Capacity

$T_r = f_{u,comp}\ A_f$ = (600 MPa) (1000 mm^2) = 600 kN

$T_f = M_f / d$ = (19.1 kN-m) / (94 mm) = 203 kN

T_f / T_r = 203 / 600 = 0.338

Interaction Equation

$(V_f / V_r)^2 + (T_f / T_r)^2 \leq 1.0$

$(0.159)^2 + (0.338)^2 = 0.14 \leq 1.0$

Slab Capacity Adjacent to Connection (S806-12)

Moment resistance of the section

$A_{frp} = 500\ mm^2\ (500)/\ 250 = 1000\ mm^2$

$d = h - c_c - d_b/2 = 142\ mm$

$\rho_{fb} = \alpha_1\ \beta_1\ (f'_c / f_u)\ (\varepsilon_{cu} / \varepsilon_{cu} + \varepsilon_{frpu}) = (0.8)\ (0.9)\ (42 / 1000)\ (0.0035 / 0.0035 + 0.0151) = 0.0057$

$\rho_f = (1000) / (500)\ (137.5) = 0.015 > \rho_{fb}$

The section will fail by concrete rupture

$f_{frp} = 0.5\ E_{frp}\ \varepsilon_{cu}\ [\ (1 + 4\ \alpha_1\ \beta_1\ f'_c / \rho_{frp}\ E_{frp}\ \varepsilon_{cu})^{1/2} -1]$

$f_{frp} = (0.5)(66{,}400)(0.0035)\ [(1 + (4)(0.9)(0.8)(42)/(0.015)(66{,}400)(0.0035)\ )^{1/2} -1] = 578\ MPa$

$a = A_{frp}\ f_{frp} / \alpha_1\ f'_c\ b = (1000)\ (578) / (0.8)\ (30)\ (500) = 48.2\ mm$

$M_r = A_{frp}\ f_{frp}\ (d - a/2) = (1000)\ (578)\ (137.5 - 48.2/2)\ (10^{-6}) = 65.5\ kN\text{-}m$

$M_{cr} = f_r\ I_g / y_t$

$f_r = 0.6\ f'^{1/2}_c = (0.6)\ (42)^{1/2} = 3.89$

$M_{cr} = (3.89)\ (500)(190)^3 / (12)\ (190/2)\ (10^{-6}) = 11.7\ kN\text{-}m$

$M_r = 65.5\ kN\text{-}m > M_f = 19.1\ kN\text{-}m$ and $M_r = 65.5\ kN\text{-}m > 2\ M_{cr} = 23.4\ kN\text{-}m$

Shear capacity of the section

$V_c = 0.05\ \lambda\ k_m\ k_r\ f'^{1/3}_c\ b_w\ d_v$ with $V_c > 0.11\ f'^{1/2}_c\ b_w\ d_v$

$\lambda = 1.0$

$d_v > 0.9\ d = 124$ or $0.72\ h = 137$

$k_m = (V_f\ d / M_f)^{1/2} = [(19.1)\ (10^3)\ (137.5) / (19.1)\ (10^6)]^{1/2} = 0.37$

$\rho_{fw} = A_f / b\ d = 0.015$

$k_r = 1 + (E_f\ \rho_{fw})^{1/3} = 10.99$

$V_c = (0.05)\ (0.37)\ (10.99)\ (42)^{1/3}\ (500)\ (137)\ (10^{-3}) = 48.4\ kN$

$V_c > 0.11\ (42)^{1/2}\ (500)\ (137)\ (10^{-3}) = 48.8\ kN$

$V_c = 48.8\ kN > V_f = 19.1\ kN$

A.8 Test Specimen Ultimate Strength Calculations – Steel Reinforcement

Reinforcement

15M Steel Bars

f_y = 462 MPa

E_s = 200 GPa

A_b = 200 mm^2

d_b = 16 mm

Concrete

f'_c = 42 MPa

Thermal Break Moment Capacity

Moment arm between A_s and A_s'

$d = h - 2\ c_c - d_b$

d = 94 mm

Moment resistance $M_r = T_s\ d = C_s\ d$

$T_s = f_y\ A_s$

$C_s = f_y\ A_s'$

$M_r = M_f$ = 38.2/2 = 19.1 kN-m

Selected Bar Spacing

s = 167

A_s = (200) (500) / 167 = 600 mm^2

Moment resistance of the connection

$M_r = f_y\ A_s\ d$ = (462 MPa) (600 mm^2) (94 mm) (10^{-6}) = 26.1 kN-m

Thermal Break Shear Capacity Check

Shear Capacity

$V_r = 0.66\ f_y A_s$ = 0.66 (462 MPa) (600 mm^2) = 183 kN

Factored shear force applied to upper row of rebar = V_f / (2 x 2) = 9.6 kN

V_f / V_r = 9.6 / 183 = 0.05

Tensile Capacity

$T_r = f_y\ A_s$ = (400 MPa) (600 mm^2) = 240 kN

$T_f = M_f / d$ = (19.1 kN-m) / (94 mm) = 203 kN

T_f / T_r = 203 / 240 = 0.85

Interaction Equation

$(V_f / V_r)^2 + (T_f / T_r)^2 \leq 1.0$

$(0.05)^2 + (0.85)^2 = 0.725 \leq 1.0$

Slab Capacity Adjacent to Connection (CSA A23.3)

Moment resistance of the section

$A_s = (200\ mm^2)\ (500\ mm)/\ (500/3\ mm) = 600\ mm^2$

$a = f_y\ A_s / \alpha_1\ f'_c\ b = (462\ MPa)\ (600\ mm^2) / (0.8)\ (42\ MPa)\ (500\ mm) = 16.5\ mm$

$d = h - c_c - d_b/2 = 142\ mm$

$M_r = f_y\ A_s\ (d - a/2) = (462\ MPa)\ (600\ mm^2)\ (142\ mm - 16.5\ mm/2)\ (10^{-6}) = 37.1\ kN\text{-}m$

Shear capacity of the section

$V_c = \lambda\ \beta\ f'^{1/2}_c\ b_w\ d_v$

$d_v > 0.9\ d = 127.8$ or $0.72\ h = 136.8$

$b_w = 500\ mm$

$\lambda = 1$

$\beta = 230 / (1000 + d_v) = 0.20$ (simplified method)

$V_c = (0.20)\ (42\ MPa)^{1/2}\ (500\ mm)\ (136.8\ mm)\ (10^{-3}) = 88.7\ kN$

$V_c = 88.7\ kN > V_f = 19.1\ kN$

A.9 Test Specimen Ultimate Strength Calculations – Stainless Steel Reinforcement Reinforcement

Number 5 Stainless Steel Bars - Provided by Salit Steel

f_y = 554 MPa

E_s = 200 GPa

A_b = 200 mm^2

d_b = 16 mm

Concrete

f'_c = 42 MPa

Thermal Break Moment Capacity Design

Moment arm between A_s and A_s'

$d = h - 2\ c_c - d_b$

d = 94 mm

Moment resistance $M_r = T_s\ d = C_s\ d$

$T_s = f_y\ A_s$

$C_s = f_y\ A_s'$

$M_r = M_f$ = 38.2/2 = 19.1 kN-m

Selected Bar Spacing

s = 250

A_s = (200) (500) / 250 = 400 mm^2

Moment resistance of the connection

$M_r = f_y\ A_s\ d$ = (554 MPa) (400 mm^2) (94 mm) (10^{-6}) = 20.8 kN-m

Thermal Break Shear Capacity Check

Shear Capacity

$V_r = 0.66\ f_y A_s$ = 0.66 (554 MPa) (400 mm^2) = 146.3 kN

Factored shear force applied to upper row of rebar = V_f / (2 x 2) = 9.5 kN

V_f / V_r = 9.6 / 146.3 = 0.066

Tensile Capacity

$T_r = f_y\ A_s$ = (518 MPa) (400 mm^2) = 207 kN

$T_f = M_f / d$ = (19.1 kN-m) / (94 mm) = 203 kN

T_f / T_r = 203 / 207 = 0.98

Interaction Equation

$(V_f / V_r)^2 + (T_f / T_r)^2 \leq 1.0$

$(0.066)^2 + (0.98)^2 = 0.96 \leq 1.0$

Slab Capacity Adjacent to Connection (CSA A23.3)

Moment resistance of the section

$A_s = (200\ mm^2)\ (500\ mm)/\ (250\ mm) = 400\ mm^2$

$a = f_y\ A_s / \alpha_1\ f'_c\ b = (554\ MPa)\ (400\ mm^2) / (0.8)\ (42\ MPa)\ (500\ mm) = 13.2\ mm$

$d = h - c_c - d_b/2 = 142\ mm$

$M_r = f_y\ A_s\ (d - a/2) = (554\ MPa)\ (400\ mm^2)\ (142\ mm - 13.2\ mm/2)\ (10^{-6}) = 30\ kN\text{-}m$

Shear capacity of the section

$V_c = \lambda\ \beta\ f'^{1/2}_c\ b_w\ d_v$

$d_v > 0.9\ d = 127.8$ or $0.72\ h = 136.8$

$b_w = 1000\ mm$

$\lambda = 1$

$$\beta = \frac{0.4}{1+1500\varepsilon_x} \cdot \frac{1300}{1000+s_{ze}}$$

$s_{ze} = 35\ s_z / 15 + a_g = (35)\ (136.8) / (15 + 20) = 136.8$

$$\varepsilon_x = \frac{\frac{M_f}{dv}+V_f}{2E_sA_s} = [(38.2)\ (10^6) / (136.8) + (38.2)\ (10^3)] / [2\ (200{,}000)\ (400)] = 0.00099$$

$B = [0.4 / (1 + 1500\ (0.00099))] \cdot [1300 / (1000 + 136.8)] = 0.184$

$V_c = (0.184)\ (42)^{1/2}\ (500)\ (136.8)\ (10^{-3}) = 81.6\ kN$

$V_c = 81.6\ kN > V_f = 19.1\ kN$

A.10 Calculated Load Deflection Curves for Test Specimens

Curves are plotted until calculated rebar yield or concrete fracture load.

	With Thermal Break		Without Thermal Break	
Reinforcement	Failure Load [kN]	Deflection at Failure [mm]	Failure Load [kN]	Deflection at Failure [mm]
Carbon Steel	29.6	2.38	41.6	2.53
Stainless Steel	25.6	3.06	36.2	3.24
GFRP	43.3	7.71	43.3	5.88

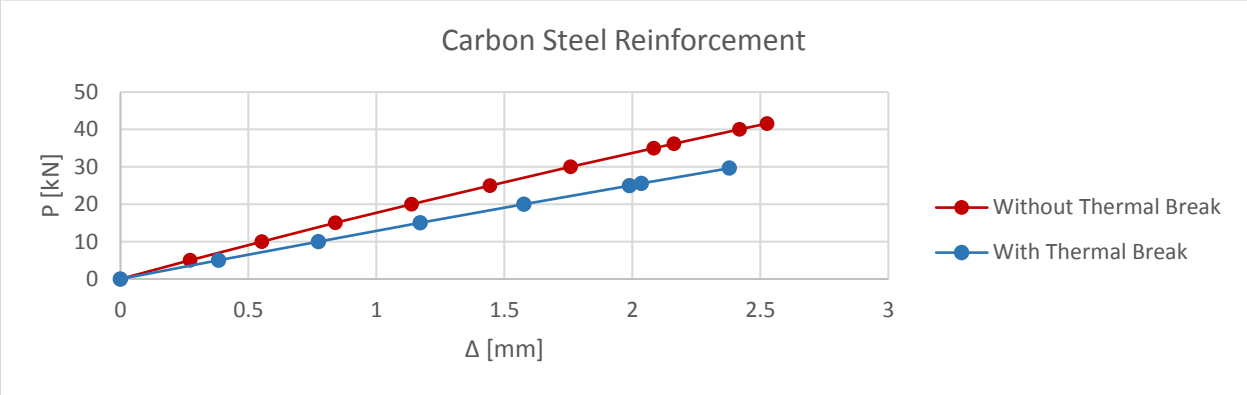

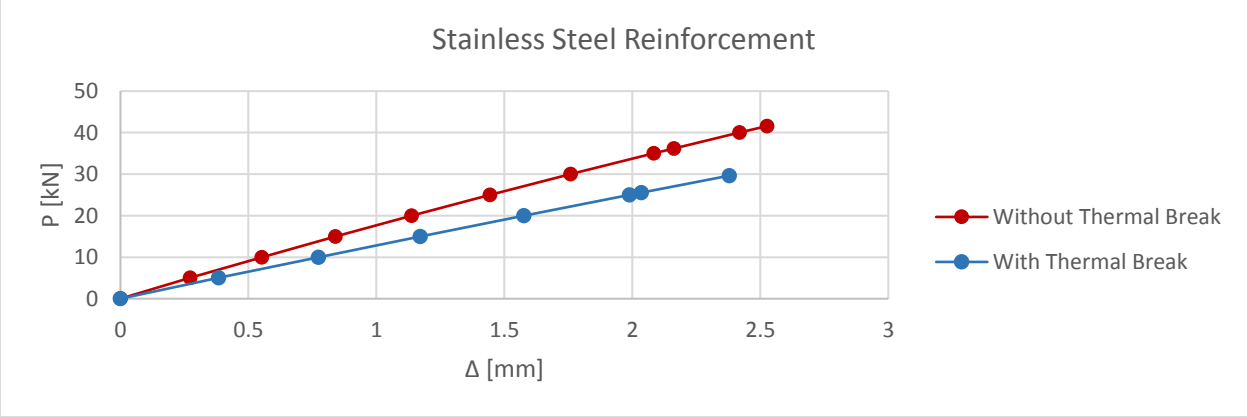

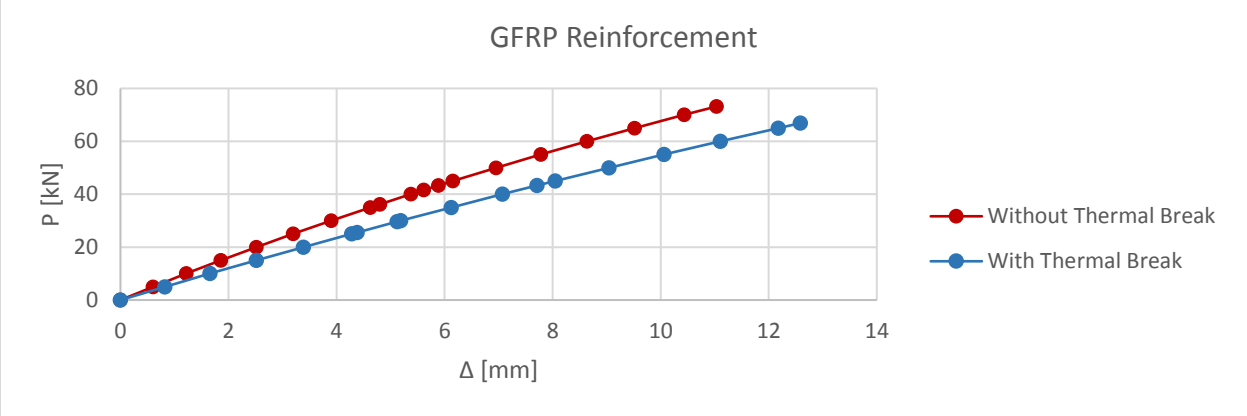

A.11 Thermistor Layout for Thermal Testing

GFRP Reinforced Samples

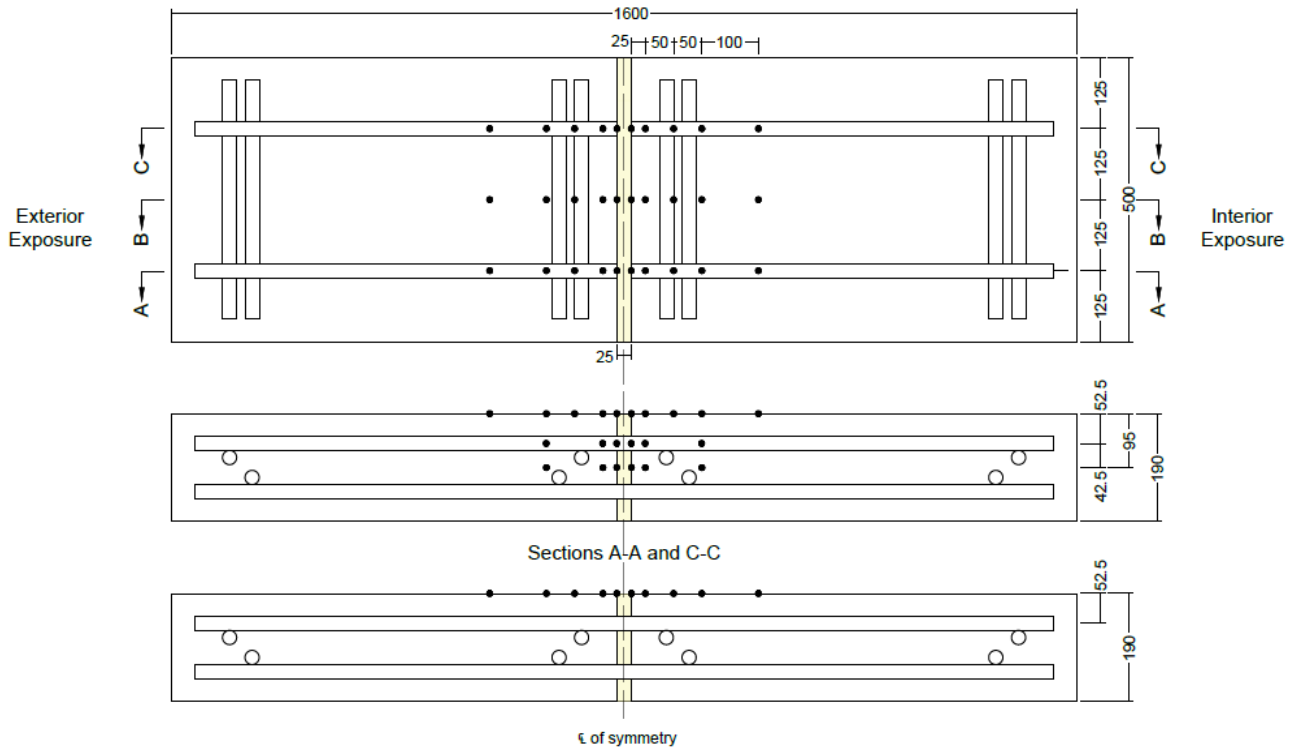

Steel Reinforced Samples

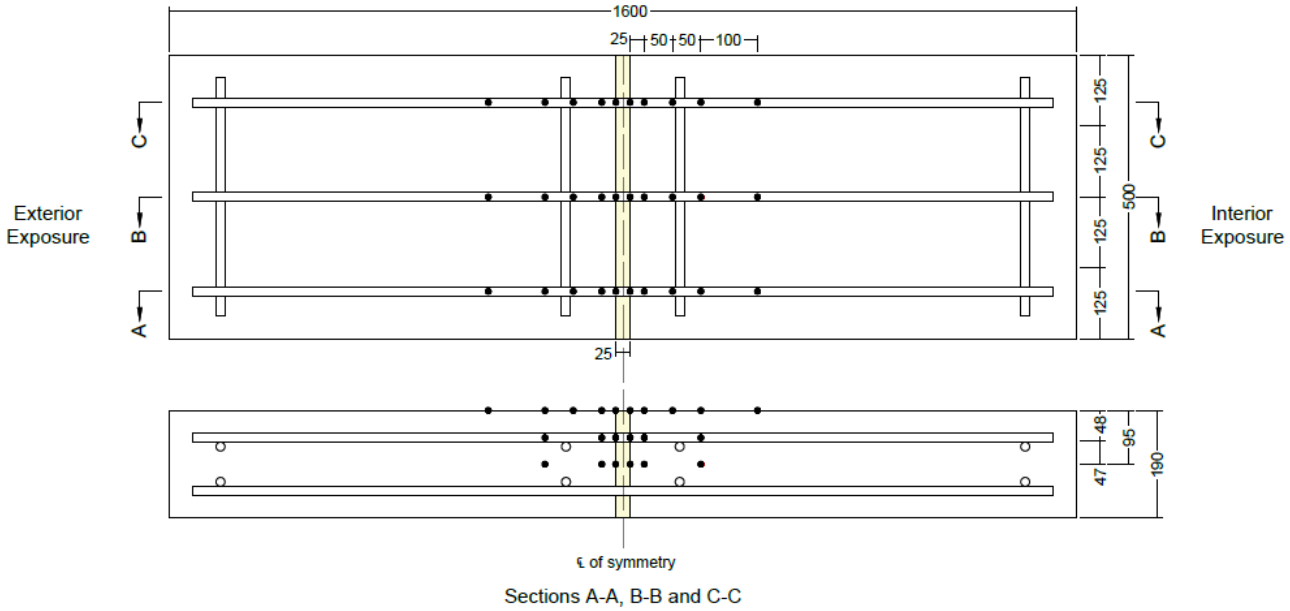

Stainless Steel Reinforced Samples

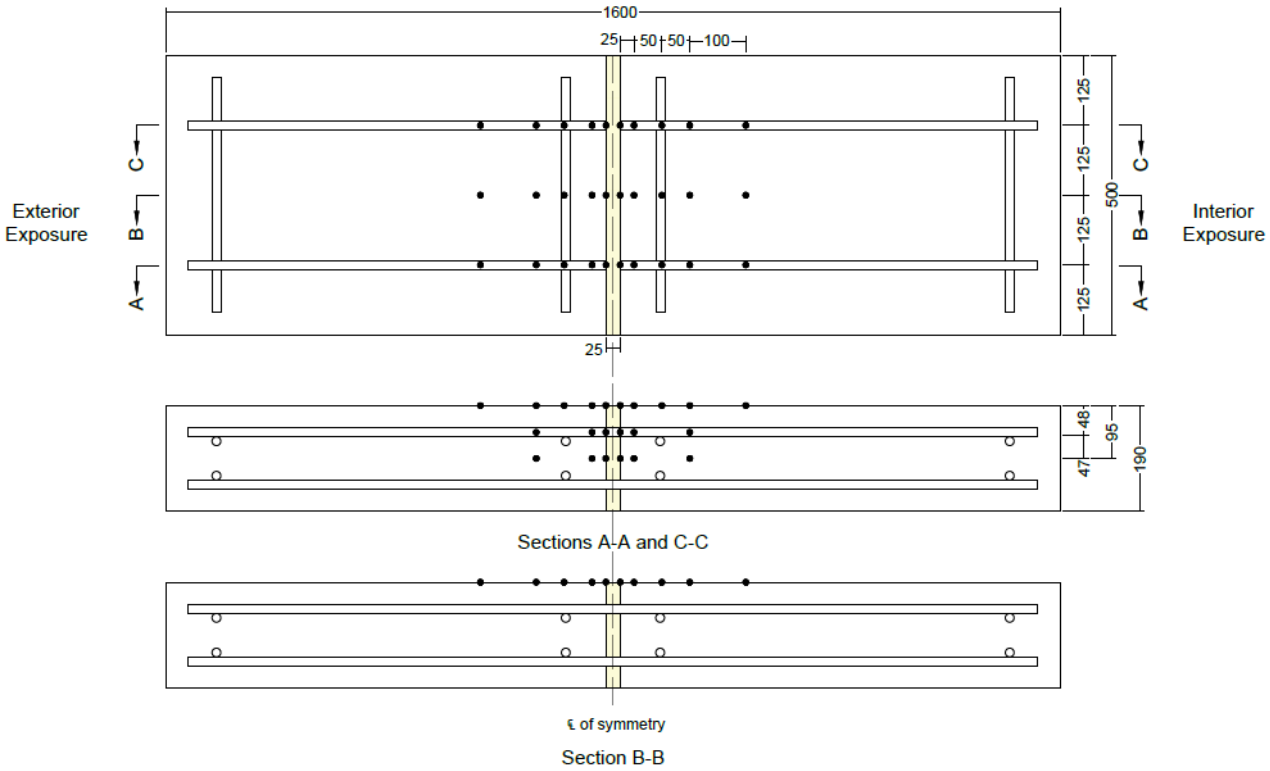
1600
25
50
50
100
125
125
125
125
500
C
B
A
C
B
A
Exterior
Exposure
Interior
Exposure
25
48
95
190
47
Sections A-A and C-C
℄ of symmetry
Section B-B